
Linear and nonlinear response in solids: a density functional based approach

Dissertation
zur Erlangung des akademischen Grades
Doctor rerum naturalium
(Dr. rer. nat.)

vorgelegt von

Yang Zhang

geboren am 05.06.1993
in Hubei, China

Fachrichtung Physik
Fakultät für Mathematik und Naturwissenschaften
Technische Universität Dresden
2018

Eingereicht am: 10. Dec 2018

Verteidigt am:

1. Gutachter: Prof. Dr. Jeroen van den Brink
2. Gutachter: Prof. Dr. Claudia Felser
3. Gutachter: Dr. Binghai Yan

Abstract

The description of the ground-state properties of solids has reached maturity with the development of first-principle techniques in recent years, especially the prediction of the structural and electronic properties of complex electronic systems. However, aspects of the response to external perturbations remain to be explored, partly because of the much larger computational cost compared with ground-state calculation. Herein, we study, develop, and implement the linear response and nonlinear response formalism based on the Kubo approach from a first-principle Wannier Hamiltonian in periodic solid systems, especially the topological semimetal and noncollinear magnets. We calculate in detail the charge current, spin current, and photocurrent driven by an external electrical field, temperature gradient, and laser radiation in the linear and nonlinear regime—i.e. in linear response: anomalous Hall effect, spin Hall effect, spin Nernst effect, and spin-polarised charge current; in nonlinear response: nonlinear Hall effect, Berry dipole, and photogalvanic effect under linearly and circularly polarised light in detail. Several detailed studies are presented into different transport properties of solid systems, including topological materials with unconventional low-energy quasi-particles, e.g. Dirac or Weyl points, and noncollinear coplanar antiferromagnets.

Contents

abstract	iii
1 Introduction	1
1.1 Background	1
1.2 Linear response theory and Berry curvature	2
1.2.1 Linear response Kubo formula	2
1.2.2 Semiclassical equation and Berry curvature	6
1.2.3 Berry curvature formalism for anomalous Hall effect and spin Hall effect	8
1.3 Nonlinear, second order response	10
1.3.1 Nonlinear Hall effect from Berry curvature dipole	11
1.3.2 Second order Kubo formula for optical response	13
1.4 Structure of the thesis	15
1.5 List of publications	16
2 Density functional theory and Wannier approach	19
2.1 Hohenberg-Kohn theorem: electron density as a basic variable	20
2.1.1 Kohn-Sham formalism	21
2.1.2 Exchange-correlation functional	22
2.2 The relativistic effect and FPLO realization of DFT	24
2.2.1 Dirac equation and spin-orbit coupling	24
2.2.2 FPLO formalism	25
2.3 Wannier functions from FPLO	26
2.3.1 Wannier transformation in FPLO	27
3 Weyl semimetal phase and linear response Hall current	30
3.1 Introduction	30
3.1.1 Weyl fermion from massless Dirac equation	31
3.1.2 Weyl semimetal and unique surface state	31

3.2	Magnetic weyl semimetal in Ti_2MnAl	33
3.2.1	Weyl point and Fermi arc	34
3.3	Anomalous Hall effect from magnetic Weyl Fermion	37
3.4	Summary	39
4	Linear response of spin current: spin Hall and Nernst effect	41
4.1	Dirac nodal line induced spin Hall effect	41
4.1.1	Nodal line semimetal	42
4.1.2	Results and Discussions	45
4.1.3	Nonsymmorphic symmetry	45
4.1.4	Dirac Nodal lines without SOC	45
4.1.5	Dirac nodal lines with SOC	47
4.1.6	Dirac nodal lines and spin Hall effect	49
4.1.7	Conclusions	51
4.2	Spin current from temperature gradient: spin Nernst effect in InBi	51
4.2.1	Introduction	52
4.2.2	Spin Nernst formalism and model parameter	52
4.2.3	Band structure, spin Hall, and spin Nernst conductivity	55
5	Spin current in non-collinear antiferromagnets: spin Hall and spin polarized current	64
5.1	Spin Hall effect emerging from a noncollinear magnetic lattice without spin-orbit coupling	64
5.1.1	introduction	65
5.1.2	Double-exchange model and symmetry analysis	66
5.1.3	Realistic materials	69
5.1.4	discussion	73
5.2	Spin-polarized current in non-collinear antiferromagnets	75
5.2.1	Introduction.	75
5.2.2	Symmetry analysis and calculations.	77
5.2.3	Discussion	81
6	Nonlinear electrical response: Berry curvature dipole	84
6.1	Semiclassical Berry dipole and nonlinear anomalous Hall current	85
6.1.1	Simple effective model of Weyl points and corresponding Berry curvature dipole	86

6.2	Ab initio calculation of Berry dipole in TaAs and NbP	88
6.2.1	Result of realistic materials	89
6.2.2	Discussion	92
6.3	Berry dipole in two dimensional two-dimensional transition-metal dichalco- genides WTe ₂ and MoTe ₂	94
6.3.1	Introduction	94
6.3.2	Response tensor in different structure	94
6.3.3	Discussion on magnitude	99
6.3.4	Conclusions	101
7	Nonlinear optical response	102
7.1	Introduction	102
7.2	Resonance theory	104
7.3	Result of TaAs	106
7.4	Effect of disorders and fluctuations.	107
7.5	Two- and three-band processes	108
7.6	Discussion and comparison with experiments	109
7.7	Summary	111
8	Summary	112
	Bibliography	114
	Acknowledgements	142
	Eidesstattliche Erklärung	143

1 Introduction

1.1 Background

Solids are typical many-body systems containing nearly 10^{23} ions and even one order-of-magnitude more electrons. Although the underlying physical laws governing the properties of such a system are known, to obtain the desired quantities one has to solve a large set of coupled equations in the form of the relativistic Dirac equation or nonrelativistic Schrödinger equation. As indicated by Dirac's famous saying, the exact applications of these fundamental laws to solids always lead to massively complicated equations, which are generally not solvable by the most powerful supercomputers. Thus, the development of approximate methods is key in condensed matter physics.

Density functional theory (DFT) is the most widely used method for the investigation of the ground state (magnetic structure, electronic structure, etc.) of many-body systems, which is discussed in detail in Chapter 2. In addition to the static properties, the study of dynamic transport phenomenon is one of the most important driving forces of modern physics. With the ground-state wavefunction from first-principle calculations and perturbation theory, one would be able to calculate the susceptibility of the system to an external driven field, such as the electric and magnetic field, temperature gradient, or optical radiation as shown in Fig. 1.1. These three types of external perturbations are studied throughout this work, typically on Weyl semimetals (WSMs) with monopoles of Berry curvature.

Despite the well-developed quantum and semiclassical theory of response phenomena, the huge Hilbert space of the first-principle wavefunction basis makes it time-consuming to calculate even the intrinsic Hall conductivity in real materials. There is a need to develop theoretical approximations and efficient numerical algorithms for a good description of the realistic response phenomenon. In the present work, we mainly study the Berry-phase-related linear and second-order response to a relatively low-amplitude driving field, which would not move our system far away from the equilibrium state, i.e. in the valid region of perturbation theory. Our target systems are topological semimetals with unconventional

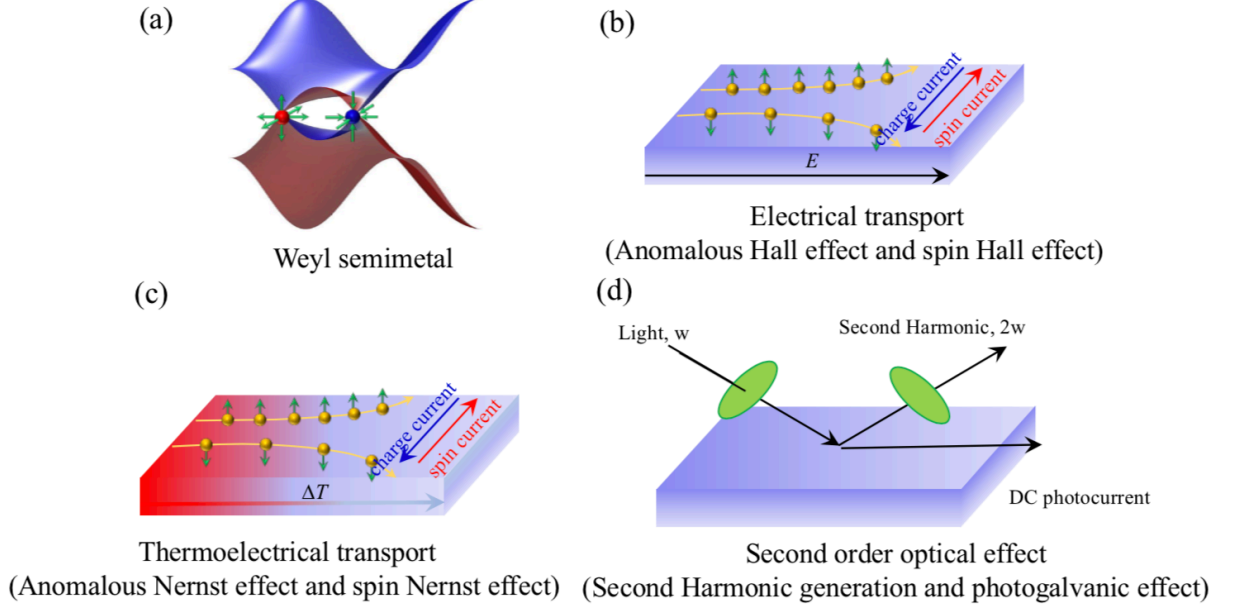


Figure 1.1: (a) (2+1) D band structure of a pair of Weyl nodes, (b) Charge and spin current under external electric field, (c) Charge and spin current under external temperature gradient, (d) Second Harmonic generation and DC photocurrent from optical radiation.

low-energy quasi-particles and noncollinear antiferromagnetic materials.

1.2 Linear response theory and Berry curvature

The response of metals to external electric fields can be described well by linear response theory, in which the response of the system is linear in the applied field. In this section, we derive the quantum mechanical Kubo formula and the semiclassical equations for electron motion, further we present the expression for anomalous Hall effect and spin Hall effect in terms of Berry curvature.

1.2.1 Linear response Kubo formula

We start from a quantum system described by the (time-independent) Hamiltonian \hat{H}_0 . Further, the expectation value of a response observable (described by the operator \hat{A}) can

be evaluated as [?]:

$$\langle \hat{A} \rangle = \frac{1}{Z_0} \text{Tr}[\hat{\rho}_0 \hat{A}] = \frac{1}{Z_0} \sum_n \langle n | \hat{A} | n \rangle e^{-\beta E_n}$$

where $Z_0 = \text{Tr}[\hat{\rho}_0]$ is the partition function expressed by the density matrix $\hat{\rho}_0 = e^{-\beta \hat{H}_0} = \sum_n |n\rangle \langle n| e^{-\beta E_n}$

After applying the external perturbation $\hat{F}(t)$, we obtain the time-dependent Hamiltonian $\hat{H}(t) = \hat{H}_0 + \hat{F}(t)$, and the evolution of density matrix is

$$i\hbar \dot{\hat{\rho}}(t) = [\hat{H}_0, \hat{\rho}(t)] + [\hat{F}(t), \hat{\rho}(t)] \quad (1.1)$$

As the time-dependent wavefunction $|n(t)\rangle$ is given by Schrödinger equation $i\hbar \partial_t |n(t)\rangle = \hat{H}(t) |n(t)\rangle$ and we assume $\hat{F}(t)$ is a weak external perturbation, only the lowest order of wavefunction ($n_D(t)$) is required from the interaction picture (Dirac picture). The relation between two pictures is given by

$$|n(t)\rangle = e^{-i\hat{H}_0(t-t_0)} |n_D(t)\rangle = \hat{U}_0^{-1}(t, t_0) |n_D(t)\rangle,$$

and t_0 is the time that the two pictures are identical, here we set $t_0=0$ for simplicity. The operators in the Dirac representations are related to the Schrödinger representation via

$$\hat{F}_D = e^{\frac{i}{\hbar} \hat{H}_0 t} \hat{F} e^{-\frac{i}{\hbar} \hat{H}_0 t} = \hat{U}_0 \hat{F} \hat{U}_0^{-1} \quad (1.2)$$

In the lowest nontrivial order (linear) of external perturbation $\hat{F}_D(t)$, one has

$$\hat{\rho}_D(t) = \hat{\rho}_0 - \frac{i}{\hbar} \int_{-\infty}^t dt' [\hat{F}_D(t'), \hat{\rho}_0]. \quad (1.3)$$

Here ρ_0 is the density matrix of unperturbed Hamiltonian, and thus identical under two representations. Then we have the first order density operator in Schrödinger representation as

$$\begin{aligned} \hat{\rho}(t) &= \hat{\rho}_0 - \frac{i}{\hbar} \int_{-\infty}^t dt' e^{-\frac{i}{\hbar} \hat{H}_0 t} [\hat{F}_D(t'), \hat{\rho}_0] e^{\frac{i}{\hbar} \hat{H}_0 t} \\ &= \hat{\rho}_0 - \frac{i}{\hbar} \int_{-\infty}^t dt' \hat{U}_0^{-1} [\hat{F}_D(t'), \hat{\rho}_0] \hat{U}_0. \end{aligned} \quad (1.4)$$

Finally, we obtain the Kubo formula in the Dirac representations, which determines the

mean change of response observable $\hat{A}(t)$ from cyclic properties of trace as:

$$\begin{aligned}
\delta A(t) &= \langle \hat{A}(t) \rangle - \langle \hat{A}_0 \rangle = \text{Tr}[\hat{\rho}(t)\hat{A}] - \text{Tr}[\hat{\rho}_0\hat{A}] \\
&= -\frac{i}{\hbar} \int_{-\infty}^t dt' \text{Tr}([\hat{F}_D(t'), \hat{\rho}_0] \hat{U}_0 \hat{A}(t) \hat{U}_0^{-1}) \\
&= -\frac{i}{\hbar} \int_{-\infty}^t dt' \text{Tr}(\rho_0[\hat{A}_D(t), \hat{F}_D(t')]) \\
&= -\frac{i}{\hbar} \int_{-\infty}^t dt' \langle [\hat{A}_D(t), \hat{F}_D(t')] \rangle_0
\end{aligned} \tag{1.5}$$

Here, $\langle \rangle_0$ is the mean value of the unperturbed Hamiltonian, which involves only the equilibrium wavefunctions of \hat{H}_0 . With the Kubo formula, the linear response of an observable \hat{A} caused by a perturbation \hat{F} can be determined with the knowledge of equilibrium Hamiltonian H_0 . In our case, the H_0 for a real material is obtained from DFT and Wannier approach.

The Eq. 1.5 shows that the correlation function of \hat{A} and \hat{F} describes the linear response of an observable \hat{A} due to the perturbation coupled to \hat{F} . Since a physically meaningful result is obtained only if the \hat{F} is turned on adiabatically: $\hat{F}(t) = e^{(\epsilon/\hbar)t} \hat{F}$, with ϵ a positive infinitesimal, and the response would be evaluated at $t = 0$. For simplicity, we also evaluate the density operator in zero temperature as $\hat{\rho}_0 = |\Psi_0\rangle\langle\Psi_0|$, with $|\Psi_0\rangle$ as the ground state of \hat{H}_0 . Since \hat{H}_0 is non-interacting, $|\Psi_0\rangle$ is the Slater determinant of the single-particle wavefunctions $|i\rangle$ ($i = 1, \dots, n$). Thus Eq. 1.5 is expressed as:

$$\delta A(t) = -\frac{i}{\hbar} \int_{-\infty}^0 dt' e^{(\epsilon/\hbar)t'} \sum_n f(E_n) \langle n | \hat{A} \hat{F}_D(t') | n \rangle - \langle n | \hat{F}_D(t') \hat{A} | n \rangle \tag{1.6}$$

where $f(E_n)$ is the Fermi-Dirac distribution and E_n is the energy of $|n\rangle$. Since $\hat{H}_0|n\rangle = E_n|n\rangle$, we have $\hat{U}_0|n\rangle = e^{\frac{i}{\hbar}E_n t}|n\rangle$. By inserting $\sum_m |m\rangle\langle m| = 1$ and perform the integral over time domain, we would obtain

$$\begin{aligned}
\delta A &= -\frac{i}{\hbar} \sum_{n,m} (f(E_n) - f(E_m)) \langle n | \hat{A} | m \rangle \langle m | \hat{F} | n \rangle \int_{-\infty}^0 dt' e^{\frac{i}{\hbar}(E_m - E_n - i\epsilon)t'} \\
&= -\sum_{n,m} \frac{(f(E_n) - f(E_m))}{E_m - E_n - i\epsilon} \langle n | \hat{A} | m \rangle \langle m | \hat{F} | n \rangle
\end{aligned} \tag{1.7}$$

For the evaluation of Eq. 1.7, we only need to know the Hamiltonian of unperturbed system. Since the most interested external perturbation is electrical field in this thesis, we

derive the general Kubo formula for the response to the DC electrical field. Here $\hat{F} = eE\hat{r}$, with e, E, \hat{r} stand for elementary charge, electrical field amplitude, and position operator. The position operator \hat{r} and velocity operator \hat{v} have the relation as $\hat{v} = \frac{i}{\hbar}[H, \hat{r}]$, and the matrix elements of position operation can be written in terms of velocity operator

$$\begin{aligned}\langle n|\hat{v}|m\rangle &= \frac{i}{\hbar}(E_n\langle n|\hat{r}|m\rangle - E_m\langle n|\hat{r}|m\rangle) \\ \langle n|\hat{r}|m\rangle &= -i\hbar\frac{\langle n|\hat{v}|m\rangle}{E_n - E_m}\end{aligned}\tag{1.8}$$

In the end, we find the δA for the the external electrical field E as

$$\delta A = -i\hbar eE \sum_{n,m} \frac{(f(E_n) - f(E_m))}{(E_m - E_n - i\epsilon)(E_n - E_m)} \langle n|\hat{A}|m\rangle \langle m|\hat{v}|n\rangle\tag{1.9}$$

As the response properties of real materials largely depend on disorder and impurities, it is necessary to express the Kubo formula in terms of Green's functions (see Appendix A of Ref. [36] for the detailed derivation). Here, we use the so-called constant Γ approximation, i.e. we assume that the only effect of the disorder is merely a constant band broadening, which modifies the Green's functions of the perfectly periodic system as follows: $G^R(\varepsilon) = 1/(\varepsilon - \hat{H} + i0+) \rightarrow 1/(\varepsilon - \hat{H} + i\Gamma)$, where \hat{H} is the Hamiltonian, ε is the energy, G^R is the retarded Green's function (the advanced Green's function is modified analogously), and Γ is a constant that determines the broadening magnitude.

Subsequently, we decompose the Kubo formula into two contributions that transform in the opposite way under time-reversal, by separating the real and imaginary part of the denominator (since the wave function is antisymmetric under time reversal operation). Within the constant Γ approximation, the two contributions to the linear response of an observable \hat{A} to for instance an electric field ($\hat{F} = eE\hat{r}$) are given by $\delta A = \chi^I E + \chi^{II} E$ from Eq. 1.7, where [55]

$$\chi^I = -\frac{e\hbar}{\pi} \sum_{\mathbf{k}, n, m} \frac{\Gamma^2 \text{Re} \left(\langle n\mathbf{k} | \hat{A} | m\mathbf{k} \rangle \langle m\mathbf{k} | \hat{\mathbf{v}} \cdot \hat{\mathbf{E}} | n\mathbf{k} \rangle \right)}{[(E_F - E_{n\mathbf{k}})^2 + \Gamma^2][(E_F - E_{m\mathbf{k}})^2 + \Gamma^2]},\tag{1.10}$$

$$\chi^{II} = -2\hbar e \sum_{\mathbf{k}, n \neq m} \frac{\text{Im} \left(\langle n\mathbf{k} | \hat{A} | m\mathbf{k} \rangle \langle m\mathbf{k} | \hat{\mathbf{v}} \cdot \hat{\mathbf{E}} | n\mathbf{k} \rangle \right)}{(E_{n\mathbf{k}} - E_{m\mathbf{k}})^2},\tag{1.11}$$

In Eq. (1.11), the sum is restricted to m, n such that n is occupied and m is unoccupied. The sums over \mathbf{k} run over all \mathbf{k} points in the first Brillouin zone (BZ). Here, we provide

the contribution χ^{II} only in the limit $\Gamma \rightarrow 0$, which is the intrinsic contribution because it is determined only by the electronic structure of the perfect crystal. In the limit $\Gamma \rightarrow 0$, Eq. (1.10) becomes the well-known Boltzmann formula with a constant relaxation time (with the relaxation time given by $\hbar/2\Gamma$). This contribution diverges as $1/\Gamma$ when $\Gamma \rightarrow 0$. While these formulas are simple, they often do provide at least qualitatively and sometimes even quantitatively correct descriptions. We use them to illustrate the symmetry of linear response and to calculate the intrinsic Hall current. When \hat{A} is equal to the current density operator: $\hat{\mathbf{j}} = -e\hat{\mathbf{v}}/V$ (V is the sample volume), Eq. (1.10) describes the longitudinal conductivity from Fermi surface scattering and Eqs. (1.11) the Hall conductivity, which is also known as the momentum integral of Berry curvature (the perturbational expression) in the BZ.

1.2.2 Semiclassical equation and Berry curvature

Eqs. (1.11) can also be obtained from the quantum mechanical equation of electron motion, and Sundaram and Niu [201] introduced an additional anomalous velocity in terms of Berry curvature to the conventional semiclassical equation of charge current, which is also the starting point of later work on second-order transport.

The traditional semiclassical equations of electron motion only consider the electron velocity at the lowest order of electrical field, the external electrical field would not affect the velocity:

$$\dot{\mathbf{r}} = \frac{1}{\hbar} \nabla_{\mathbf{k}} E_{\mathbf{k}} \quad (1.12)$$

Here $\frac{1}{\hbar} \nabla_{\mathbf{k}} E_{\mathbf{k}}$ is the dispersion function of electron energy $E_{\mathbf{k}}$, known as group velocity. However, the external electrical field would also modify the wavefunction of electron, consequently adding the additional term to the total velocity. A better approach of understanding the influence of electric field is to let the electric field enter into the Hamiltonian and then solve the Schrödinger equation. To realize this target we would add an uniform time-dependent vector potential $\mathbf{A}(t)$ to the unperturbed Hamiltonian

$$H(t) = \frac{[\hat{\mathbf{p}} + e\mathbf{A}(t)]^2}{2m} + V(\mathbf{r}) . \quad (1.13)$$

After the unitary transforming from real space to q space, we obtain the \mathbf{q} representation

$$H(\mathbf{q}, t) = H(\mathbf{q} + \frac{e}{\hbar} \mathbf{A}(t)) . \quad (1.14)$$

With the gauge-invariant crystal momentum

$$\mathbf{k} = \mathbf{q} + \frac{e}{\hbar} \mathbf{A}(t) . \quad (1.15)$$

The parameter-dependent Hamiltonian can be simply written as $H(\mathbf{k}(\mathbf{q}, t))$. Hence the eigenstates of the time-dependent Hamiltonian can be labeled by a single parameter \mathbf{k} . Moreover, because $\mathbf{A}(t)$ preserves the translational symmetry, \mathbf{q} is still a good quantum number and is a constant of motion $\dot{\mathbf{q}} = 0$. It then follows from Eq. (1.15) that \mathbf{k} satisfies the following equation of motion

$$\dot{\mathbf{k}} = -\frac{e}{\hbar} \mathbf{E} . \quad (1.16)$$

To capture the adiabatic current induced by the variation of external potentials, we calculate the wave function up to first order in the rate of the change of the Hamiltonian (standard first order correction to wavefunction as shown in the appendix of [234])

$$|u_n\rangle - i\hbar \sum_{m \neq n} \frac{|u_m\rangle \langle u_m | \frac{\partial u_n}{\partial t} \rangle}{E_n - E_m} . \quad (1.17)$$

Here u_n and E_n is the wavefunction and energy for n -th band of ground state Hamiltonian. The velocity operator is obtained via $v(q, t) = \frac{i}{\hbar} [H, r] = \partial H(q, t) / \partial (\hbar q)$. Hence, the average velocity in q to first order is

$$v_n(q) = \frac{\partial E_n(q)}{\hbar \partial q} - i \sum_{m \neq n} \left\{ \frac{\langle u_n | \frac{\partial H}{\partial q} | u_m \rangle \langle u_m | \frac{\partial u_n}{\partial t} \rangle}{E_n - E_m} - \text{c.c.} \right\} , \quad (1.18)$$

where c.c. denotes the complex conjugate. With $\langle u_n | \partial H / \partial q | u_m \rangle = (E_n - E_m) \langle \partial u_n / \partial q | u_m \rangle$ and the identity $\sum_n |u_n\rangle \langle u_n| = 1$, we find

$$v_n(q) = \frac{\partial E_n(q)}{\hbar \partial q} - i \left[\left\langle \frac{\partial u_n}{\partial q} \left| \frac{\partial u_n}{\partial t} \right\rangle - \left\langle \frac{\partial u_n}{\partial t} \left| \frac{\partial u_n}{\partial q} \right\rangle \right] . \quad (1.19)$$

The second term is exactly the Berry curvature Ω_{qt}^n defined in the parameter space (q, t) . To transfer it to k -space, we use the relation from Eq. 1.14 and 1.15

$$\begin{aligned} \partial H / \partial q &= \partial H / \partial k, \\ \partial H / \partial t &= (\partial H / \partial k) (\partial k / \partial t) = -(e/\hbar) E \partial H / \partial k \end{aligned} \quad (1.20)$$

Thus the velocity in a given \mathbf{k} is given by

$$\mathbf{v}_n(\mathbf{k}) = \frac{\partial E_n(\mathbf{k})}{\hbar \partial \mathbf{k}} - \frac{e}{\hbar} \mathbf{E} \times \boldsymbol{\Omega}_n(\mathbf{k}), \quad (1.21)$$

where $\boldsymbol{\Omega}_n(\mathbf{k})$ is the Berry curvature of the n th band:

$$\boldsymbol{\Omega}_n(\mathbf{k}) = i \langle \nabla_{\mathbf{k}} u_n(\mathbf{k}) | \times | \nabla_{\mathbf{k}} u_n(\mathbf{k}) \rangle. \quad (1.22)$$

In addition to the usual band dispersion contribution, an extra term previously known as an anomalous velocity also contributes to electron velocity. This velocity is always transverse to the electric field, which will give rise to a Hall current under time reversal breaking condition. The overall semiclassical equations of motion for an electron wavepacket in a metal are thus written as

$$\begin{aligned} \dot{\mathbf{r}} &= \frac{1}{\hbar} \nabla_{\mathbf{k}} E_{\mathbf{k}} - \dot{\mathbf{k}} \times \boldsymbol{\Omega}, \\ \hbar \dot{\mathbf{k}} &= -e \mathbf{E} - e \dot{\mathbf{r}} \times \mathbf{B}, \\ \boldsymbol{\Omega}_n(\mathbf{k}) &= i \langle \nabla_{\mathbf{k}} u_n(\mathbf{k}) | \times | \nabla_{\mathbf{k}} u_n(\mathbf{k}) \rangle. \end{aligned} \quad (1.23)$$

With the identity $\langle u_n | \partial H / \partial q | u_m \rangle = (E_n - E_m) \langle \partial u_n / \partial q | u_m \rangle$, the Eq. 1.23 could be directly transferred to Eq. 1.11 when \hat{A} is the current density operator, which tells us that the semiclassical approach gives the identical description as the Kubo formula from full quantum mechanical equations at least in the first order.

1.2.3 Berry curvature formalism for anomalous Hall effect and spin Hall effect

The band-structure topology and electronic response functions are commonly characterised by the Berry curvature [234] in the momentum(k) space. A well-established example is the anomalous Hall effect (AHE) [142] as an intrinsic property originating in the band structure, in which the Berry curvature integrated over the occupied states at the thermodynamic equilibrium results in the Hall conductivity. The AHE and its quantised version have recently been observed in time-reversal symmetry (TRS)-breaking topological materials—for example, magnetically doped topological insulators (TIs) [24, 117, 256] and magnetic Weyl semimetals [16, 237, 243, 245].

The AHE is characterized by a transverse voltage generated by a longitudinal charge current usually in a ferromagnetic (FM) metal. In the main section, we have derived the

Kubo formula and semiclassical equation for the response of charge current to external electrical field. A further generalized expression for the intrinsic contribution to anomalous Hall conductivity ($\sigma_{\alpha\beta}$) is written as

$$\sigma_{\alpha\beta} = -\frac{e^2}{\hbar} \sum_n \int_{BZ} \frac{d^3\vec{k}}{(2\pi)^3} f_n(\vec{k}) \Omega_n(\vec{k}),$$

$$\Omega_n(\vec{k}) = 2i\hbar^2 \sum_{m \neq n} \frac{\langle u_n(\vec{k}) | \hat{v}_\alpha | u_m(\vec{k}) \rangle \langle u_m(\vec{k}) | \hat{v}_\beta | u_n(\vec{k}) \rangle}{(E_n(\vec{k}) - E_m(\vec{k}))^2}, \quad (1.24)$$

where $\hat{v}_{\alpha(\beta,\gamma)} = \frac{1}{\hbar} \frac{\partial \hat{H}}{\partial k_{\alpha(\beta,\gamma)}}$ is the velocity operator with $\alpha, \beta, \gamma = x, y, z$. $f_n(\vec{k})$ is the Fermi-Dirac distribution. $|u_n(\vec{k})\rangle$ and $E_n(\vec{k})$ are the eigenvector and eigenvalue of the Hamiltonian $\hat{H}(\vec{k})$, respectively. $\Omega_n(\vec{k})$ is the Berry curvature in momentum space, and the corresponding AHC $\sigma_{\alpha\beta}$ can be evaluated by summarizing the Berry curvature over the Brillouin zone (BZ) for all the occupied bands. Here $\sigma_{\alpha\beta}$ corresponds to a 3×3 matrix element and indicates a transverse Hall current j_α generated by a longitudinal electric field E_β , which satisfies $J_\alpha = \sigma_{\alpha\beta} E_\beta$.

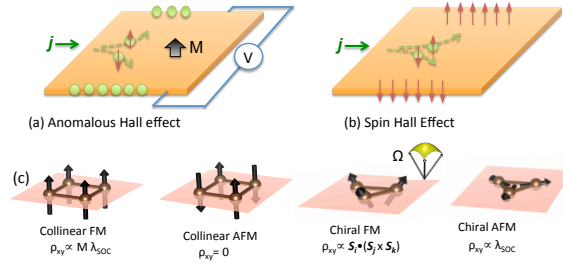


Figure 1.2: Schematic illustrations of (a) the anomalous Hall effect and (b) the spin Hall effect from the viewpoint of spin-dependent Mott scattering. (c) The anomalous Hall effect in collinear FM, collinear AFM, chiral FM, and chiral AFM systems. ρ_{xy} , M , λ_{SOC} and $S_i \cdot (S_j \times S_k)$ represent the anomalous Hall resistivity, magnetization, strength of SOC and the scalar spin chirality, respectively.

The AHE can be generalized to the case of the spin Hall effect (SHE) in nonmagnetic materials in which Mott scattering leads to the deflection of spin-up and -down charge carriers in opposite directions, owing to spin-orbit coupling (SOC), as illustrated in Fig. 5.1. Thus, a longitudinal charge current can generate opposite spin accumulations along opposing edges in the transverse direction to the current. On the contrary, a spin current can also induce a transverse voltage drop, in an effect called the inverse SHE. Both the

AHE and SHE are of particular interest for spintronic applications [74, 129, and references therein] in which spin currents can be used to manipulate magnetic moments, for example, switching the state of magnetization of magnetic nano-elements, or for inducing the very efficient motion of domain walls [158, 247].

By extending the Berry curvature to spin Berry curvature, the intrinsic spin Hall conductivity (SHC) can be obtained by replacing the velocity operator with the spin current operator $\hat{J}_\alpha^\gamma = \frac{1}{2}\{\hat{v}_\alpha, \hat{s}_\gamma\}$, where \hat{s}_γ is the spin operator. The SHC then has the form of

$$\begin{aligned}\sigma_{\alpha\beta}^\gamma &= \frac{e}{\hbar} \sum_n \int_{BZ} \frac{d^3\vec{k}}{(2\pi)^3} f_n(\vec{k}) \Omega_{n,\alpha\beta}^\gamma(\vec{k}), \\ \Omega_{n,\alpha\beta}^\gamma(\vec{k}) &= 2i\hbar^2 \sum_{m \neq n} \frac{\langle u_n(\vec{k}) | \hat{J}_\alpha^\gamma | u_m(\vec{k}) \rangle \langle u_m(\vec{k}) | \hat{v}_\beta | u_n(\vec{k}) \rangle}{(E_n(\vec{k}) - E_m(\vec{k}))^2},\end{aligned}\tag{1.25}$$

$\Omega_{n,\alpha\beta}^\gamma(\vec{k})$ is referred to as the spin Berry curvature in the following, in order to distinguish it from the Berry curvature $\vec{\Omega}_n(\vec{k})$. The SHC ($\sigma_{\alpha\beta}^\gamma$; $\alpha, \beta, \gamma = x, y, z$) is a third-order tensor ($3 \times 3 \times 3$) and represents the spin current $J s_\alpha^\gamma$ generated by an electric field \vec{E} via $J s_\alpha^\gamma = \sigma_{\alpha\beta}^\gamma E_\beta$, where $J s_\alpha^\gamma$ flows along the α -direction with the spin-polarization along the γ -direction and E_β is the β -component of the electric field \vec{E} . In addition, the unit of SHC differs from that of the AHC by $\frac{\hbar}{2e}$, where $\hbar/2$ is the spin angular momentum and e is the electron charge. Thus, the unit of SHC is $(\hbar/e)(\Omega \cdot \text{cm})^{-1}$.

Starting from ground-state DFT calculation, we develop a numerical programme to build the highly symmetric Wannier Hamiltonians and calculate the linear response susceptibility from the integral in momentum space. With a highly efficient parallel and vectorised algorithm, we could evaluate a real material system with over 1000 bands for a very dense momentum space mesh up to $500 * 500 * 500$ for the integrals of Eq. 1.24-1.25. The low numerical cost and automatic Wannier Hamiltonian generation make it possible to search all possible materials and build a database of transport properties from the simulation point of view.

1.3 Nonlinear, second order response

It is well known that, in the linear response regime, the anomalous Hall effect vanishes in the presence of TRS, because TRS forces the Berry curvature to be odd with respect to k , i.e. $\Omega^n(k) = -\Omega^n(-k)$ where n is the band index. In the nonlinear response regime, however, an intriguing nonlinear anomalous Hall effect (NLAHE) can still survive in the

presence of TRS but in the absence of inversion symmetry [191]. When an electric field E drives a current through a crystal in the steady state, the system is out of equilibrium and the Fermi surface exhibits an effective shift in k -space. Therefore, the Fermi occupations at k and $-k$ are no longer necessarily the same. This leads to a net Berry curvature summed on the nonequilibrium Fermi surface, i.e. an anomalous Hall conductivity proportional to E and the relaxation time τ . Thus, the Hall voltage is estimated to be quadratic, rather than linear, to the longitudinal electric field E . The NLAHE was derived at the zero-frequency limit of the nonlinear photocurrent generation [140, 191]. Although it is a nonequilibrium property, the NLAHE can be described by a geometric quantity at the equilibrium Fermi surface, the Berry curvature dipole (BCD) [191].

1.3.1 Nonlinear Hall effect from Berry curvature dipole

To calculate such a nonlinear Hall current, first we introduce the semiclassical approach with Berry curvature. Starting from the semiclassical velocity from Eq.1.23 without magnetic field, we perform the integral with Fermi-Dirac distribution function

$$\begin{aligned} \mathbf{j} &= -e \int_{\mathbf{k}} f(\mathbf{k}) \mathbf{v}, \\ \mathbf{v} &= \mathbf{v}_0 + \mathbf{v}_1 = \frac{1}{\hbar} \nabla_{\mathbf{k}} E_{\mathbf{k}} - \dot{\mathbf{k}} \times \boldsymbol{\Omega}, \\ \dot{\mathbf{k}} &= -e \mathbf{Re}(E(t)) \end{aligned} \tag{1.26}$$

Here $\mathbf{E}(t) = \mathbf{E}e^{i\omega t}$ is the driving electric field as a function of time but with no dependence on space, which could be introduced by DC (AC) electrical field or light radiation, \mathbf{v}_0 and \mathbf{v}_1 are the group velocity and anomalous velocity. The Fermi-Dirac distribution function f is obtained from Boltzmann transport equations under constant relaxation time approximation.

$$-e\tau \mathbf{E} \partial_{\mathbf{k}} f + \tau \partial_t f = f_0 - f, \tag{1.27}$$

here $\partial_{\mathbf{k}} f = \partial f / \partial \mathbf{k}$, $\partial_t f = \partial f / \partial t$, and f_0 is the equilibrium distribution, which the lowest order function regarding electrical field. Since we would need to calculate the second order current, the distribution function is expanded until the second order as $f = \text{Re}\{f_0 + f_1 + f_2\}$

[191]. The recursive relation is give by

$$\begin{aligned} f_1 &= f_1^\omega e^{i\omega t}, \quad f_1^\omega = \frac{e\tau \mathcal{E}_a \partial_a f_0}{1 + i\omega\tau}, \\ f_2 &= f_2^0 + f_2^{2\omega} e^{2i\omega t}, \quad f_2^0 = \frac{(e\tau)^2 \mathcal{E}_a^* \mathcal{E}_b \partial_{ab} f_0}{2(1 + i\omega\tau)}, \\ f_2^{2\omega} &= \frac{(e\tau)^2 \mathcal{E}_a \mathcal{E}_b \partial_{ab} f_0}{2(1 + i\omega\tau)(1 + 2i\omega\tau)}. \end{aligned} \quad (1.28)$$

To obtain a second order current, one needs to combine the first order Fermi-Dirac distribution function with anomalous velocity, or second order Fermi-Dirac distribution function with group velocity. The overall second order current is:

$$j_a^2 = \frac{e^2}{2} \int_k \varepsilon_{abc} \Omega_b \mathcal{E}_c^* f_1^\omega - e \int_k f_2^0 \partial_a \epsilon(k). \quad (1.29)$$

The j_a^2 describes a DC current, which scales quadratically with the electrical field. The second terms in j_a^2 are proportional to the integral of a three-index tensor, $\mathbf{v}_0 \partial_{bc} f_0(k)$. Since \mathbf{v}_0 is odd under time reversal, while the second order derivative $\partial_{bc} f_0$ is even under time reversal, the overall second terms in j^0 and $j^{2\omega}$ are odd under time reversal. This contribution would be quite important in magnetic systems, especially in antiferromagnets with combined inversion and time reversal symmetry. They have zero Berry curvature in momentum space but a second order current would still arise from the time reversal odd term. Since we are mainly focused on time reversal symmetric materials in current study, the only surviving term is the one associated with the Berry curvature.

By writing $j_a^2 = \chi_{abc} \mathcal{E}_b \mathcal{E}_c^*$, $j_a^{2\omega} = \chi_{abc} \mathcal{E}_b \mathcal{E}_c$, one has that:

$$\chi_{abc} = \varepsilon_{adc} \frac{e^3 \tau}{2(1 + i\omega\tau)} \int_k (\partial_b f_0) \Omega_d. \quad (1.30)$$

With the differential function $\partial_b f_0$, it is obvious that a nonzero j^2 would require the presence of a finite Fermi surface, which is only possible in metallic system. Since the Berry curvature is odd under time reversal, a differential transformation on Eq. (1.30) gives the final Berry curvature dipole expression:

$$\chi_{abc} = -\varepsilon_{adc} \frac{e^3 \tau}{2(1 + i\omega\tau)} \int_k f_0 (\partial_b \Omega_d). \quad (1.31)$$

$$D_{ab} = \int_k f_0 (\partial_a \Omega_b). \quad (1.32)$$

Here $\partial_a \Omega_b$ is the Berry curvature dipole in momentum space, and its integral D_{ab} gives the second order conductivity. In transport region, we note this second order current would be proportional to the relaxation time, which gives a constant Hall angle with weak dependence on temperature and possible disorder.

It is kind of obvious that a nonzero Berry dipole and NLAHE would require inversion symmetry breaking because of the nature of second order response. But the searching of suitable materials that would hold a sizeable nonlinear current for experimental investigation is yet to be done. Aiming for the final experimental realisation of NLAHE, we calculate the BCD for the three-dimensional (3D) WSMs based on *ab initio* band structures [266] and also for two-dimensional transition-metal dichalcogenides W(Mo)Te₂ [265], and observe that the Berry dipole is strongly enhanced around the Weyl nodes in 3D structures and the topological transition critical points in 2D structures. WTe₂ and MoTe₂ are a class of readily synthesisable layered materials. Originally highlighted for the semiconducting band gap of exfoliated monolayers, they have recently been recognised as topological materials. As revealed in this work, they indeed generate a large BCD. As they are widely studied in transport experiments, 2D WTe₂ and MoTe₂ are ideal candidates for the experimental investigation of the NLAHE.

1.3.2 Second order Kubo formula for optical response

Besides the intraband (Fermi surface) effect from Berry curvature dipole as discussed above, the monopole-type Berry curvature of WSMs can also lead to appealing nonlinear interband optical effects closely related to the Berry phase in the band structure [40, 138, 139, 187, 252]. Under strong light irradiation, a noncentrosymmetric material exhibits photocurrents as nonlinear functions of the electric field of the light and also generates higher harmonic frequencies, referred to as photogalvanic effects. The photogalvanic effect rectifies light to DC currents and often plays a crucial role in optical devices and solar cells beyond the p-n junction platform [34, 68, 248]. Under linearly polarised light, the induced photocurrent is usually called a shift current, which originates from the charge centre shift between the valence and conduction bands in the optical excitation. Under circularly polarised light, the photocurrent generation is referred to as the circular photogalvanic effect (CPGE). It can be expressed in the formalism of Berry curvature and Berry connection [139, 187, 252], revealing a topological nature. Therefore, WSMs have recently been theoretically investigated for such nonlinear optical phenomena [?, 21, 22, 38, 61, 66, 75, 82, 83, 91, 140, 171, 191, 202, 249, 266]. In these works, two-band

or four-band effective models are commonly adopted to reveal the relation between the photocurrent and the Weyl bands. For example, the tilt of Weyl cones is proposed to play an essential role in generating a net CPGE current by considering the two-band transition from the occupied Weyl band to the empty Weyl band [22].

Starting with the Kubo-like resonant formula, we would derive the fully three-band formula to describe both the shift current and CPGE, which scale in the second order regarding electrical field.

In Eq. 1.3, the density operator is only treated in the linear order, here we expand the Eq. 1.1 to second order and solve it by iteration:

$$\begin{aligned}\hat{\rho}(t) &= \hat{\rho}_0 + \hat{\rho}_1(t) + \hat{\rho}_2(t) + \dots, \\ \hat{\rho}_{n+1} &= -\frac{i}{\hbar} \int_{-\infty}^t dt' e^{\epsilon/\hbar t'} \hat{U}(t') [\hat{\rho}_n(t'), \hat{F}(t')] \hat{U}^{-1}(t').\end{aligned}\tag{1.33}$$

Different from the case of linear response in a DC field, here we choose the Weyl gauge with scalar potential equal to zero, and neglect the spatial variations of the vector potential $A(r, t)$ assuming the electric dipole approximations. Then we have the Hamiltonian and perturbation field as:

$$\begin{aligned}\hat{H} &= \hat{H}_0 + \hat{F}(t) \\ \hat{F}(t) &= \hat{J} \cdot \mathbf{A}(t) + e^2/(2m_0 V) \mathbf{A}^2 \\ \hat{J} &= -e\hat{v}/V \\ \mathbf{A}(t) &= (\mathbf{E}_0/\omega) \cos(\omega t)\end{aligned}\tag{1.34}$$

The advantage of Weyl gauge is that we avoid the position operator associated with electrical field, and thus formulate the response solely with velocity operator. (Note there are also other approaches using the so called length gauge [187], which give the identical expressions for DC photocurrent in the end.) The DC photocurrent is linearly in the light radiation and quadratic in the light electrical field, thus only depends on $\hat{\rho}_2(t)$ (obtained from Eq. 1.33 and 1.3). In analogy to Eq. 1.5, the DC photocurrent density at $t = 0$ is obtained by

$$\begin{aligned}
 j(0) &= \text{Tr}[\hat{\rho}_2 \hat{J}] \\
 &= - \int_{-\infty}^0 dt' \int_{-\infty}^0 ds (V/\hbar\omega)^2 e^{\frac{\epsilon}{\hbar}(t'+s)} E_0^2 \text{Tr}(\rho_0 \{ \hat{J}_D(0), [\hat{J}_D(t'), \hat{J}_D(t' + s)] \}) \\
 &= - \int_{-\infty}^0 dt' \int_{-\infty}^0 ds (V/\hbar\omega)^2 e^{\frac{\epsilon}{\hbar}(t'+s)} E_0^2 \langle \{ \hat{J}_D(0), [\hat{J}_D(t'), \hat{J}_D(t' + s)] \} \rangle_0,
 \end{aligned} \tag{1.35}$$

with $\hat{J}_D = \hat{U}(t) \hat{J} \hat{U}(t)^{-1}$ denoting the current operator in Dirac picture. Expand Eq. 1.35 by inserting the identity $\sum_m |m\rangle \langle m| = 1$ and $\sum_l |l\rangle \langle l| = 1$, then perform the integral over time domain in analogy to Eq. 1.7, we would obtain the expression in terms of ground state wavefunctions:

$$\begin{aligned}
 \sigma_{ab}^c &= \frac{|e|^3}{8\pi^3\omega^2} \text{Re} \left\{ \sum_{\Omega=\pm\omega} \sum_{l,m,n} \int_{BZ} d^3k (f_l - f_n) \right. \\
 &\quad \left. \frac{\langle n|\hat{v}_a|l\rangle}{E_n - E_l + \hbar\Omega - i\epsilon} \left(\frac{\langle l|\hat{v}_b|m\rangle \langle m|\hat{v}_c|n\rangle}{E_n - E_m - i\epsilon} - \frac{\langle l|\hat{v}_c|m\rangle \langle m|\hat{v}_b|n\rangle}{E_m - E_l - i\epsilon} \right) \right\}.
 \end{aligned} \tag{1.36}$$

The conductivity ($\sigma_{ab}^c; a, b, c = x, y, z$) is a third rank tensor and represents the photocurrent J^c generated by an electrical field \vec{E} via $J^c = \sigma_{ab}^c E_a^* E_b$. For the second term $\frac{\langle l|\hat{v}_c|m\rangle \langle m|\hat{v}_b|n\rangle}{E_m - E_l - i\epsilon}$ in Eq. 1.36, we apply the exchange of l and n together with the prefactor, then it becomes identical as the first term. Finally we obtain the brief expression for photocurrent density as:

$$\begin{aligned}
 \sigma_{ab}^c &= \frac{|e|^3}{8\pi^3\omega^2} \text{Re} \left\{ \sum_{\Omega=\pm\omega} \sum_{l,m,n} \int_{BZ} d^3k (f_l - f_n) \right. \\
 &\quad \left. \frac{\langle n\vec{k}|\hat{v}_a|l\vec{k}\rangle \langle l\vec{k}|\hat{v}_b|m\vec{k}\rangle \langle m\vec{k}|\hat{v}_c|n\vec{k}\rangle}{(E_n - E_m - i\epsilon)(E_n - E_l + \hbar\Omega - i\epsilon)} \right\}.
 \end{aligned} \tag{1.37}$$

With the first-principle approach, which accounts for the realistic material band structures, we could provide a better understanding of the optical response compared with the effective kp model approach in Chapter. 7

1.4 Structure of the thesis

In this thesis, we propose the theoretical framework of Berry-phase-related linear and nonlinear response phenomena and explore its relationship with band topology. With the

accurate description of response formula and the *ab – initio* Wannier model parameter, we make quantitative predictions of realistic materials and compare our results with those of recent experiments, which are consistent even for the nonlinear optical response.

In Chapter 2, we introduce the theoretical framework of DFT, and the full-potential local-orbital (FPLO) approach, followed by the procedure for symmetric Wannier function generation. In Chapter 3, we show the magnetic WSM phase in Ti_2MnAl , an inverse Heusler with large anomalous Hall effect, and introduce the general theory of linear response and the electron transport with Berry curvature. In Chapter 4, various linear transport phenomena of spin current are formulated and calculated from the Berry phase approach based on the *ab – initio* wavefunction. We first introduce the spin Hall effect in the IrO_2 family of Dirac nodal-line materials and analyse the contribution from typical band structures such as nodal-line bands. Subsequently, with the knowledge of the relation between spin Berry curvatures, we propose the p-band topological semimetal InBi with giant spin Hall and Nernst effects as the ideal material for spin current generation. In Chapter 5, we study the linear response of spin current in antiferromagnetic materials and its relation to magnetic symmetry: spin Hall effect in noncollinear antiferromagnetic Mn_3X ($\text{X}=\text{Ga}, \text{Ge}, \text{Sn}$, and $\text{Rh}, \text{Ir}, \text{Pt}$) without spin-orbital coupling, spin-polarised current in noncollinear antiferromagnets, and its application to antiferromagnetic spintronics. To connect the transport properties with lattice symmetry, we also provide a detailed description of the linear response tensor shape from space group operations both with and without spin-orbital coupling. In Chapter 6, we present the Berry-dipole-induced NLAHE in 2D and 3D topological systems and present the ideal platform to observe NLAHE. In Chapter 7, we calculate the photogalvanic effect in WSM TaAs from the second-order Kubo formula and analyse the optical transition from Weyl nodes by separating the full response to two-band and three-band parts. A summary of this work and an outlook on further work are given in Chapter 8.

1.5 List of publications

The results presented in this thesis are mainly contained from the following list of articles.

1. Strong spin-Hall and Nernst effects in a p-band semimetal
Y. Zhang, Q. Xu, K. Koepernik, J. Gooth, J. v. d. Brink, C. Felser, Y. Sun
arXiv preprint arXiv:1805.12049
2. Electrically tuneable nonlinear anomalous Hall effect in two-dimensional transition-

metal dichalcogenides WTe₂ and MoTe₂

Y. Zhang, J. v. d. Brink, C. Felser, B. Yan

2D Materials. 5 044001 (2018)

3. Photogalvanic Effect in Weyl Semimetals from First Principles

Y. Zhang, H. Ishizuka, J. v. d. Brink, C. Felser, B. Yan, N. Nagaosa

Physical Review B 97, 241118(R) (2018)

4. Prediction of a magnetic Weyl semimetal without spin-orbit coupling and strong anomalous Hall effect in the Heusler compensated ferrimagnet Ti₂MnAl

W. Shi, L. Muechler, K. Manna, **Y. Zhang**, K. Koepernik, R. Car, J. v. d. Brink, C. Felser, Y. Sun

Physical Review B 97 (6), 060406 (2018)

5. Spectral dynamics of topological shift-current in ferroelectric semiconductor SbSI

M. Sotome, M. Nakamura, J. Fujioka, M. Ogino, Y. Kaneko, T. Morimoto, **Y. Zhang**, M. Kawasaki, N. Nagaosa, Y. Tokura, N. Ogawa

arXiv preprint arXiv:1801.10297

6. Berry curvature dipole in Weyl semimetal materials: An ab initio study

Y. Zhang, Y. Sun, B. Yan

Physical Review B 97 (4), 041101 (2018)

7. From colossal to zero: Controlling the Anomalous Hall Effect in Magnetic Heusler Compounds via Berry Curvature Design

K. Manna, L. Muechler, TH. Kao, R. Stinshoff, **Y. Zhang**, N. Kumar, G. Kreiner, K. Koepernik, R. Car, J. Kbler, G. H. Fecher, C. Shekhar, Y. Sun, C. Felser

arXiv preprint arXiv:1712.10174

8. Spin-Polarized Current in Noncollinear Antiferromagnets

J. Zelezny, **Y. Zhang**, C. Felser, B. Yan

Physical Review Letters 119 (18), 187204 (2017)

9. Emergent Weyl Fermion Excitations in TaP Explored by Ta 181 Quadrupole Resonance

H. Yasuoka, T. Kubo, Y. Kishimoto, D. Kasinathan, M. Schmidt, B. Yan, **Y. Zhang**, H. Tou, C. Felser, A. P. Mackenzie, M. Baenitz

Physical Review Letters 118 (23), 236403 (2017)

10. Dirac nodal lines and induced spin Hall effect in metallic rutile oxides
Y. Sun, **Y. Zhang**, CX. Liu, C. Felser, B. Yan
Physical Review B 95 (23), 235104 (2017)
11. Spin Hall effect emerging from a chiral magnetic lattice without spin-orbit coupling
Y. Zhang, J. Zelezny, Y. Sun, J. v. d. Brink, B. Yan
New Journal of Physics. 20 (2018)
12. Strong anisotropic anomalous Hall effect and spin Hall effect in the chiral antiferromagnetic compounds Mn_3X (X= Ge, Sn, Ga, Ir, Rh, and Pt)
Y. Zhang, Y. Sun, H. Yang, J. Zelezny, S. P. P. Parkin, C. Felser, B. Yan
Physical Review B 95 (7), 075128 (2018)
13. Topological Weyl semimetals in the chiral antiferromagnetic materials Mn_3Ge and Mn_3Sn
H. Yang, Y. Sun, **Y. Zhang**, WJ. Shi, S. S. P. Parkin, B. Yan
New Journal of Physics 19 (1), 015008 (2017)
14. Strong intrinsic spin Hall effect in the TaAs family of Weyl semimetals
Y. Sun, **Y. Zhang**, C. Felser, B. Yan
Physical Review Letters 117 (14), 146403 (2016)
15. Giant facet-dependent spin-orbit torque and spin Hall conductivity in the triangular antiferromagnet IrMn_3
W. Zhang, W. Han, SH. Yang, Y. Sun, **Y. Zhang**, B. Yan, S. S. P. Parkin
Science Advances 2 (9), e1600759 (2016)

2 Density functional theory and Wannier approach

In this chapter, we provide a brief introduction to the ground-state DFT and Wannier function approach. We review the basis of DFT from the Hohenberg–Kohn theorems and the Kohn–Sham formalism [?, ?], and subsequently, we show the four-component DFT from Dirac equation and the FPLO formalism.

As the Dirac equation and even the non-relativistic Schrödinger equation can accurately describe a solid system, we start from the total non-relativistic quantum mechanical Hamiltonian for many-body systems made of ions and electrons and thereafter add the relativistic effect as the perturbation.

$$\begin{aligned}
 \hat{H}_{tot} &= \hat{H}_n + \hat{H}_e + \hat{H}_{nn} + \hat{H}_{ee} + \hat{V}_{ne} \\
 &= - \sum_I \frac{\hbar^2}{2M_I} \nabla_I^2 - \sum_i \frac{\hbar^2}{2m_i} \nabla_i^2 + \frac{e^2}{2} \sum_I \sum_{J \neq I} \frac{Z_I Z_J}{|\mathbf{R}_I - \mathbf{R}_J|} \\
 &\quad + \frac{e^2}{2} \sum_i \sum_{j \neq i} \frac{1}{|\mathbf{r}_i - \mathbf{r}_j|} - e^2 \sum_I \sum_j \frac{Z_I}{|\mathbf{R}_I - \mathbf{r}_j|}
 \end{aligned} \tag{2.1}$$

Here, $M(m)$ and $R(r)$ denote the mass and location coordinates of nuclei (electrons), respectively, Z represents the nuclear charge, e is the elementary charge, i, j are the indices for electrons, and I, J are the indices for nuclei. The first two terms represent the kinetic energy, the third and fourth terms are interactions between nuclei (electrons), and the final term is the interaction between nuclei and electrons. The above Hamiltonian describes a complicated many-body system with $3N$ (N is the total number of electrons and nuclei) coupled spatial degrees of freedoms, that we cannot hope to solve exactly even with the most powerful existing supercomputer.

Several approximations are introduced to simplify the situation. In the first step, we separate the total Hamiltonian into electronic motion and nuclear motion, as the electrons

are lighter than the nuclei by three orders of magnitude and there would be a strong separation of time scales between the electronic and nuclear motions. With the so-called Born–Oppenheimer approximation, we can write the wavefunction of the solid system in a quasi-separable form as follows:

$$\Psi(\mathbf{R}, \mathbf{r}) = \Psi_n(\mathbf{R}) \Psi_e(\mathbf{R}, \mathbf{r}) \quad (2.2)$$

Here $\Psi_n(\mathbf{R}, \mathbf{r})$ and $\Psi_e(\mathbf{R})$ are the wavefunctions of electrons and atomic nuclei, respectively.

2.1 Hohenberg-Kohn theorem: electron density as a basic variable

After the Born–Oppenheimer approximation, we obtain the electron Hamiltonian with fixed nuclei as

$$\begin{aligned} \hat{H}_e = & - \sum_i \frac{\hbar^2}{2m_i} \nabla_i^2 + \sum_i V_{ext}(\mathbf{r}_i) \\ & + \frac{e^2}{2} \sum_i \sum_{j \neq i} \frac{1}{|\mathbf{r}_i - \mathbf{r}_j|} \end{aligned} \quad (2.3)$$

where V_{ext} is the expression for the interaction with nuclei in addition to any external potential. We now discuss how to determine the ground state of such an electron Hamiltonian. The basic idea is to use spatial electron density function instead of electron wavefunctions and reduce the degrees of freedom from $3N$ to 3 (N is the number of electrons), which arising from the fundamental tenet of DFT (also known as Hohenberg-Kohn theorem): any property of a system of many interacting particles can be viewed as a functional of the ground state density $n(\mathbf{r})$.

Fermi and Thomas first realised that electron density can determine the ground state and other properties of a many-electron system and applied the electron density distribution $n(\mathbf{r})$ to atoms. Subsequently, Dirac showed that exchange effects could be incorporated into the aforementioned case and proved that a ‘density function’ determines the entire state of the atoms within the Hartree–Fock approximation; he formally stated that ‘it is not necessary to specify the individual three-dimensional wavefunction’ [?].

This simplification started from the Thomas–Fermi–Dirac approximation mentioned above and was subsequently formulated by Hohenberg and Kohn in the framework of two Hohenberg–Kohn theorems (HK theorems). The HK theorems relate to any system consisting of electrons moving under the influence of an external potential; here, we refer to them without proof (the detailed derivation can be found in Ref. [?]):

Theorem 1: For any system of interacting particles in an external potential $V_{ext}(r)$, the external potential (and hence the total energy) is a unique functional, except for a constant, of the ground-state electron density $n(\mathbf{r})$.

Theorem 2: The universal functional for the energy $E(n)$ in terms of the density $n(\mathbf{r})$ can always be defined for any external potential $V_{ext}(\mathbf{r})$. The ground-state energy of the system is the global minimum value of the defined functional, and the input density is the true ground-state density if and only if the functional is minimised.

The original HK theorems assume that the ground state is non-degenerate, and there is a technical issue called the V-representability problem. During the variational process, it is assumed that there is a corresponding $V_{ext}(\mathbf{r})$ for every reasonable ground-state density $n(\mathbf{r})$ associated with the antisymmetric ground-state wavefunction. Thus, every density in the HK functional is V-representable and the conditions for such densities are not known in general. Levy and Lieb (LL) proposed a new Levy–Lieb formulation as the restatement of the HK functional and eliminated the restriction that the proof of HK theorems requires a non-degenerate ground state. The LL functional is based on an operational definition: the minimum of the sum of kinetic and interaction energies for all possible wavefunctions having the given density $n(\mathbf{r})$. Since the LL functional is defined for any density $n(\mathbf{r})$ derivable from a wavefunction Ψ_e , it is then termed N-representability, and the existence of such a wavefunction for any density satisfying simple conditions is known [60], as discussed in Sec. 6.5 of Ref. [?].

2.1.1 Kohn-Sham formalism

The above HK theorems do not provide us any computational approximation for the construction of a density functional, and Kohn and Sham (KS) subsequently proposed the KS equation to map the interacting electron Hamiltonian to a non-interacting Hamiltonian by collecting all the unknown parts of the functional to the exchange and correlation (xc) energy functional E_{xc} , which forms the basis of DFT calculations.

The interacting electron functional can be written as follows:

$$E[n] = \int V(\mathbf{r})n(\mathbf{r})d\mathbf{r} + \frac{1}{2} \iint d\mathbf{r}d\mathbf{r}' \frac{n(\mathbf{r})n(\mathbf{r}')}{|\mathbf{r} - \mathbf{r}'|} + T_s[n] + E_{xc}[n], E_{xc}[n] = \int n(\mathbf{r})\epsilon_{xc}d\mathbf{r} \quad (2.4)$$

Here, the second and third terms represent the Hartree interaction energy and kinetic energy for the non-interacting system, respectively, and E_{xc} is the exchange-correlation energy functional, which includes the difference between the true kinetic energy of interacting systems and that of the non-interacting systems with the same density.

We write the density from the Kohn-Sham ansatz as follows:

$$n(\mathbf{r}) = \sum_i^N |n_i \psi_i(\mathbf{r})|^2$$

(n_i is the occupation number).

Thus, the ground-state energy is obtained by minimising the energy functional; after performing the variation, we obtain the famous KS equation as follows:

$$\left\{ -\frac{1}{2} \nabla^2 + [v(\mathbf{r}) + \int \frac{n(\mathbf{r}')}{|\mathbf{r} - \mathbf{r}'|} d\mathbf{r}' + v_{xc}(n(\mathbf{r}))] \right\} \psi_i(\mathbf{r}) = \epsilon_i \psi_i(\mathbf{r}). \quad (2.5)$$

Under the uniform electron gas assumption, we have $v_{xc} = d(E_{xc})/dn(\mathbf{r})$ as the exchange and correlation potential of a uniform electron gas of the density $n(\mathbf{r})$. $\psi_i(\mathbf{r})$ and ϵ_i are the wavefunction and energy of the Kohn-Sham orbital of electron, respectively.

We observe that the projection theories are still exact and have a clear expression, except for the unknown $E_{xc}(\mathbf{r})$. From the KS-orbitals, the density is calculated first, followed by the potential. After the convergence of self-consistent calculation, we obtain the final total energy and density.

2.1.2 Exchange-correlation functional

To replace the original complex many-body Hamiltonian with a different auxiliary easily-solved system, Kohn and Sham take the ansatz that assumes that the ground-state density of an interacting system is equal to that of some chosen non-interacting system. Once we incorporate the difficult many-body terms into an exchange-correlation functional of the density, we obtain an independent-particle equation that can be exactly solved numerically. The accuracy of the ground-state density and energy is only limited by the approximations in the exchange-correlation functional. Further, the local density approximation (LDA)

is the most common and simple exchange-correlation functional in practice, in which the effects of exchange and correlation are treated as local properties and E_{xc} is solely dependent on the value of charge density in space.

As suggested by Kohn–Sham, the LDA form exchange-correlation functional is given approximately by the xc-energy of a homogenous electron gas at density $n(\mathbf{r})$.

$$E_{xc}^{LDA} \approx \int d\mathbf{r} n(\mathbf{r}) \epsilon_{xc}(n(\mathbf{r})). \quad (2.6)$$

The exchange-correlation potential is obtained from the functional derivation

$$v_{xc}[n(\mathbf{r})] = \frac{\delta}{\delta n(\mathbf{r})} E_{xc}[n(\mathbf{r})] = \epsilon_{xc}(n(\mathbf{r})) + n(\mathbf{r}) \frac{d\epsilon_{xc}(n)}{dn}(\mathbf{r}). \quad (2.7)$$

For a spin-polarised system, the local spin density approximation (LSDA) is a direct generalisation of LDA by adding the spin degrees of freedom as follows:

$$E_{xc}^{LSDA} \approx \int d\mathbf{r} n(\mathbf{r}) \epsilon_{xc}(n^+(\mathbf{r}), n^-(\mathbf{r})), \quad (2.8)$$

where n^+, n^- represent spin-up and spin-down electron density, respectively.

It is observed that the total energies of homogeneous interacting electron systems with different densities and spin polarisations can be calculated using the quantum Monte Carlo method precisely, and Perdew and Wang [161] have obtained a precise fitting, which is widely used as the standard LSDA version. As L(S)DA does not consider the fluctuation of charge density, it would lead to a sizeable error when the system is very localised.

To reduce the error of L(S)DA, Perdew, Burke, and Ernzerhof (PBE) [160] proposed the generalised gradient approximations (GGA). By including the gradient of charge density, the exchange-correlation is expressed as

$$E_{xc}^{GGA} = \int n(\mathbf{r}) \epsilon_{xc}[n(\mathbf{r})] d\mathbf{r} + \int F_{xc}[n(\mathbf{r}), \nabla n(\mathbf{r})] d\mathbf{r} \quad (2.9)$$

where the functional $F_{xc}[n(\mathbf{r}), \nabla n(\mathbf{r})]$ represents the contribution from the gradient of charge density. With a better treatment of charge density fluctuation, the PBE96 GGA approach provides a more accurate estimation of energy calculation and is the most widely used and cited exchange-correlation approximation in DFT.

2.2 The relativistic effect and FPLO realization of DFT

The last section mainly discusses the non-relativistic Hamiltonian, when the spin degrees of freedom are not coupled to the orbitals. However, in real materials, spin-orbital coupling (SOC) plays an important role in various phenomena, such as magnetocrystalline anisotropy, and anomalous and spin Hall effects, which are discussed later. The SOC would lead to a shift in the energy level, in the same order as the relativistic corrections to the kinetic energy in the non-relativistic Hamiltonian.

The most straightforward way to treat the relativistic effect is to use the full four-component Dirac formalism, which is implemented in the FPLO minimum-basis [102] code. In most DFT codes, the first-order correction term (in c^{-2}) from the Dirac equation is added to the KS equation as a perturbation, known as the SOC term.

2.2.1 Dirac equation and spin-orbit coupling

It is known that the Schrödinger equation is proposed to describe the motion of non-relativistic quantum particles, while the electrons in solids move quickly around the nuclei and have spin degrees of freedom. Thus, an accurate quantum model for electron motion would require the consideration of relativistic effect, as in the famous Dirac equation.

First, we write the Lorentz covariant Dirac equation in matrix form as follows:

$$i\hbar\partial_t\Psi = \left[c\vec{\gamma} \left(\vec{p} - \frac{e}{c}\vec{A} \right) + eA_0 + m_0c^2\beta \right] \Psi \quad (2.10)$$

With the momentum $\vec{p} = -i\hbar\vec{\nabla}$, the vector potential of magnetic field, and the four-by-four γ, β -matrices, we have

$$\gamma_i = \begin{pmatrix} 0 & \sigma_i \\ \sigma_i & 0 \end{pmatrix}, \quad \beta = \begin{pmatrix} \mathbf{1} & 0 \\ 0 & \mathbf{1} \end{pmatrix} \quad (2.11)$$

As electrons moving in solids experience a confining potential, we must add the external $V(\mathbf{r})$ to our free electron Dirac equation for the actual numerical calculation.

$$i\hbar\partial_t\Psi = \left[c\vec{\alpha} \left(\vec{p} - \frac{e}{c}\vec{A} \right) + eA_0 + m_0c^2\beta + \beta V \right] \Psi \quad (2.12)$$

By expanding the Dirac equation and retaining only the first-order term regarding c^{-2} , we obtain the similar non-relativistic Hamiltonian and the relativistic effect as perturbation in spinor space as follows:

$$H_e = H_0 + H_{kinetic} + H_{Darwin} + H_{SO} = \frac{p^2}{2m} + V - \frac{\mathbf{p}^4}{8m^3c^2} + \frac{\hbar}{8m^2c^2}(\nabla^2 V) + \frac{\hbar}{4m^2c^2}(\nabla V \times \mathbf{p}) \cdot \boldsymbol{\sigma} \quad (2.13)$$

Here, the first two terms are non-relativistic H_0 from Coulomb interaction, the third term is the correction to kinetic energy $H_{kinetic}$, the fourth term is the correction to the potential known as the Darwin term H_{Darwin} , and the final term is SOC H_{SO} .

With the SOC term H_{SO} , it is evident that the total energy of the crystal is dependent on the specific direction of the magnetic moments with respect to the crystalline axes. The energy difference from H_{SO} is called magnetocrystalline anisotropy energy, which could determine the direction of magnetic momentum in magnetic materials.

The magnitude of SOC increases with the atomic number in general. This is also the reason why a strong spin Hall effect is typically observed for a heavy 5d metal. In Chapter 4, we show that H_{SO} is crucial to various transport phenomena, especially in magnetic materials, not only because of its magnitude but also because it breaks the corresponding spin rotation symmetries.

2.2.2 FPLO formalism

Despite the above discussed theories and approximations, the solution of the density functional equation also relies on the exact wavefunction basis. In the solid-state system, there are two widely used bases: 1. plane wave (PW) and its extensions augmented plane wave (APW) and linearised augmented plane wave (LAPW); 2. localised orbital. As most of our work is carried out from the DFT calculation of FPLO, we review the local orbital method and FPLO formalism.

The linear combination of atomic orbital (LCAO) method uses a basis of atomic or modified atomic-like functions, which provide an intuitive description of electronic states in solids. Bloch first considered the simplest s-symmetry function, and Slater and Koster [189] subsequently summarised and provided a framework for the LCAO method within tight-binding approximation.

FPLO minimum basis code is used to solve the KS equation for a periodic lattice and finite system (such as molecule and slab). With a much smaller basis set, FPLO achieves a level of numerical accuracy comparable to advanced full-potential LAPW implementations such as Wein2k. [112] Inside the programme, the KS wavefunction $\psi_{\mathbf{k}}$ is expressed as a set of atomic-like local basis orbitals $|\mathbf{s}\mu\rangle = \varphi_{\mathbf{s}\mu}(\mathbf{r} - \mathbf{R} - \mathbf{s})$ located at the site \mathbf{R} (lattice vector)

+ \mathbf{s} (atom position in a unit cell) and classified by orbital labels μ , which are atom-like quantum numbers and spin ($\mu = nlm$).

$$\psi_{\mathbf{k}} = \sum_{i\mu} |i\mu\rangle c_{i\mu}^{\mathbf{k}} \quad (2.14)$$

with the coefficients $c_{i\mu}^{\mathbf{k}}$.

Replacing the KS-orbital by atomic basis, the KS-equation 2.5 become:

$$\left\{ -\frac{1}{2}\nabla^2 + [v(\mathbf{r}) + \int \frac{n(\mathbf{r}')}{|\mathbf{r} - \mathbf{r}'|} d\mathbf{r}' + v_{xc}(n(\mathbf{r}))] \right\} |i\mu\rangle = e_{i\mu} |i\mu\rangle \quad (2.15)$$

With the new basis orbitals, we could construct the density and perform self-consistent calculation.

2.3 Wannier functions from FPLO

The linear response and the nonlinear response calculation rely on the integral of a dense momentum space mesh, and generation and diagonalisation process of Hamiltonian for each k -point is expensive with a large number of basis functions. However, the DFT Hamiltonian is usually huge, especially that from the PW basis approach. To construct a reduced Hamiltonian, we use the Wannier interpolation to project only the states around the Fermi level.

Gregory Wannier first introduced Wannier functions as a complete set of orthogonal functions of solid-state systems. [221] Wannier functions can be chosen in various ways, and the most widely and conveniently used way to fix the gauge freedom is the maximally-localised Wannier functions. [131]

However, the maximally-localised procedure implemented in Wannier90 would generally break the symmetry of Wannier functions transformed from the first-principle Bloch wavefunction. Further, the symmetry breaking of the Wannier function would lead to additional error in the response calculation. In FPLO, we use a minimum local orbital basis, which is already a set of highly localised Wannier functions by definition. A good choice of projected Wannier functions, which are less entangled with orbitals out of the selected energy window, would automatically provide localised Wannier functions.

In general, the Wannier functions are generated from the Bloch representation by a set

of transformations in a continuous space of unitary operator, denoted by

$$W_{Ra} = \int e^{-ikR} \sum_n \Psi_n(k) U_{na}(k) \quad (2.16)$$

Here, the Wannier function W_{Ra} is in the cell R and is of type a (which denotes the Wannier centre and orbital label), $\Psi_n(k)$ denotes the Kohn–Sham (KS) Bloch functions, and U is a column unitary projector ($U^\dagger U = 1$, $UU^\dagger = P$), which maps all the KS bands on fewer WFs, and contains a free choice gauge.

In FPLO, KS Bloch wavefunctions are constructed from a localised molecular orbital basis Φ defined as

$$\Psi_n(k) = \frac{1}{\sqrt{N}} \sum_{Rsv} \Phi_{Rsv} e^{ik(R+s)} C_{sv,n}(k) \quad (2.17)$$

where s is the atom position, ν represents quantum numbers regarding the orbital label, and $C_{sv,n}(k)$ is the coefficient.

2.3.1 Wannier transformation in FPLO

After the convergence of DFT self-consistent calculation, we define a test function or WF projector χ and an energy window for each WF and start the Wannier procedure. The WF projector χ is a linear combination of FPLO orbitals used in the DFT step, and the energy window specified the dispersion of the KS band with weight dominated by the selected Wannier orbitals.

The numerical transformation is separated into two steps. First, FPLO generates the column unitary projection operator U from the input Wannier function projector χ and the corresponding energy window. Applying the projection operator U to the KS wavefunction, we obtain the expression of real space Wannier function as the sum of Bloch functions

$$\begin{aligned} W_\mu(r, k) &= \sum_n \Psi_n^k(r) U_{n\mu}^k \\ &= \frac{1}{\sqrt{N}} \sum_R e^{ikR} W_{R\mu}(r) \end{aligned} \quad (2.18)$$

$$W_{R\mu}(r) = \int e^{-ikR} W_\mu(r, k) dk \quad (2.19)$$

As already shown, the orbital basis Bloch functions are

$$\Phi_{s\mu}(k) = \frac{1}{\sqrt{N}} \sum_R \Phi_{Rs\mu} e^{ik(R+s)}$$

Thus, the representation of the Hamiltonian in the Bloch function of DFT basis orbital is

$$\underline{H}_{s's}(k) = \langle \Phi_{s'}^k \hat{H} \Phi_s^k \rangle \quad (2.20)$$

$$= \frac{1}{N} \sum_{R'R} \langle \Phi \hat{H} \Phi \rangle_{R's'R_s} e^{ik(R+s-R'-s')} \quad (2.21)$$

$$= \sum_R \langle \Phi \hat{H} \Phi \rangle_{0s',Rs} e^{ik(R+s-s')} \quad (2.22)$$

The momentum space Hamiltonian in the Wannier basis is written as

$$\begin{aligned} \langle W_{\mu'}^k \hat{H} W_{\mu}^k \rangle &= \sum_n U_{n\mu'}^{k*} \varepsilon_n(k) U_{n\mu}^k \\ &= \frac{1}{N} \sum_{RR_1} \langle W_{R_1\mu'} \hat{H} W_{R\mu} \rangle e^{ik(R-R_1)} \\ &= \sum_R \langle W_{0\mu'} \hat{H} W_{R\mu} \rangle e^{ikR} \delta_{qk} \end{aligned} \quad (2.23)$$

with a real space hopping parameter from μ' orbital in the first unit cell to orbital μ in cell R

$$\begin{aligned} \varepsilon_{0\mu',R\mu} &= \langle W_{0\mu'} \hat{H} W_{R\mu} \rangle \\ &= \int e^{-ikR} \langle W_{\mu'}^k \hat{H} W_{\mu}^k \rangle dk \end{aligned} \quad (2.24)$$

Further, $\varepsilon_n(k) = (C^{k+} \underline{H}^k C^k)_n$ is the eigenvalue of the DFT band n .

So far, we have obtained the momentum space Wannier Hamiltonian. If the projection operator U is a unitary matrix, i.e. the selected projected Wannier functions have the same Hilbert space as the DFT basis orbitals, the band structure from the Wannier model would be identical to the DFT band structure.

The second step is the numerical generation of real space hopping parameters, as this is the output of FPLO, which can be used to generate the Wannier model. To obtain a small set of hopping parameters, we could introduce a cut-off both for the hopping distance R and the magnitude of hoppings. The resulting hopping parameter can be

Fourier-transformed to the momentum space Hamiltonian, and the diagonalisation of such a Hamiltonian would provide us the band structure and the corresponding wavefunction, which is used for subsequent transport calculations. The removal of hoppings by distance and magnitude provides us a slightly different Wannier model as shown in Eq. 2.23, although the symmetry is identical. One must check the band structure of the modified small Wannier model with the DFT band structure and ensure that the difference is in an acceptable range.

Notably, the Wannier module in FPLO enables the automatic generation of the tight-binding model for numerous materials. In programmes such as Wannier90, as the disentanglement and maximally-localised procedure are tricky, one must make many attempts to determine the correct Wannier projector and the corresponding energy window, which makes it impossible to perform the Wannier model generation automatically.

In FPLO, as we start from a minimum basis of local orbitals, the Hilbert space is much reduced compared with the PW approach. By including all the valence electrons (the whole DFT basis functions except semi core electrons) in the Wannier projector χ , the upper energy window is chosen from the highest band, and counting from the highest band by the number of input Wannier projectors, the lowest selected bands and the down energy window are fixed, which normally has a clear band gap to the semi-core state. The generated Wannier model perfectly reproduces the DFT band structure in most of the cases. Considering Sn as an example, we only need to include $5s, 5p, 6s, 5d, 6p$ in the input projector, which are 26 orbitals even in the SOC case. Thus, the automatic procedure would provide us a Wannier model with approximately $20N - 30N$ (N is the number of atoms in the unit cell). The automatic Wannier model generation and highly efficient response programme enable the high-throughput calculation of transport property in numerous materials.

3 Weyl semimetal phase and linear response Hall current

3.1 Introduction

The study of quantum spin Hall effect leads to the discovery of time-reversal invariant TIs, and has largely promoted our understanding of band theory in terms of topology [72, 164]. In the study of band insulators, the topological properties are characterised by the presence of an energy gap in the boundary, and topological nontrivial connections to gapless states have begun to emerge. In a 3D TI, there is a gapless Dirac dispersion at the surface, analogous to the two-dimensional semimetal graphene. In the presence of both time reversal and inversion symmetries, the transition between topological and trivial phases would go through a gapless state— for example, a 3D Dirac dispersion would appear in the 3D topological to trivial insulator transition. In general, the four-fold Dirac degeneracy not topologically protected and the residual momentum-conserving terms in the Hamiltonian could mix these states and gap out the electronic spectrum. However, in some special cases, the mixing of states could be forbidden by space group symmetries and the Dirac nodes may remain gapless, and the materials that hold these kinds of degeneracy nodes are called Dirac semimetals (DSMs). If inversion symmetry or TRS is broken, the critical point expands into a gapless phase with double degenerate Weyl nodes, which hold integer topological charge of Chern flux, also viewed as the ‘magnetic monopole’ in momentum space. As the Weyl point is topologically protected and not connected to space group symmetries, the existence of WSM phase in materials is stable under small perturbations.

In this chapter, we introduce the time-reversal-breaking WSM in Ti_2MnAl and its large anomalous Hall effect owing to the enhanced Berry curvature around Weyl points.

3.1.1 Weyl fermion from massless Dirac equation

Shortly after Paul Dirac proposed his four-fold Dirac equation Eq. 2.10, Hermann Weyl observed that it could be simplified if we have massless particles $m = 0$ as follows:

$$\gamma^\mu \partial_\mu \psi = I_2 \frac{1}{c} \frac{\partial \psi}{\partial t} \pm (\sigma_x \frac{\partial \psi}{\partial x} + \sigma_y \frac{\partial \psi}{\partial y} + \sigma_z \frac{\partial \psi}{\partial z}) = 0 \quad (3.1)$$

Here, I_2 is a two-by-two identity matrix, and $\sigma_{x,y,z}$ are three Pauli matrices. Thus, we obtain the famous Weyl Hamiltonian $H_W = \mp(c\hat{p} \cdot \vec{\sigma})$, and ψ represents the two-component Weyl spinors, which have fixed chirality.

Since Weyl proposed the massless chiral Fermion, it has been considered as the building block for quantum field theory and the standard model. So far, Weyl fermion has not been observed as a fundamental particle in nature. However, it has recently been observed that it could be realised as an emergent quasi-particle in a low-energy condensed matter system.

3.1.2 Weyl semimetal and unique surface state

In a TI, the valence and conduction bands with opposite parity [8,56] cross each other and open an energy gap owing to SOC. When TRS or inversion symmetry is broken, some of the anti-crossing points may become gapless as a semimetal [148] and exhibit linear energy dispersions along all three-dimensional (3D) momenta (k) starting from the crossing point called the Weyl point, which result in topologically nontrivial semimetals: WSMs.

The Weyl point is the monopole of Berry curvature (Chern flux) and carries an integer charge known as the Chern number. They always come in pairs in the BZ, with opposite Chern numbers and therefore corresponding left- or right-hand chirality. As the two-dimensional (2D) k plane between a pair of Weyl points has a nonzero Chern number, robust edge states on the boundary are induced similar as the 2D quantum anomalous insulator. However, topological edge states disappear in other 2D k planes because of vanishing Berry curvature flux. Therefore, these edge states in a WSM [215] would form unclosed Fermi lines in the 3D surface of BZ, called Fermi arcs, existing to connect the surface projection of two Weyl points with opposite parity [Fig. 3.1(b)]. [?]

As the Fermi surface of a TI or other trivial materials is a closed curve, the unclosed Fermi arc in a WSM serves as a strong evidence of WSM. In addition, WSM is robust against any weak perturbation that preserves translational symmetry. For example, an exchange field or slight lattice distortion can only shift the positions of Weyl points.

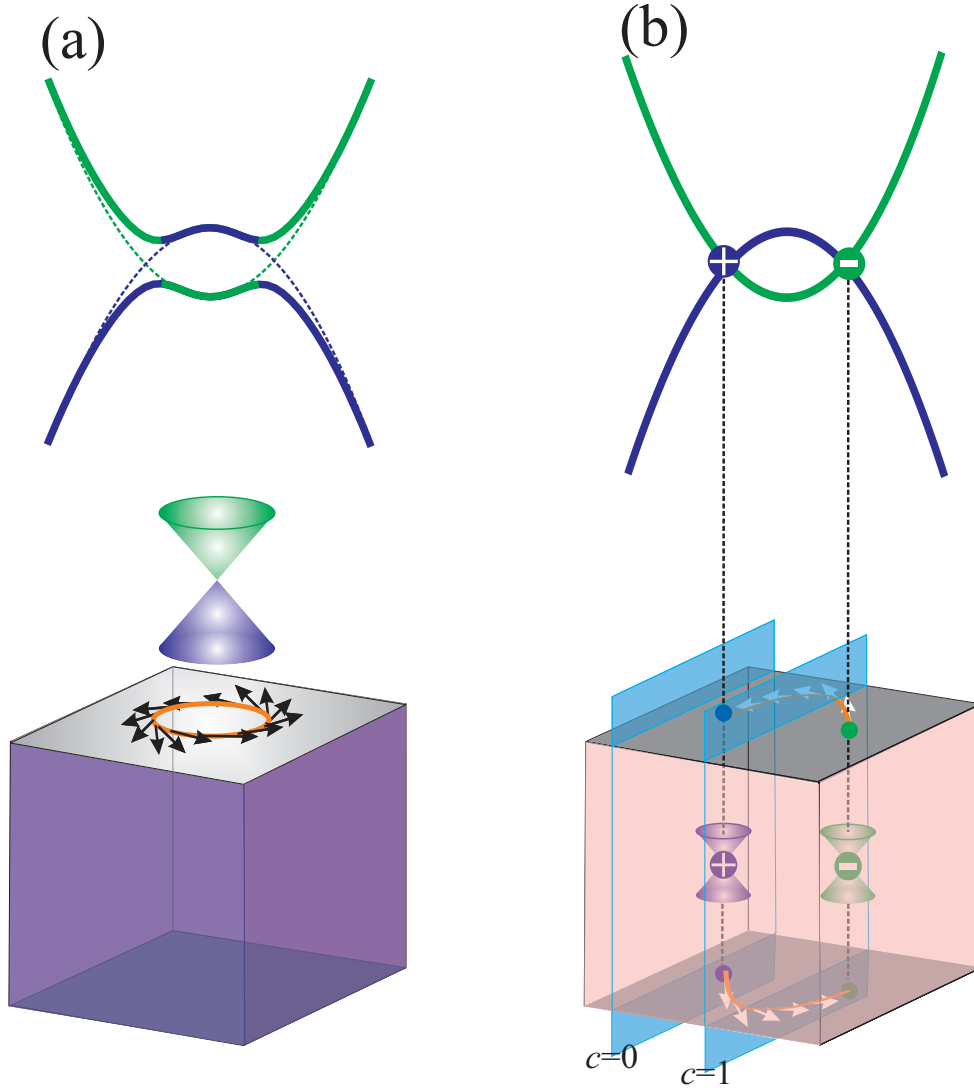


Figure 3.1: Schematics of the topological insulator and Weyl semimetal. (a) A TI exhibits an energy gap with a band inversion. Topological surface states exhibit Dirac-cone-type dispersion with spin texture. (b) A WSM is gapless in the bulk and a pair of Weyl points (band crossing points) exists with opposite parity. Nonzero Chern number (c) only exists between Weyl points of the opposite chirality, which leads to a spin-resolved surface Fermi arc.

Besides the topological surface Fermi arcs, WSMs also exhibit exotic topological transport phenomena, such as the chiral anomaly effect [79, 149, 219, 262], gravitational anomaly effect [65], strong intrinsic anomalous and spin Hall effects [17, 199, 237], large magnetoresistance [59, 79, 123, 136, 183, 219, 262], and even special catalytic activity [168].

3.2 Magnetic weyl semimetal in Ti_2MnAl

The existence of Weyl points requires the breaking of spin degeneracy, either by breaking inversion or time reversal symmetry (or both) [147]. Since the Berry curvature is odd under time reversal, Weyl points in the latter case can generate a strong anomalous Hall effect (AHE). Although the total magnetic moment vanishes, time-reversal symmetry is broken in compensated ferrimagnets. In contrast to antiferromagnets, bands in compensated ferrimagnets are spin split, which allows the existence of Weyl points even without spin-orbit coupling (SOC). Additionally, the Weyl points in compensated ferrimagnets lead to a strong AHE despite a zero net magnetic moment. Different from the non-collinear antiferromagnets Mn_3X ($X = \text{Ge}, \text{Sn}, \text{Ga}, \text{Ir}, \text{Rh}, \text{and Pt}$) [27, 143, 144, 267], the AHE in a compensated magnetic WSMs is topologically protected. If the Weyl nodes are close to the Fermi level and are isolated from trivial bands, the charge carrier density is expected to be very low and a large anomalous Hall angle is naturally expected in these materials.

We have theoretically studied an ideal time-reversal symmetry breaking WSM in the inverse Heusler compound Ti_2MnAl with compensated magnetic structure, where the Weyl points are only 14 meV away from the Fermi energy. In Ti_2MnAl the Weyl points do not derive from mirror symmetry protected nodal lines, due to the lack of mirror planes in the inverse Heusler structure. Rather, the Weyl points exist without taking into account SOC, in contrast to the recently predicted Weyl-points in ferromagnetic Co-based magnetic Heusler compounds, which possess nodal lines close to the Fermi level. [25, 109, 220]. Since the nodal lines normally disperse in energy, the Co-based magnetic Heusler WSMs have higher bulk charge carrier density, which makes the detection of Weyl points related phenomena difficult. Due to the lower symmetry, Ti_2MnAl has a small charge carrier density of only $2 \times 10^{19}/\text{cm}^3$, which is even smaller than the charge carrier density in NbP [101]. Therefore the Weyl points in Ti_2MnAl should be much easier to observe experimentally and a large anomalous Hall angle (AHA) is expected. Heusler compounds are ideal materials for the study of the interplay between magnetism and topology [20, 52] due to their excellent tunability. According to our calculations, Ti_2MnGa and Ti_2MnIn have a similar electronic structure with Weyl points. However, only Ti_2MnAl has been

successfully grown in thin films with a high Curie temperature above 650 K. [51, 53] Considering all these factors, Ti_2MnAl provides an excellent platform for the study of magnetic Weyl physics and suggests a new direction to obtain a strong AHE without a net magnetic moment.

Methods. To investigate the electronic band structure we have performed *ab-initio* calculations based on density functional theory (DFT) using the full-potential local-orbital code (FPLO) [102] with a localized atomic basis and full potential treatment. The exchange and correlation energy is considered at the generalized gradient approximation (GGA) level [160]. The tight binding model Hamiltonian was constructed by projecting the Bloch states onto atomic orbital like Wannier functions. By using the tight binding model Hamiltonian, we have calculated the surface state.

3.2.1 Weyl point and Fermi arc

Ti_2MnAl has an inverse Heusler lattice structure with space group $F\bar{4}3M$ (No.216) [Fig. 3.2(a)] [53, 188], which, without the inclusion of spin-orbit coupling (SOC), shows a typical half-metallic electronic band structure, as shown in Fig. 3.2(c, d). Because of the compensated magnetic sublattices formed by Ti and Mn, the net magnetic moment in Ti_2MnAl vanishes. The spin-down channel forms an insulating gap of 0.5 eV, and the spin-up channel is semimetallic. The spin-up bands in Fig. 3.2(c) show an easily identifiable band anti-crossing along the $L - W$ direction, indicating a band inversion around the Fermi energy. Though there is a general gap for the spin-up channel along the high symmetry directions, its density of states is not zero at the Fermi level. Therefore, the spin-up bands should cut the Fermi level in some lower symmetry directions.

Indeed, there is a linear crossing point away from the high-symmetry lines [Table 4.2]. Due to the six mirror planes $M_{\pm 110}$, $M_{1\pm 10}$, and $M_{0\pm 11}$, together with the three rotation axes $C_{2,x}$, $C_{2,y}$, and $C_{2,z}$, there are 12 pairs of linear crossing points in total. This is completely different from the Co-based Heusler WSMs, where the band structures possess nodal lines without considering SOC. Calculating the Berry phases of these 12 pairs of linear crossing points, we found that half of them have Chern number +1 and the other half Chern number -1. Hence the chirality obeys the mirror symmetries, as presented in Fig. 3.2(b). The energy dispersion of one pair of Weyl points related by the mirror symmetry is given in Fig. 3.3(a) and (c), from which we can see that the Weyl points are just lying at the Fermi level.

In order to completely understand the Weyl points in Ti_2MnAl , we need to take SOC

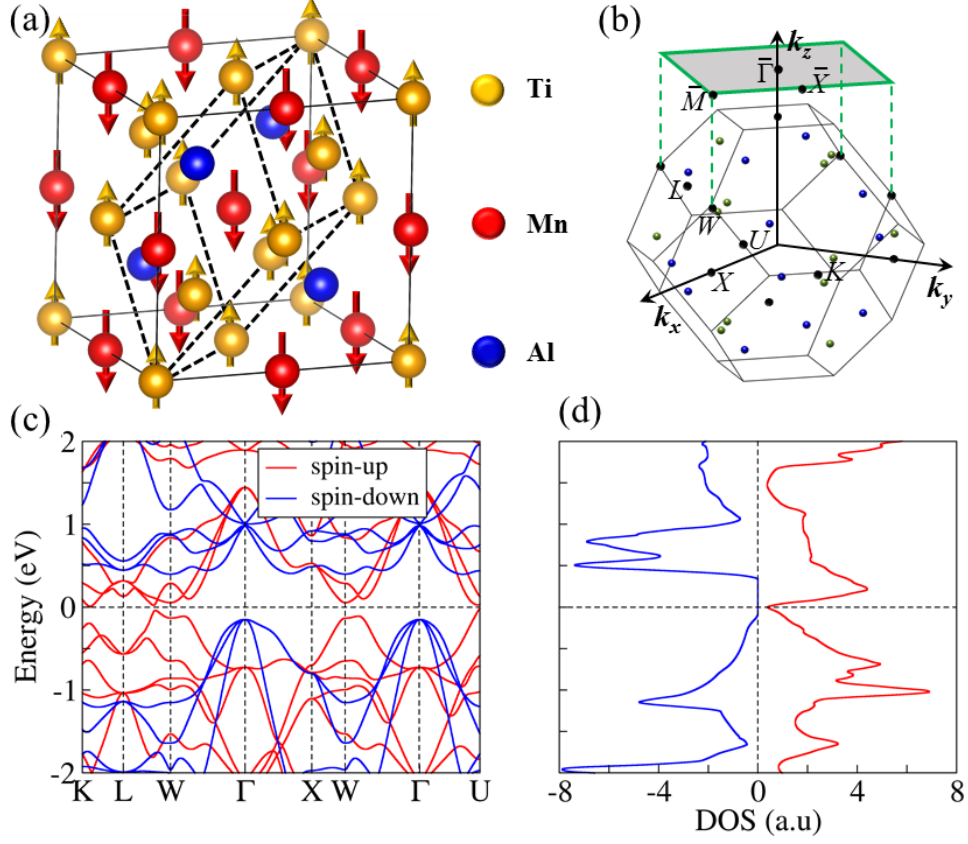


Figure 3.2: (a) FCC lattice crystal structure of Ti_2MnAl . Spin polarization of atom Mn and Ti are along positive and negative z direction, respectively. The primitive cell is marked by the dashed line. (b) Three-dimensional Brillouin zone (BZ) and its two-dimensional projection in (001) direction. Weyl points with positive and negative chirality are presented by the green and blue spheres. (c, d) Energy dispersion and density of states without the inclusion of SOC. The labels of high symmetry points are given in (b).

into consideration, though SOC is not very strong in this compound, due to the light elements involved. In the presence of SOC, the symmetry of the system is reduced and the details of band structures are dependent on the direction of the magnetization. To obtain the magnetic ground state, the total energies of magnetizations along the (001), (110), and (111) directions were compared. The net magnetic moments are still smaller than $1 m\mu_B$ per formula unit and the total energy difference between them is smaller than 0.1 meV, which is beyond the accuracy of DFT itself. Taking the magnetic polarization along (001) as an example, we analyzed the band structures further. Since SOC is not so strong in this compound, it just acts as a weak perturbation. The original position of one pair of Weyl points W_A and W_B and the energy dispersion slightly breaks the reflection

Table 3.1: Location of one pair of Weyl points (labeled as W_A and W_B). Without the inclusion of SOC, they are related to each other by the mirror plane, and all the other Weyl points can be obtained via the symmetries of $M_{\pm 110}$, $M_{1\pm 10}$, $M_{0\pm 11}$, $C_{2,x}$, $C_{2,y}$, and $C_{2,z}$. SOC breaks the mirror symmetry as a perturbation. The positions of Weyl points are described in the Cartesian coordinates in units of $(\frac{2\pi}{a}, \frac{2\pi}{a}, \frac{2\pi}{a})$

	w/o SOC	SOC
W_A	(0, 0.4737, 0.7515)	(0, 0.4802, 0.7531)
W_B	(0.4737, 0, 0.7515)	(0.4680, 0, 0.7504)

symmetry $M_{\pm 110}$. A comparison of the energy dispersions of one pair of Weyl points before and after the inclusion of SOC is shown in Fig. 3.3(a-d). Without the inclusion of SOC, the energy dispersion is mirror symmetric, as shown by the red dashed line in Fig. 3.3(a). As long as SOC is taken into consideration, the mirror symmetry is not preserved. The bands corresponding to W_A cross the reference line (the red dashed line) two times, while the bands associated with W_B cross it 4 times. Because of the perturbation from SOC, the Weyl points are not at the charge neutrality point anymore, which shifts them above the Fermi level by around 14 meV, see Fig. 3.3(d). Though the SOC slightly shifts the Weyl points in both momentum and energy, the chirality remains unchanged, as shown in Fig. 3.3(e-f).

A typical feature of WSMs is the topological surface Fermi arc state. To calculate the (001) surface state, we considered an open boundary condition with the half-infinite surface by using iterative Greens function method [178, 179]. From the energy dispersion along the high-symmetry line $\bar{X} - \bar{\Gamma} - \bar{M}$, surface bands connecting the bulk conduction and valence states can be seen, which should be related to the Fermi arcs. Actually, the two projected Weyl points on the (001) surface are very close to the $\bar{\Gamma} - \bar{M}$ line (see Fig. 3.4(c, d)), and therefore nearly linear bulk band crossings can be observed along $\bar{\Gamma} - \bar{M}$. Since Fermi arcs begin and end at the Weyl points with opposite chiralities, we have chosen a special direction along the two projected Weyl points (see Fig. 3.4(c)). For the (001) surface, two Weyl points of the same chirality project onto each other. The corresponding energy dispersion, given in Fig. 3.4(b), clearly shows the linear dispersion of the bulk Weyl points (labeled by the green and blue circles) with two Fermi arc related surface bands terminating at the two Weyl points on top of each other. Because of the dispersion of the Fermi arcs below the Fermi level, they could be detected by ARPES and STM measurements.

By fixing the energy at the Weyl points, perfect Fermi arcs with tiny bulk states can

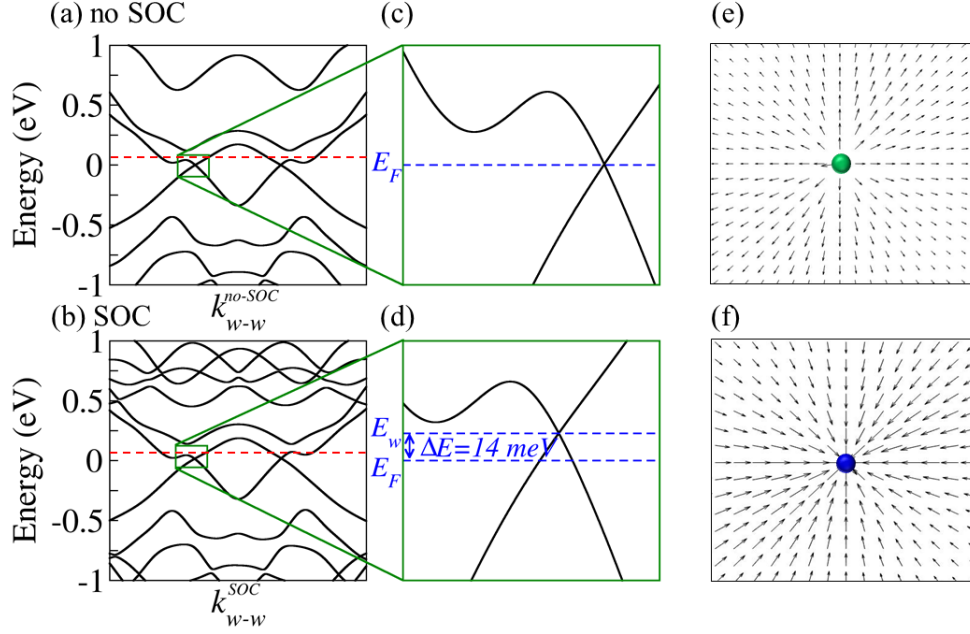


Figure 3.3: (a-d) Energy dispersion of one pair of Weyl points for (a, c) without and (b, d) with the inclusion of SOC. The red dashed lines in (a, b) are the reference lines indicating the breaking of the mirror symmetries if SOC is considered. (e, f) Berry curvature distribution around the Weyl points with positive and negative chirality.

clearly be seen in Fig. 3.4(c). Dependent on the number of surfaces projected Weyl points, the number of Fermi arcs terminated at each Weyl points differs. Moreover, two long Fermi arcs extend around 75% of the reciprocal lattice vector, which is amongst the longest Fermi arc to be observed so far. On shifting the energy down by 14 meV to the charge neutral point, there is a slight change in the surface state and most of the Fermi arcs remain clearly detectable. Therefore, the Weyl semimetal states in Ti_2MnAl lead to the existence of isolated surface Fermi arcs, and the long Fermi arc around the charge neutral point should be easy to detect by surface techniques.

3.3 Anomalous Hall effect from magnetic Weyl Fermion

Owing to the large Berry curvature around the Weyl points, a strong AHE is expected in magnetic Weyl semimetals. To investigate the AHE we have computed the intrinsic AHC by the linear-response Kubo formula approach in the clean limit as Eqs (1.11) [234]. A $500 \times 500 \times 500$ k -grid in the BZ was used for the integral of the AHC.

If the magnetization is along the z -axis, σ_{xy}^z is the only non-zero component of the

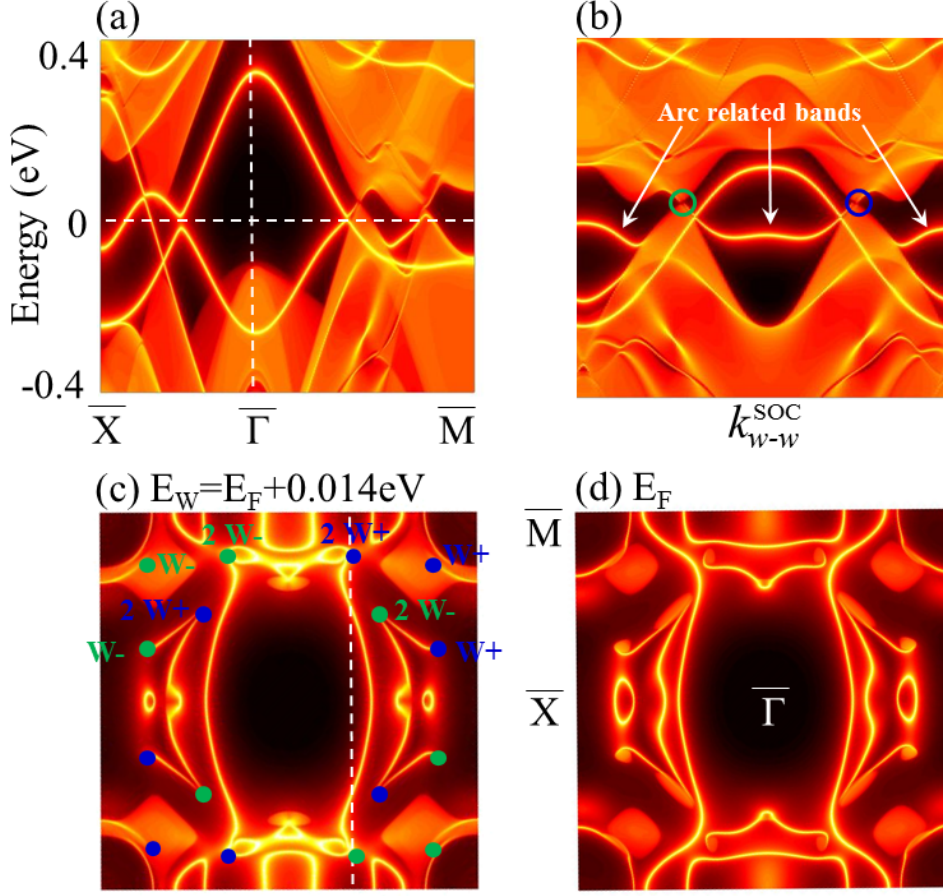


Figure 3.4: Surface states of Ti₂MnAl terminated along the (001) direction. (a) Surface energy dispersion along high symmetry lines of $\bar{X} - \bar{\Gamma} - \bar{M}$. (b) Surface energy dispersion crossing one pair of Weyl points. The k -path is given in (c). (c,d) Fermi surface with energy lying at Weyl points and charge neutral point, respectively.

AHC-tensor. From our calculation, the intrinsic AHC is around 300 S/cm at the charge neutrality point. However, since the Weyl points are just above the Fermi level, the AHC should be sensitive to the position of chemical potential and a large value is expected at the energy of the Weyl points. To investigate the effect of electron and hole doping, we calculated the energy dependent AHC, see Fig. 3.5(a). The AHC increases sharply when shifting the energy from E_F to E_w , and the AHC attains a peak value at $E = E_w$ with $\sigma_{xy}^z = 550 \text{ S/cm}$, implying that the large AHC originated from the Weyl points, since the Berry curvature distribution of a Weyl point peaks sharply at the nodal energy. For further confirmation of the effect of the Weyl points to the AHC, we analyzed the Berry curvature distribution in k -space. Fig. 3.5(b) shows the Berry curvature distribution in the $k_z=0$

plane with four pairs of Weyl points very close to it. Except for the eight hotspots derived from the Weyl points, there are barely other contributions to the AHC. The other two high-symmetry planes $k_x=0$ and $k_y=0$ have almost the same Berry curvature distribution. Therefore, the AHE in Ti_2MnAl is mainly generated by the 12 pairs of Weyl points, and hence it is topologically protected.

The AHA, defined as $\sigma_{xy}^z/\sigma_{xx}$, provides a dimensionless measure of the strength of the AHE, which is the conversion efficiency from the longitudinal charge current to transverse charge current. The longitudinal conductivity σ_{xx} is proportional to the charge carrier density and mobility. In comparison to metals, the charge carrier density of semimetals differs by some orders of magnitude and therefore the conductivity σ_{xx} is lower as well. Theoretically, the AHA can be estimated from the intrinsic AHC and charge carrier density. To evaluate the charge carrier density we have analyzed the FSs in three dimensions. As shown in Fig. 3.5(c,d), there are 24 electron bubbles and 8 hole bubbles in the 1st BZ, and all of them are very small. The charge carrier density obtained from the volume of the FSs is around $2 \times 10^{19}/\text{cm}^3$, a typical semimetallic value. Though we cannot compute an accurate σ_{xx} , which needs further experimental transport measurements, a large AHA is expected from the small charge carrier density and a relatively large AHC. In the quantum anomalous Hall effect (QAHE), the AHA diverges, since the 2D bulk becomes insulating. A magnetic material with a large bulk AHA could show a QAHE in thin films due to quantum confinement [237], and therefore the study of the thin film of Ti_2MnAl should be highly interesting.

3.4 Summary

In summary, we have theoretically predicted the magnetic WSM and large AHC in the inverse Heusler compound Ti_2MnAl with Weyl points only 14 meV away from the Fermi level. Because of the large Berry curvature from Weyl points and compensated magnetic structure, the strong AHE exists even without a net magnetic moment. Motivated by this finding, it would be interesting to investigate the topological properties of the other class of compensated ferrimagnets in the Heusler structure with 24 valence electrons [195]. Due to the large separation of Weyl points with the opposite chirality, the Fermi arc extend up to 75% of the reciprocal lattice vectors in length. Our work provides an excellent magnetic Weyl semimetal for both transport and surface study.

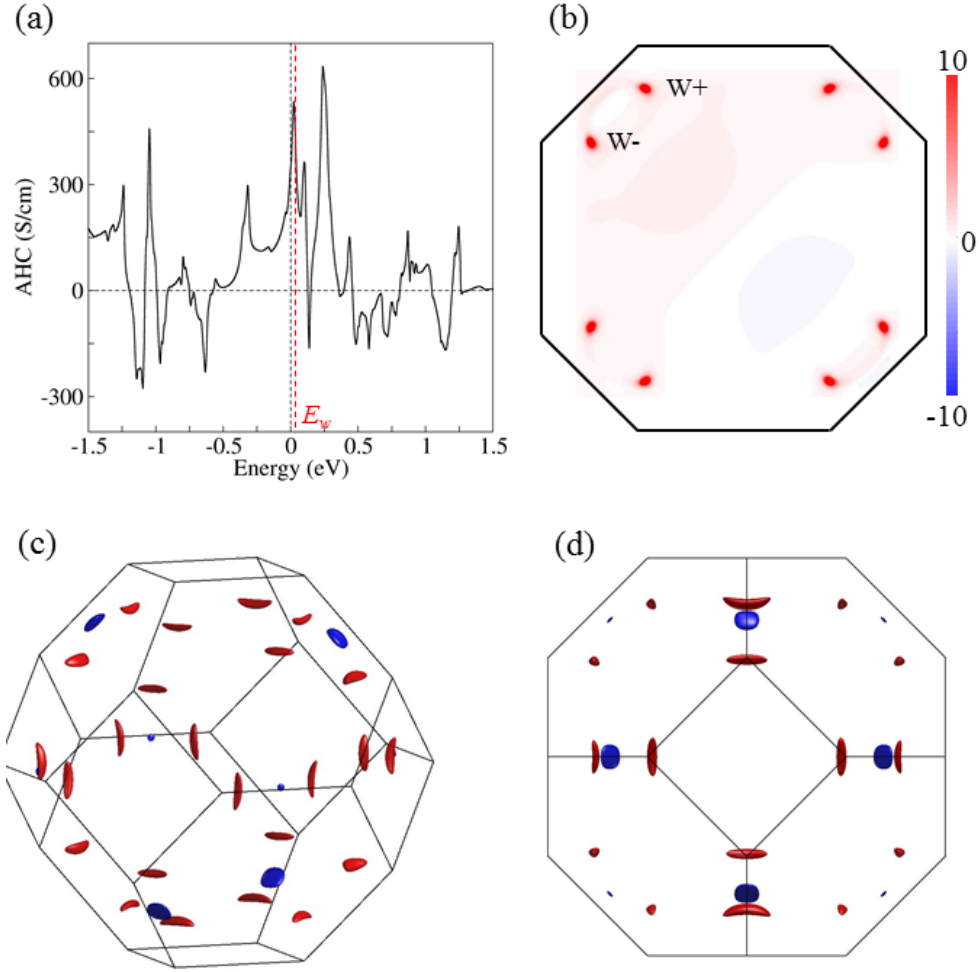


Figure 3.5: (a) Energy-dependent AHC. The peak value highlighted by red dashed line corresponds to the Weyl-node energy. (b) Berry curvature distribution in the $k_z=0$ plane. The eight hot spots are just the positions of Weyl points. Color bars are arbitrary units. (c, d) FSs distribution in the 3D BZ. Red and blue FSs are hole and electron bubbles, respectively.

4 Linear response of spin current: spin Hall and Nernst effect

In previous chapter, we introduce the magnetic Weyl semimetal and the linear response theory to calculate intrinsic anomalous Hall effect. In Eq. (1.11), (1.10), if we set \hat{A} to the spin-current operator, $\hat{j}_{i,j}^s = \frac{1}{2}\{\hat{s}_i, \hat{v}_j\}$, they describe time reversal even and odd spin-conductivity. In this chapter, we would first study the spin Hall effect in time reversal symmetric Dirac nodal line semimetal and Weyl semimetal, analysis the relation between different type of topological band structures with spin Berry curvature in k space. Then we show the giant spin Hall and Nernst effect in a p-band semimetal InBi as a successful example of such guiding rules, and the unconventional relationship between spin Nernst conductivity and Hall conductivity is well studied both from material specific tight-binding model and modified TI model.

4.1 Dirac nodal line induced spin Hall effect

We have found Dirac nodal lines (DNLs) in the band structures of metallic rutile oxides IrO_2 , OsO_2 , and RuO_2 and revealed a large spin Hall conductivity contributed by these nodal lines, which explains a strong spin Hall effect of IrO_2 discovered recently. Two types of DNLs exist. The first type forms DNL networks that extend in the whole Brillouin zone and appears only in the absence of spin-orbit coupling (SOC), which induces surface states on the boundary. Because of SOC-induced band anti-crossing, a large intrinsic SHE can be realized in these compounds. The second type appears at the Brillouin zone edges and is stable against SOC because of the protection of nonsymmorphic symmetry. Besides reporting new DNL materials, our work reveals the general relationship between DNLs and the SHE, indicating a way to apply Dirac nodal materials for spintronics.

4.1.1 Nodal line semimetal

Dirac and Weyl semimetals are typical three-dimensional topological nodal point semimetals, where nodal points and surface Fermi arcs have been recently discovered in real materials [242], for example, Na_3Bi [121, 218, 238], TaAs [78, 125, 222, 239, 246], and MoTe_2 [39, 77, 85, 192, 198, 204]. Beyond Dirac and Weyl points, new-type symmetry-protected nodal points with three-, six- and eight-band crossings in nonsymmorphic space groups [11, 226] and nodal points with triple degeneracy in symmorphic space groups [223, 224, 229, 269] have been proposed with potential material candidates, such as MoP [124, 269]. Furthermore, nodal lines [18, 32, 33, 48, 260, and references therein] can exist in two classes of systems, according to the absence and presence of spin-orbit coupling (SOC) [48, 50]. The first type without SOC has been reported in many systems (e.g., LaN) [23, 28, 73, 97, 113, 225, 236, 255, 260]. The inclusion of SOC will either gap or split the nodal lines [222, 260]. The second type requires the protection of additional symmetries such as nonsymmorphic symmetries [19, 48, 180, 251] and mirror reflection [1, 10, 32, 225]. Nodal lines can cross the whole Brillouin zone (BZ) in a line shape, form closed rings inside the BZ, or form a chain containing connected rings [19]. The topological nature of a nodal line can be characterized by a quantized Berry phase π along a Wilson loop enclosing the nodal line [18, 23, 49, 193, 254]. On the surface, nodal line materials were predicted to host drumhead-like surface states [225]. Theoretical search for exotic nodal phases and corresponding materials launches a race for discovering novel topological states in experiments.

Since topological nodal semimetals or metals commonly exhibit nontrivial Berry phases and strong SOC, they are expected to reveal a strong SHE as an intrinsic effect from the band structure [199]. The intrinsic SHE, in which the charge current generates the transverse spin current, is intimately related with the Berry phase and SOC [186]. Four of us recently found that the first type of Dirac nodal lines (DNLs) (without SOC) can induce a strong intrinsic SHE when turning on SOC, for example, in the TaAs -family Weyl semimetals [199]. Furthermore, it provokes us to search for topological nodal systems among known SHE (or AHE) materials. Therefore, our attention has been drawn to SHE material IrO_2 discovered recently [58], where its thin films act as efficient spin detectors [58, 167] via the inverse SHE that converts the spin current to the electric voltage. However, the microscopic understanding of the SHE is still missing for this metallic oxide. Furthermore, the strong SOC of the $\text{Ir-}5d$ orbitals and nonsymmorphic symmetries of its rutile crystal structure imply that IrO_2 may host topological nodes in the band structure. Additionally, this oxide has been used for electrodes in various applications such as catalysts in water

splitting [210, and references therein] and ferroelectric memories for a long time [181].

We theoretically investigated the topology of the band structure of metallic rutile oxide IrO_2 and similar oxides RuO_2 and OsO_2 . We observe two types of DNLs in their band structures. The first type extends the whole BZ and forms a square-like DNL network in the absence of SOC, resulting in surface states. Joint points of the network are six- and eight-band-crossing points at the center and boundary of the BZ, respectively. These DNLs become gapped and lead to a strong SHE when SOC exists. The second type is stable against SOC and appears at the edges of the tetragonal BZ, which is protected by nonsymmorphic symmetries.

Calculation method To investigate the band structure and the intrinsic SHE, we have performed *ab initio* calculations based on the density-functional theory (DFT) with the localized atomic orbital basis and the full potential as implemented in the full-potential local-orbital (FPLO) code [102]. The exchange-correlation functionals were considered at the generalized gradient approximation (GGA) level [160]. We adopted the experimentally measured lattice structures for RO_2 ($R = \text{Ir, Os, and Ru}$) compounds. By projecting the Bloch states into a highly symmetric atomic orbital like Wannier functions (O- p and R- d orbitals), we constructed tight-binding Hamiltonians and computed the intrinsic spin Hall conductivity (SHC) by the linear-response Kubo formula approach in the clean limit [186, 234],

$$\sigma_{ij}^k = e\hbar \int_{\text{BZ}} \frac{d\vec{k}}{(2\pi)^3} \sum_n f_{n\vec{k}} \Omega_{n,ij}^k(\vec{k}), \quad (4.1)$$

$$\Omega_{n,ij}^k(\vec{k}) = -2\text{Im} \sum_{n' \neq n} \frac{\langle n\vec{k} | J_i^k | n'\vec{k} \rangle \langle n'\vec{k} | v_j | n\vec{k} \rangle}{(E_{n\vec{k}} - E_{n'\vec{k}})^2}$$

where $f_{n\vec{k}}$ is the Fermi–Dirac distribution for the n -th band. The spin current operator is $J_i^k = \frac{1}{2} \left\{ v_i, s_k \right\}$, with the spin operator s , the velocity operator $v_i = \frac{1}{\hbar} \frac{\partial H}{\partial k_i}$, and $i, j, k = x, y, z$. $|n\vec{k}\rangle$ is the eigenvector for the Hamiltonian H at the eigenvalue $E_{n\vec{k}}$. $\Omega_{n,ij}^k(\vec{k})$ is referred as the spin Berry curvature as analogy to the ordinary Berry curvature. A $500 \times 500 \times 500$ k -grid in the BZ was used for the integral of the SHC. The SHC σ_{ij}^k refers to the spin current ($j_i^{s,k}$), which flows along the i -th direction with the spin polarization along k , generated by an electric field (E_j) along the j -th direction, i.e., $j_i^{s,k} = \sigma_{ij}^k E_j$.

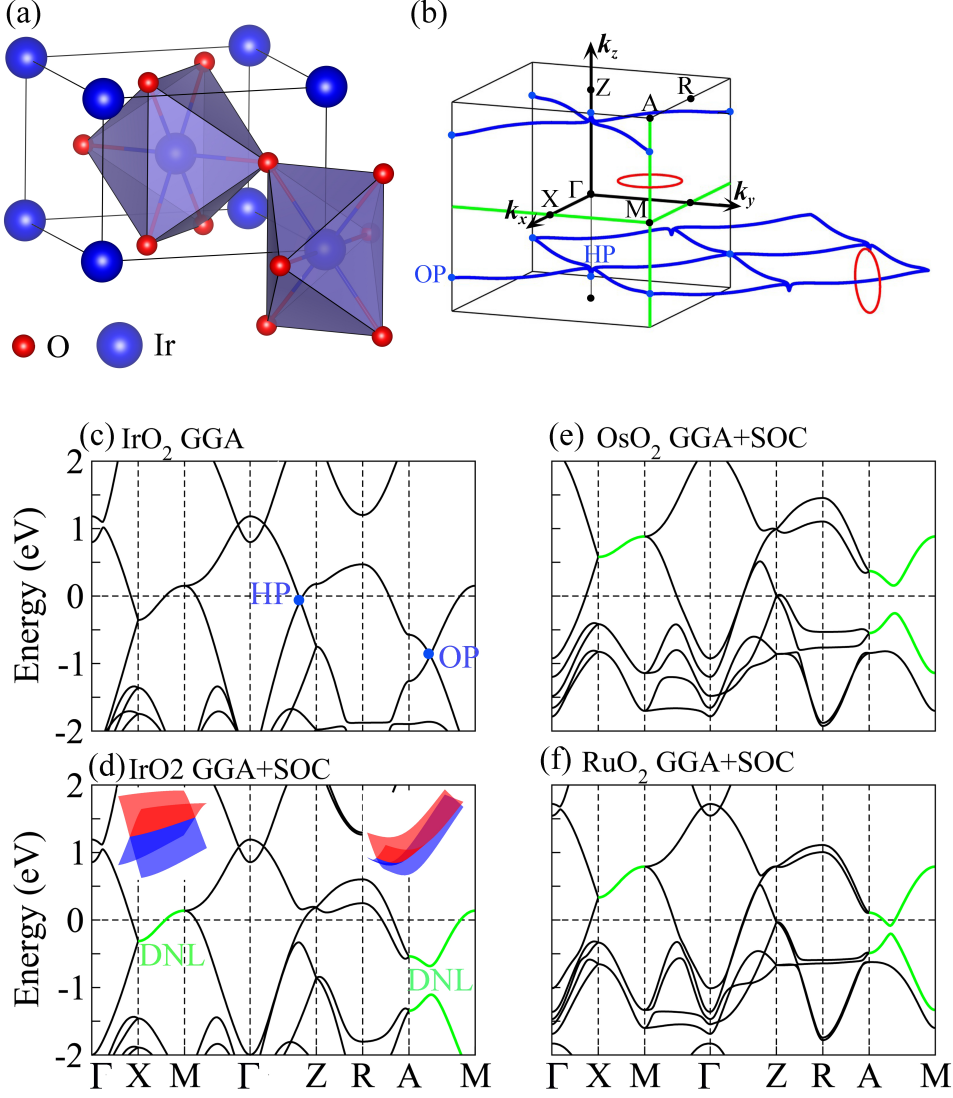


Figure 4.1: (a) Rutile lattice structure of IrO_2 . (b) The tetragonal BZ of IrO_2 . DNLs (blue lines) without SOC form networks inside the BZ, and the corresponding Wilson loop around it (red circle) gives a π Berry phase. The connection points of the network are hexatuple points (HPs) and octuple points (OPs). The DNLs (green) with SOC are lines along X - M and M - A at the BZ boundary, and the Wilson loop around them has zero Berry phase. (c) Band structure for IrO_2 without SOC. The HP and OP are indicated by blue dots. (d-f) Band structures for IrO_2 , OsO_2 , and RuO_2 with SOC. The DNLs on $X - M$ and $M - A$ are highlighted by green lines. In (d), the 3D band dispersion around the DNLs is shown as insets.

4.1.2 Results and Discussions

4.1.3 Nonsymmorphic symmetry

Three compounds RO_2 ($R = \text{Ir, Os, and Ru}$) share the rutile-type lattice structure with space group $P4_2/mnm$ (No. 136), as shown in Fig. 4.1. A primitive unit cell contains two R atoms that sit at the corner and center of the body-centered tetragonal lattice, respectively. One R atom is surrounded by six O atoms that form a distorted octahedron. For space group No. 136, we have the following generator operations,

$$E, m_z, P, n_x \equiv \{m_x|\vec{\tau}\}, n_{4z} \equiv \{c_{4z}|\vec{\tau}\},$$

where $m_{x,z}$ are mirror reflections, c_{4z} is the four-fold rotation, P is the inversion symmetry, n_x and n_{4z} represent nonsymmorphic symmetries, and $\vec{\tau} = (\frac{1}{2}, \frac{1}{2}, \frac{1}{2})$ is the translation of one-half of a body diagonal. Additionally; the time-reversal symmetry T also appears for RO_2 systems.

It is known that electronic bands are doubly degenerate (considering spin and SOC) at every k -point of the BZ owing to the coexistence of P and T . Furthermore, a generic nonsymmorphic symmetry leads to new band crossings and thus higher degeneracies at the BZ boundary. Therefore, the coexistence of P , T , and nonsymmorphic symmetries guarantees four-fold or even larger degeneracies at some k -points of the BZ boundary. As discussed in the following, IrO_2 exhibits a four-fold degeneracy at the BZ edge lines, $X(Y)-M$ and $M-A$ (also see Fig. 4.1d). Consequently, one requires $4n$ electrons for filling these bands to obtain a band insulator. However, a primitive unit cell contains two IrO_2 formula units and in total 42 valence electrons, failing to satisfy the precondition of a band insulator in this nonsymmorphic space group [11, 156]. Therefore, IrO_2 is constrained by the lattice symmetry to be a band metal in the weak interaction case. Recently, it has been reported that IrO_2 cannot become a Mott insulator because of a large bandwidth [89, 96], while several seemingly similar iridates (e.g., Sr_2IrO_4) are known as $5d$ Mott insulators with the $J_{eff} = 1/2$ state [93, 94].

4.1.4 Dirac Nodal lines without SOC

We first investigate the band structures without including SOC. As shown in Fig. 4.1c, six-band and eight-band crossing points (including spin) appear at the $\Gamma - Z$ and $M - A$ axes, respectively, which are noted as a hexatuple point (HP) and an octuple point (OP),

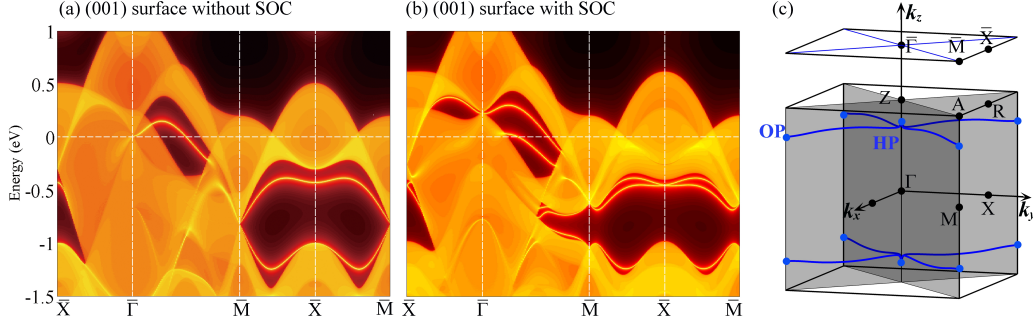


Figure 4.2: Surface band structure for IrO₂ projected to the (001) surface without (a) and with (b) SOC. The brightness of color represents the weight of surface states. (c) The projection of the bulk BZ to the surface BZ with DNLs.

respectively. There is a DNL connecting neighboring HP and OP in the BZ, forming a network in the k -space, as indicated by Fig. 4.1b and 4.3a. Two layers of networks are present above and below the $k_z = 0$ plane respectively, and can be transformed to each other by P or T . DNLs exist inside the (110) and $(\bar{1}10)$ mirror planes and originate from crossing of $d_{x^2-y^2}$ and $d_{xz,yz}$ bands. Here, $d_{x^2-y^2}$ and $d_{xz,yz}$ bands are all doubly degenerate owing to P and T and exhibit opposite eigenvalues -1 and $+1$, respectively, for each mirror reflection. The mirror symmetry protects the four-band-crossing in the absence of SOC.

The topology of a DNL is characterized by the nontrivial Berry phase (or winding number) along with a closed path that includes the DNL. We choose a loop, along which the system is fully gapped as indicated in Fig. 4.1b [193, 254]. The Berry phase for all “occupied” bands is found to be a quantized value, π . This nonzero Berry phase further leads to surface states. When projecting to the (001) surface, the nodal band structure exhibits a local energy gap between \bar{M} and \bar{X} in the surface BZ. Two layers of DNL networks overlap in the (001) surface projection. Thus, one can observe two sets of surface states (spinless) connecting OPs between two adjacent \bar{M} points inside the gap in Fig. surfacea.

When SOC is included and the $SU(2)$ symmetry is broken, these DNLs including HPs and OPs are gapped (see Fig. 4.1d), since there is no additional symmetry protection. On the surface, original spinless surface states split into two Rashba-like spin channels (see Fig. 4.1b). Because of the lack of robust symmetry protection (e.g., P is commonly breaking on the surface), these surface states may appear or disappear according to the surface boundary condition.

4.1.5 Dirac nodal lines with SOC

The $k_x = \pi$ and $k_y = \pi$ planes are actually Dirac nodal planes in the absence of SOC. The presence of SOC gaps these planes and only leaves DNLs along some high-symmetry lines, X - M and M - A . By taking the DNL along X - M as an example, we can understand the four-fold degeneracy by considering time reversal symmetry T , point group symmetries, m_z , P , and nonsymmorphic symmetry n_x . Since $[m_z, H] = 0$ in the $k_z = 0$ plane, we can choose the eigenstates of Hamiltonian H with definite mirror parity for \vec{k} along X - M ,

$$\begin{aligned} H(\vec{k})|\phi_{\pm}(\vec{k})\rangle &= E_{\pm}(\vec{k})|\phi_{\pm}(\vec{k})\rangle \\ m_z|\phi_{\pm}(\vec{k})\rangle &= \pm i|\phi_{\pm}(\vec{k})\rangle \end{aligned} \quad (4.2)$$

where i is from the spin. First, we know $[TP, m_z] = 0$. Therefore, we have

$$\begin{aligned} m_z(TP|\phi_{\alpha}(\vec{k})\rangle) &= TP(m_z|\phi_{\alpha}(\vec{k})\rangle) \\ &= TP(i\alpha|\phi_{\alpha}(\vec{k})\rangle) = -i\alpha(TP|\phi_{\alpha}(\vec{k})\rangle) \end{aligned} \quad (4.3)$$

where $\alpha = \pm 1$. Therefore, $TP|\phi_{\alpha}(\vec{k})\rangle$ is also an eigenstate at \vec{k} ($TP\vec{k} = \vec{k}$) with the mirror parity $-i\alpha$, where $-$ sign is from the complex conjugate in T . Next, we consider the commutation between m_z and the glide mirror symmetry n_x , both of which act in real space (x, y, z) and the spin space simultaneously. In real space, we have

$$\begin{aligned} (x, y, z) &\xrightarrow{n_x} (-x + \frac{1}{2}, y + \frac{1}{2}, z + \frac{1}{2}) \\ &\xrightarrow{m_z} (-x + \frac{1}{2}, y + \frac{1}{2}, -z - \frac{1}{2}) \\ (x, y, z) &\xrightarrow{m_z} (x, y, -z) \\ &\xrightarrow{n_x} (-x + \frac{1}{2}, y + \frac{1}{2}, -z + \frac{1}{2}) \\ m_z n_x &= T_{(0,0,-1)} n_x m_z \end{aligned} \quad (4.4)$$

where $T_{(0,0,-1)} = e^{ik_z}$ is the translation operator when acting on the Bloch wavefunction. In the spin space, $m_z = i\sigma_z$ and $n_x = i\sigma_x$ and thus $m_z n_x = -n_x m_z$. By combining the real space and the spin space, we obtain

$$m_z n_x = e^{ik_z} (-1) n_x m_z = -n_x m_z \quad (4.5)$$

Therefore, $n_x|\phi_\alpha(\vec{k})\rangle$ is also an eigenstate at \vec{k} ($n_x\vec{k} = \vec{k}$), but with a mirror parity $-i\alpha$. Further, the combination of TPn_x leads to one more state $TPn_x|\phi_\alpha(\vec{k})\rangle$ with a mirror parity $+i\alpha$.

In total, we can have four eigenstates, $|\phi_\alpha(\vec{k})\rangle$, $TP|\phi_\alpha(\vec{k})\rangle$, $n_x|\phi_\alpha(\vec{k})\rangle$, and $TPn_x|\phi_\alpha(\vec{k})\rangle$ for $\vec{k}(\pi, k_y, 0)$ along X - M . The mirror parities of m_z are $+i\alpha$ for $|\phi_\alpha(\vec{k})\rangle$ and $TPn_x|\phi_\alpha(\vec{k})\rangle$, and $-i\alpha$ for $TP|\phi_\alpha(\vec{k})\rangle$ and $n_x|\phi_\alpha(\vec{k})\rangle$. Next, we will prove that they are orthogonal to each other, i.e., two eigenstates with the same mirror parity are orthogonal, $\langle \phi_\alpha(\vec{k})|TPn_x|\phi_\alpha(\vec{k})\rangle = 0$. This requires that TPn_x is anti-unitary. In real space, we have

$$\begin{aligned} (x, y, z) &\xrightarrow{Pn_x} \left(x - \frac{1}{2}, -y - \frac{1}{2}, -z - \frac{1}{2}\right) \\ &\xrightarrow{Pn_x} (x - 1, y, z) \end{aligned} \quad (4.6)$$

In the spin space, $P = 1$ and $n_x = i\sigma_x$. Therefore, we have $(Pn_x)^2 = -e^{ik_x}$. Considering $T^2 = -1$ for spinful fermions, we obtain $(TPn_x)^2 = e^{ik_x} = -1$ for $\vec{k} = (\pi, k_y, 0)$. Since TPn_x is an anti-unitary operator that satisfies $\langle \phi|\psi\rangle = \langle TPn_x\psi|TPn_x\phi\rangle$, we have

$$\begin{aligned} &\langle \phi_\alpha(\vec{k})|TPn_x|\phi_\alpha(\vec{k})\rangle \\ &= \langle (TPn_x)^2\phi_\alpha(\vec{k})|TPn_x|\phi_\alpha(\vec{k})\rangle \\ &= -\langle \phi_\alpha(\vec{k})|TPn_x|\phi_\alpha(\vec{k})\rangle = 0 \end{aligned} \quad (4.7)$$

which means the states $TP|\phi_\alpha(\vec{k})\rangle$ and $n_x|\phi_\alpha(\vec{k})\rangle$ are orthogonal to each other.

Therefore, we prove that there are four degenerate orthogonal eigenstates along the X - M line. We point out that the nonsymmorphic symmetry is crucial to protect the four-fold degeneracy, while only P , T , and m_z cannot stabilize DNLs. Likewise, we can also understand the four-fold degeneracy along the M - A line considering m_z , P , T , and another nonsymmorphic symmetry n_{4z} .

These DNLs protected by nonsymmorphic symmetries are similar to those DNLs observed at the BZ edges in ZrSiS and HfSiS (e.g., [26, 180]). We find that the Berry phase along a loop (indicated in Fig. 4.1b) including such a DNL is zero. Therefore, we do not expect apparent topological surface states related to these DNLs. It is still interesting to point out that the density of states scales linearly to the energy for DNLs. Then one can expect different correlation effects in DNL semimetals from a nodal point semimetal and a normal metal [48, 80]. For IrO₂, such DNLs appear at the Fermi energy, while they stay far below the Fermi energy in ZrSiS-type compounds. These DNLs may be responsible for the high conductivity and large magnetoresistance [115, 173].

Table 4.1: SHC for IrO₂, OsO₂, and RuO₂. The Fermi energy is set to the charge neutral point. The SHC is in units of $(\hbar/e)(\Omega \cdot \text{cm})^{-1}$.

	IrO ₂	OsO ₂	RuO ₂
σ_{xy}^z	8	9	83
σ_{zx}^y	-253	-311	-238
σ_{yz}^x	-161	-541	-284

4.1.6 Dirac nodal lines and spin Hall effect

The first type of DNLs, DNL networks without SOC, indicate the existence of a strong SHE in RO_2 . It is known that band anti-crossing induced by SOC can lead to a large intrinsic SHC. To maximize the SHC, one needs to increase the number of band anti-crossing points, i.e., nodal points in the absence of SOC. Therefore, a DNL, an assemble of continual nodal points in the BZ, can induce a strong SHE. The DNL networks that constitute many DNLs will further enhance the SHE. Because such type of DNLs without SOC are usually protected by the mirror symmetry, it will be insightful to look for SHE materials in space groups that host many mirror or glide mirror planes. This argument seems consistent with the fact that current best SHE materials are usually Pt and W metals(e.g. [69, 206]) from the high-symmetry space groups.

Next, we compute the intrinsic SHC for RO_2 compounds following Eq. 5.3 based on the band structure including SOC. The SHC σ_{ij}^k is a second-order tensor with 27 elements. The number of independent nonzero elements of the SHC tensor is constrained by the symmetry of the system. We have only three independent nonzero elements, $\sigma_{xy}^z = -\sigma_{yx}^z$, $\sigma_{zx}^y = -\sigma_{xz}^y$, and $\sigma_{yz}^x = -\sigma_{zy}^x$. We list their values in Table I for all the three compounds. The SHC of OsO₂ is larger than that of RuO₂, and Os-5*d* bands exhibit much stronger SOC than Ru-4*d* bands. The SHC is dependent on the Fermi energy of the system. Because Ir has one more electron than Os/Ru, the Fermi surface of IrO₂ is higher than that of OsO₂ and RuO₂ although their band structures look very similar (see Figs. 4.1d-f). Thus, IrO₂ displays a smaller SHC than OsO₂ although Ir has stronger SOC. For all the three compounds, the SHC is very anisotropic, as can be seen from Table I. Here, the largest SHC of RO_2 is still smaller than that of Pt [$\sigma_{xy}^z \sim 2000(\hbar/e)(\Omega \cdot \text{cm})^{-1}$]. However, RO_2 may exhibit a large spin Hall angle (the ratio of the SHC over the charge conductivity) owing to their high resistivity compared to a pure metal, as already found in IrO₂ [58].

Here, we also demonstrate the direct correspondence between DNLs and the SHC. Since the SHC is obtained by integrating the spin Berry curvature over the BZ, we show the distribution of $\Omega_{n,yz}^x(\vec{k})$ in the (110) mirror plane that hosts DNLs. In the band structure

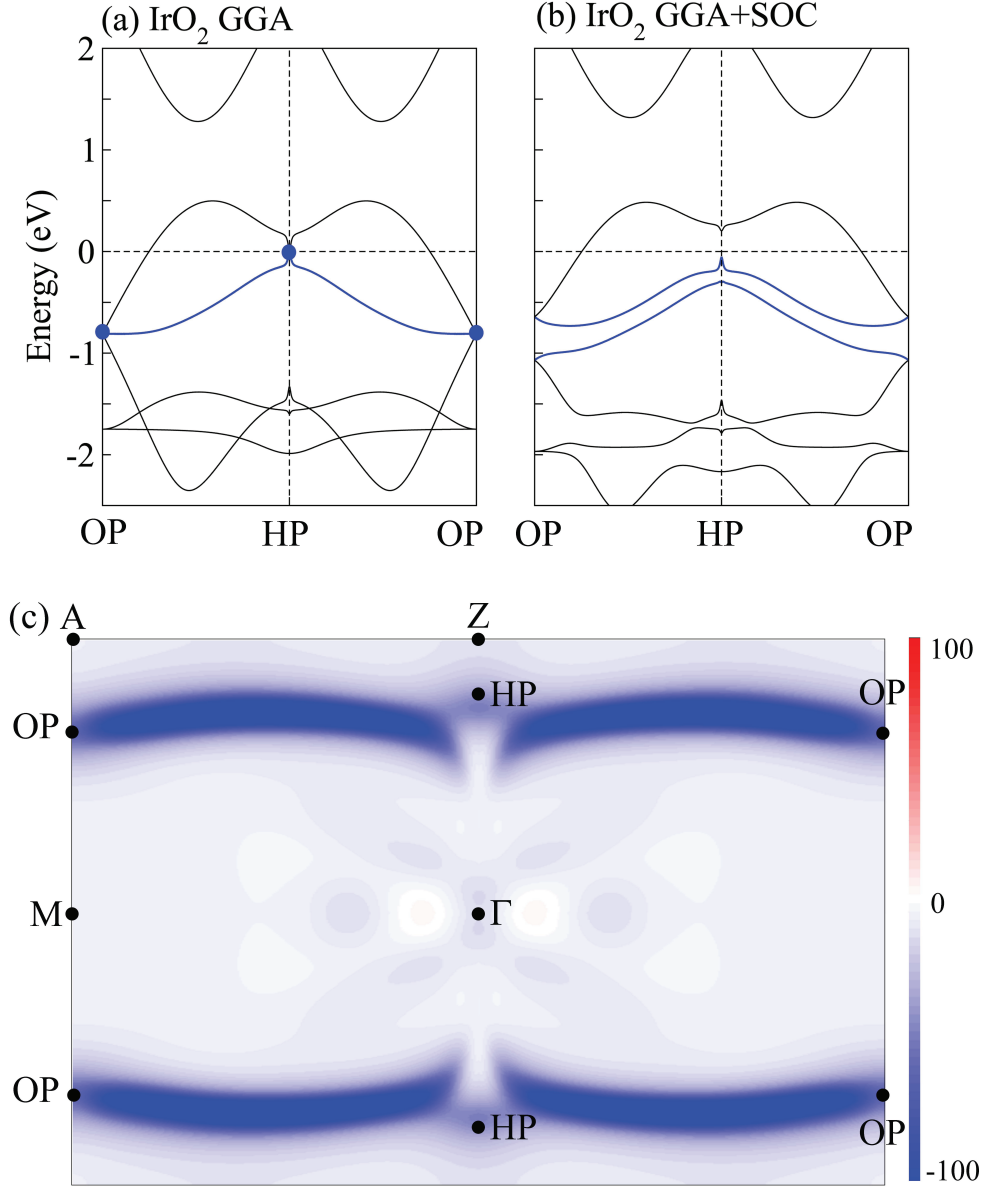


Figure 4.3: DNLs and SHE in IrO₂. (a) Band structure without SOC along a first-type DNL. Blue curves represent the DNL that connects the HP and the OP in the (110) or $(\bar{1}\bar{1}0)$ mirror plane. (b) Band structure with SOC along the same line. A gap opens along the nodal line due to SOC. (c) Distribution of the spin Berry curvature $\Omega_{n,yz}^x(\vec{k})$ inside the (110) mirror plane. Here, $\Omega_{n,yz}^x(\vec{k})$ is summarized over all bands below the SOC split gap. It is clear that the spin Berry curvature is dominantly contributed by the DNL regions. The blue and red colors represent negative and positive values of the spin Berry curvature in unit of $(\text{\AA}^{-1})^2$

along DNLs in Fig. 4.3, the SOC clearly gaps a DNL that connects a HP and an OP. Correspondingly, one can find two "hot lines" of the spin Berry curvature, which is the anti-crossing region of the DNLs. Thus, it is clear that the first-type DNLs contribute to a large SHC for IrO₂-type materials. In contrast, the second-type DNLs at the BZ edges (e.g., that along *M-A* in Fig. 4.3c) show a slight contribution to the SHC.

4.1.7 Conclusions

To summarize, we found two types of DNLs in metallic rutile oxides IrO₂, OsO₂, and RuO₂. First-type DNLs form networks that extend in the whole BZ and appear only in the absence of SOC, which induces surface states at the boundary. The second type of DNLs is stable against SOC because of the protection of nonsymmorphic symmetry. Because of the SOC-induced gap for first-type DNLs, a large intrinsic SHE can be realized in these compounds. This explains the strong SHE observed in IrO₂ in the previous experiment. Moreover, our calculation suggests that OsO₂ will behave even better than IrO₂ in SHE devices, as OsO₂ shows a larger intrinsic SHC. Our work implies that first-type DNLs (or nodal points that can be gapped by SOC) and the SHE maybe commonly related to each other, indicating new guiding principles to search for DNLs in SHE materials or enhance the SHE by DNLs in the band structure. For example, it will be insightful to look for SHE materials in high-symmetry space groups with many mirror or glide mirror planes, which can induce the first type of DNLs.

4.2 Spin current from temperature gradient: spin Nernst effect in InBi

Because of the recent experimental progress also the spin Nernst effect (SNE), the thermo-electrical counterpart of the SHE, has attracted much interest. Empirically strong SHEs and SNEs are associated with *d*-band compounds, such as transition metals and their alloys – the largest spin Hall conductivity (SHC) in a *p*-band material is $\sim 450 (\hbar/e) (\Omega \cdot \text{cm})^{-1}$ for a Bi-Sb alloy, which is only about a fifth of platinum. This raises the question whether either the SHE and SNE are naturally suppressed in *p*-bands compounds, or favorable *p*-band systems were just not identified yet. Here we consider the *p*-band semimetal InBi, and predict it has a record SHC $\sigma_{xy}^z \approx 1100 (\hbar/e) (\Omega \cdot \text{cm})^{-1}$ which is due to the presence of nodal-lines in its band structure, similar to what we have seen in Ir₂ family of materials. Also the spin-Nernst conductivity $\alpha_{zx}^y \approx 1.2 (\hbar/e)(A/m \cdot K)$ is very large, but our analysis

shows its origin is different as the maximum appears in a different tensor element. This insight gained on InBi provides guiding principles to obtain a strong SHE and SNE in p -band materials and establishes a more comprehensive understanding of the relationship between the SHE and SNE.

4.2.1 Introduction

Apart from the SHE, a transverse spin current can be generated by a temperature gradient instead of an electric field, which constitutes the spin Nernst effect (SNE) [95, 133, 184]. The SNE can also be formulated via the Kubo formula approach based on the electronic band structure [6, 9, 30, 141, 185, 208, 209, 227, 234]. Thus the electronic band structure plays a crucial role in searching and designing strong SHE and SNE materials.

Though the precise reason is not clear to date, empirically materials with a strong SHE are primarily dominated by d -orbital-related compounds [74, 99, 177, 186, 206] such as 5d-transition metals and alloys. The largest spin Hall conductivity (SHC) found in p -band materials is in a Bi-Sb alloy [46, 174] at only around 450 $((\hbar/e)(\Omega \cdot \text{cm})^{-1})$. Very recently, it was found that the nodal line band structure could generate strong SHCs because of the large local SBC [199, 200]. Employing this guiding principle, we theoretically predict a large intrinsic SHC of about 1100 $((\hbar/e)(\Omega \cdot \text{cm})^{-1})$ in the p -band semimetal InBi. Substitution of the electric field by a temperature gradient, reveals a large spin Nernst conductivity (SNC) of about 1.2 $(\hbar/e)(A/m \cdot K)$ at 300 K. This shows that the SNE and SHE can be strongly enhanced by the topological band structure and that the large SNC and SHC need not be intrinsically weak in cheaper and therefore commercially more attractive p -band materials. Though both the intrinsic SHE and SNE can be understood from the SBC, their largest value appears at different tensor elements, implying different origins.

4.2.2 Spin Nernst formalism and model parameter

To understand the effect of the nodal line band structure on the SHE and especially the SNE, we first consider two simple systems by effective model Hamiltonians. From the high-symmetry Benervig-Hughes-Zhang (BHZ) model for quantum spin Hall insulators [8], where s_z is maintained as a good quantum number (see the method section), the band structure is presented as a nodal line without considering spin-orbit coupling (SOC). As soon as SOC is taken into consideration, the linear band crossing is gapped and leads to a quantized spin Hall conductance in the band gap [199]. Though the spin Hall conduc-

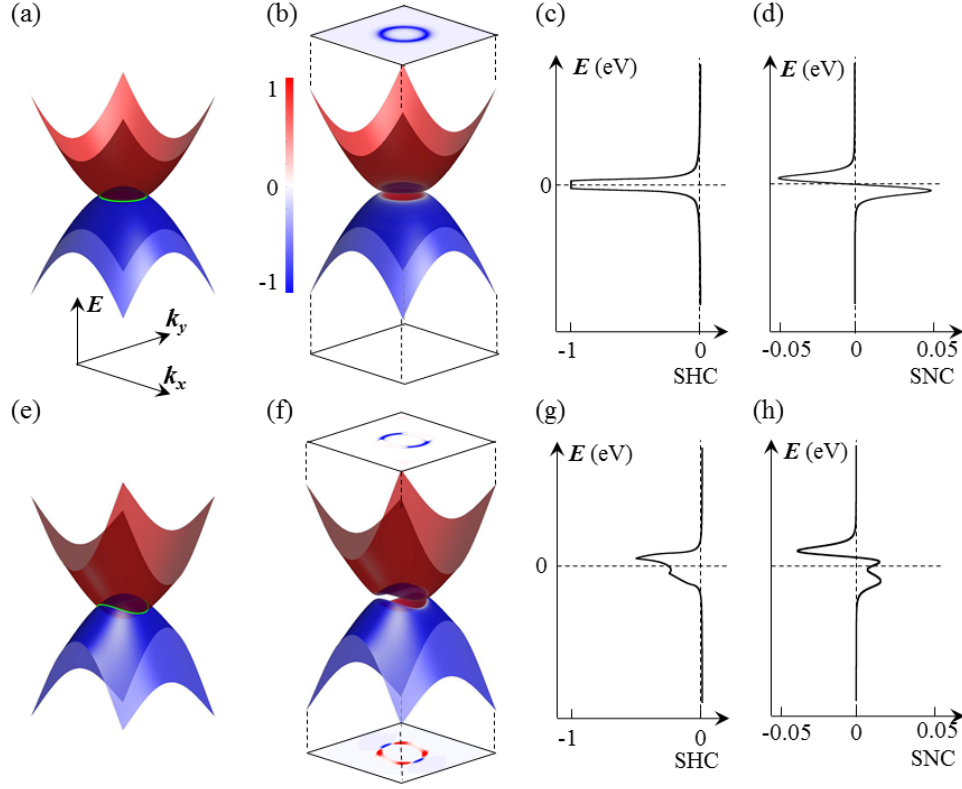


Figure 4.4: Band structure, SHC, and SNC in the effective BHZ model. (a) Nodal line energy dispersion of the high symmetry effective BHZ model without the inclusion of SOC. (b) SOC breaks the nodal line with opening a global band gap after SOC is taken into consideration. The distribution of SBC and SNBC at charge neutral point are given above and below the energy dispersion. (c-d) Energy-dependent SHC and SNC, respectively. (e-h) The same as (a-d) but for the symmetry-reduced model. The color bars are in arbitrary units.

tance reaches the maximum value at the charge neutral point, the spin Nernst conductance is zero there because of the electron and hole symmetry. Comparing the SBC and spin Nernst Berry curvature (SNBC) distribution in reciprocal space, it is found that the SNBC is zero at any k -point, while the SBC has a strong hot ring from the nodal-line-like band anti-crossing (see Fig. 4.4(b)). From Eq. (4), one can find that the SNBC is actually a redistribution of the SBC because of the temperature effect, which should be canceled out by the electron-hole symmetry. To break the electron-hole symmetry, we have reduced the symmetry of the effective model Hamiltonian, making the system non-insulating. Compared to the high-symmetry model, the nodal line in the symmetry-reduced model has a dispersion in energy space, and the Fermi velocities are different along the x and y directions. As there is no global gap, the spin Hall conductance is not quantized anymore (Figs. 4.4(f–g)). Meanwhile, a finite spin Nernst conductance appears at the charge neutral point. In Figs. 4.4(b,f), we also analyzed the SBC and SNBC distribution in the $k_x - k_y$ plane. Because of the dispersion of the nodal ring, the high intensity of the SBC changes from a hot ring to two hotspots, resulting in a non-zero SNBC, as presented in the lower panel of Fig. 4.4(f). By integrating the SNBC, one can obtain a non-zero spin Nernst conductance at the charge neutral point. Therefore, the non-zero SNC must break the balance of the SHC distribution in energy space.

The SNC is calculated via

$$\alpha_{ij}^k = \frac{1}{T} \int_{BZ} \frac{d^3k}{(2\pi)^3} \sum_n \Omega_{n,ij}^{S,k}(\vec{k}) [(E_n - E_F) f_{n\vec{k}} + k_B T \ln(1 + \exp \frac{E_n - E_F}{-k_B T})], \quad (4.8)$$

A $500 \times 500 \times 500$ k -grid in the BZ was used for the integral of the SHC and SNC. For convenience, we call $\Omega_{n,ij}^{SN,k} = \Omega_{n,ij}^{S,k}(\vec{k}) [(E_n - E_F) f_{n\vec{k}} + k_B T \ln(1 + \exp \frac{E_n - E_F}{-k_B T})]$ the SNBC.

The BHZ model [8] around the Γ point is written in the form of

$$H_{eff}(\vec{k}) = \begin{pmatrix} H(\vec{k}) & \\ & H^*(-\vec{k}) \end{pmatrix} \quad (4.9)$$

$$H(\vec{k}) = \varepsilon(\vec{k}) + d_i(\vec{k})\sigma_i$$

where σ_i are the Pauli matrices, $d_1 + id_2 = A(k_x + ik_y)$, and $d_3 = M - B(k_x^2 + k_y^2)$. In our calculations, for Figs. 4.4(a–c), we have set the parameters of $A = -0.1$ eV Å, $B = -0.5$ eV Å², and $M = 0.1$ eV.

In order to obtain a non-zero SNC, we break the balance of the SHC by reducing the

symmetry:

$$H_{eff}(\vec{k}) = \begin{pmatrix} H'(\vec{k}) & \\ & H^{*'}(-\vec{k}) \end{pmatrix} \quad (4.10)$$

$$H'(\vec{k}) = d'_1\sigma_1 + d'_2\sigma_2 + \begin{pmatrix} M_1 - (B_1k_x^2 + B_2k_y^2) & 0 \\ 0 & -[M_2 - (B_2k_x^2 + B_1k_y^2)] \end{pmatrix}$$

where $d'_1 + id'_2 = A_1k_x + iA_2k_y$. The parameters are $A_1=0.05$ eV \AA , $A_2=0.1$ eV \AA , $B_1=-1$ eV \AA^2 , $B_2=-0.5$ eV \AA^2 , $M_1=-0.3$ eV, and $M_2=-0.5$ eV.

To perform the integral in the whole BZ, we projected the continuous $\vec{k} \cdot \vec{p}$ model to the lattice by the replacement of $k_i = (1/a)\sin(ak_i)$ and $k_i^2 = (2/a^2)(1 - \cos(ak_i))$ with lattice constant $a=1$ \AA .

4.2.3 Band structure, spin Hall, and spin Nernst conductivity

The specific material InBi has been reported to exhibit nonsymmorphic symmetry-protected nodal lines at the edge of the Brillouin zone (BZ) [45]. However, these kinds of nodal lines are just band degeneracies from band folding between different BZs. According to previous studies, this kind of nodal line normally does not exhibit any topological charge or SBC and, therefore, cannot generate the SHE and SNE [200]. In the current work, we find another type of nodal line inside the BZ protected by mirror symmetry and rotation symmetry, which generates a strong SHE and SNE. As shown in Fig. 4.5(b), there are four classes of nodal lines, located in the high-symmetry planes of $k_{x,y}=0$, $k_z=0$, and $k_x \pm k_y=0$, and high-symmetry line of $\Gamma - Z$, respectively. Without including the SOC, the inverted bands have opposite mirror eigenvalues of 1 and -1, respectively, in the planes of $k_{x,y}=0$, $k_z=0$, and $k_x \pm k_y=0$, leading to the double degeneracy (not considering the spin degree of freedom) of nodal line linear band crossings. Along the high-symmetry line of $\Gamma - Z$, the double band degeneracy (highlighted by magenta in Fig. 4.5(c)) is due to the c_4 rotation symmetry with respect to the z -axis. As long as SOC is taken into consideration, the spin rotation symmetry is broken and the linear band crossings are also gapped out, as indicated in Figs. 4.5(c-d). This kind of band anti-crossing from the SOC is often accompanied by strong band entanglements and yields a large SBC.

The $\text{SHC}(\sigma_{ij}^k)$ and $\text{SNC}(\alpha_{ij}^k; i, j, k = x, y, z)$ are $3 \times 3 \times 3$ tensors, representing the spin current \vec{J}_{si}^k generated by the electric field \vec{E} via $\vec{J}_{si}^k = \sum_j \sigma_{ij}^k \vec{E}_j$ and temperature gradient

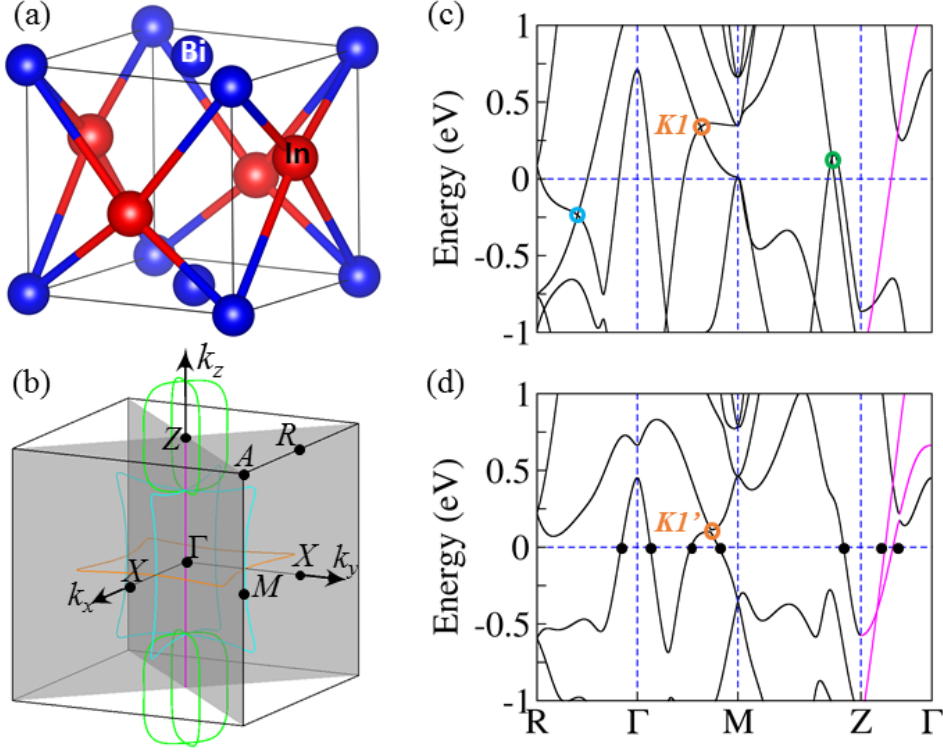


Figure 4.5: Lattice and electronic band structure for InBi. (a) Tetragonal lattice structure in InBi with space group $P4/nmm$. The lattice parameters are $a = b = 4.9846 \text{ \AA}$ and $c = 4.8116 \text{ \AA}$. (b) Nodal line distribution in BZ. Here only the nodal lines without the inclusion of SOC are shown, and they are gapped out by SOC. (c-d) Energy dispersion without and with the inclusion of SOC. The nodal ring linear band crossings in $k_z = 0$, $k_{x,y} = 0$, and $k_x \pm k_y = 0$ planes, are labeled by orange, cyan, and green circles, respectively, in (c). The band anticrossing opened by SOC on the Γ - M is also labeled by an orange circle. The nodal line on Γ - Z is highlighted by magenta. The transition point of band occupation are labeled by black dots in (d).

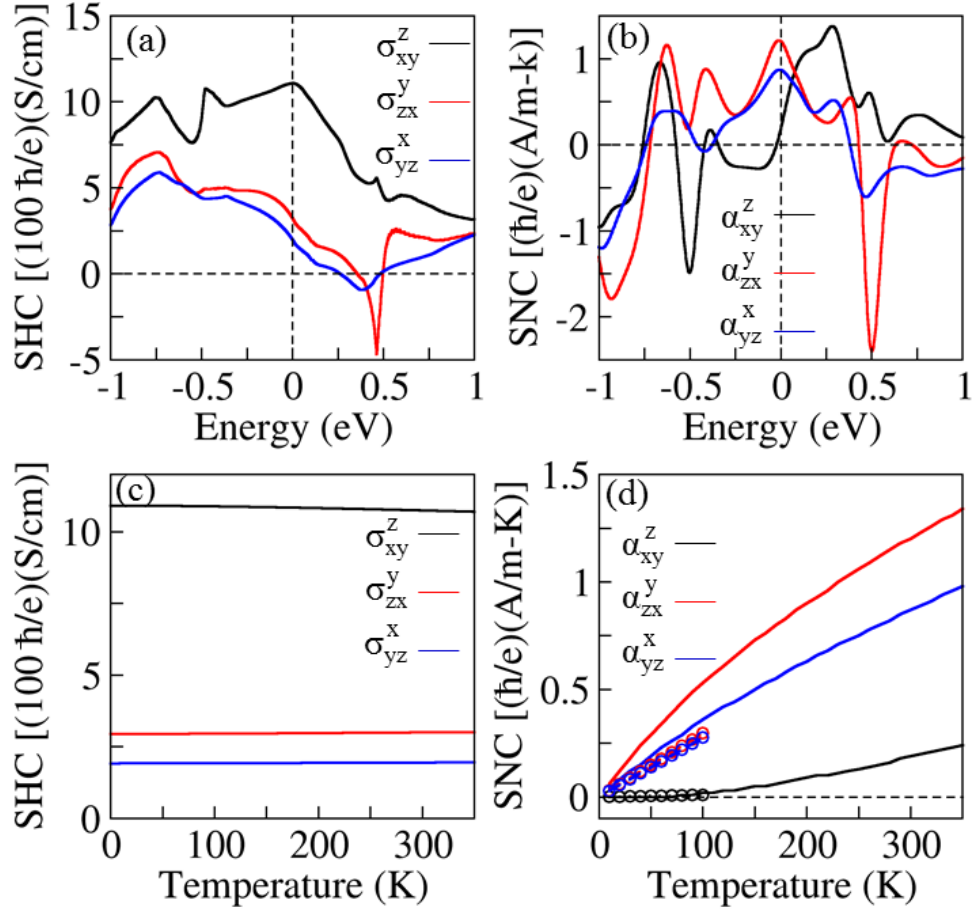


Figure 4.6: SHC and SNC in InBi. (a, b) Energy dependent SHC and SNC for the three independent tensor elements. (c,d) The evolution of SHC and SNC as the function of temperature. The solid curves and empty circles in (d) are from equation 4.8 and Mott relation, respectively.

$\vec{\nabla T}$ by $\vec{J}_{S_i}^k = \sum_j \alpha_{ij}^k \vec{\nabla T}_j$, where $\vec{J}_{S_i}^k$ flows along the i -direction with the spin-polarization along the k -direction, and \vec{E}_j and $\vec{\nabla T}_j$ are the j -component of the electric field \vec{E} and temperature gradient $\vec{\nabla T}$, respectively. Based on linear response theory, for the specific space group $P4/nmm$, there are only three independent tensor elements for both the SHC and SNC tensor [100, 182]:

$$\underline{X}^x = \begin{pmatrix} 0 & 0 & 0 \\ 0 & 0 & X_{yz}^x \\ 0 & -X_{zx}^y & 0 \end{pmatrix}, \underline{X}^y = \begin{pmatrix} 0 & 0 & -X_{yz}^x \\ 0 & 0 & 0 \\ X_{zx}^y & 0 & 0 \end{pmatrix}, \underline{X}^z = \begin{pmatrix} 0 & X_{xy}^z & 0 \\ -X_{xy}^z & 0 & 0 \\ 0 & 0 & 0 \end{pmatrix} \quad (4.11)$$

where $X=\sigma$ and α represent the SHC and SNC, respectively. Therefore, there are only three independent non-zero elements, following the relation of $X_{xy}^z = -X_{yx}^z$, $X_{zx}^y = -X_{zy}^x$, and $X_{yz}^x = X_{xz}^y$.

Our calculations are fully consistent with the symmetry analysis. From the energy-dependent SHC (Fig. 4.6(a)), one can see that the largest tensor element appears at σ_{xy}^z , which can reach up to about 1100 $((\hbar/e)(\Omega \cdot \text{cm})^{-1})$. Thus far, this is the only SHC above 1000 $((\hbar/e)(\Omega \cdot \text{cm})^{-1})$ in the reported p -orbital compounds. This large value is robust in a large energy window from E_0 –0.5 eV to the charge neutral points in the hole-doped range. Therefore, hole doping is preferred from the SHE point of view. Furthermore, we find that the SHC is robust with respect to temperature. The SHC only varies less than 5% from 0 K to room temperature, which is very similar to that in platinum [133]

From the above model analysis, we already know that a large SHC does not imply a large SNC. To obtain a large SNC, the balance of the SHC distribution in energy space must be broken. Based on this understanding, the robustness of the SHC in energy space is not beneficial for the SNE, and a large SNC should not appear at α_{xy}^z . Indeed, the tensor element of α_{xy}^z is very small, at about 0.2 $((\hbar/e)(A/m \cdot K))$ at 300 K. However, a quite large SNC is achieved at α_{xy}^z , which can reach up to about 1.2 $((\hbar/e)(A/m \cdot K))$ at 300 K. Because the SNE is very sensitive to temperature, we also analyzed the evolution of the SNC as a function of temperature. As presented in Fig. 4.6(c), α_{xy}^z is near-zero at low temperatures below 100 K, and the α_{zx}^y and α_{yz}^x are also small ($\sim 0.5 ((\hbar/e)(A/m \cdot K))$). All three components increase steadily with temperature, but α_{zx}^y and α_{yz}^x increase much faster than α_{xy}^z . This is the reason why α_{xy}^z is so small even above 300 K.

For the conversion efficiency of the charge and heat current to the spin current not only the absolute values of the SHC and SNC are important, but also the spin Hall angle (SHA)

Table 4.2: SHC, SHA, SNC, and SNA for InBi and Pt. The chemical potential is at charge neutral point, and the temperature is 300 K. The unit for SHC and SNC are $(\hbar/e)(\Omega \cdot \text{cm})^{-1}$ and $((\hbar/e)(A/m \cdot K))$, respectively.

		SHC	SHA	SNC	SNA
InBi	X_{xy}^z	1100	0.3	0.2	0.04
	X_{zx}^y	300	0.09	1.2	0.28
	X_{yz}^x	200	0.06	0.9	0.21
Pt	X_{xy}^z	2200	0.11	3.0	0.20

and the spin Nernst angle (SNA). Due to the lack of experimental values for the electrical conductivity and thermopower of InBi film, we have just used the bulk values to estimate the SHA and SNA. Because of the large SHC (σ_{xy}^z) and small charge conductivity [35], the SHA ($\theta_{SH,xy}^z$) can reach up to 0.3 (see Table I). Hence, the SHA in InBi is close to or even larger than that in the 5d transition metals of Pt, W, and Ta. Similarly, in combination with a large SNC and low thermalpower, the SNA can reach up to 0.21 and 0.28 for $\theta_{SN,yz}^x$ and $\theta_{SN,zx}^y$, respectively. It should be noted that the thermalpower in bulk is normally much larger than that in film form, so the SNA should also be much larger.

At low temperature, the SNC can be understood from the Mott relation as the derivative of the SHC with respect to energy [111, 235]:

$$\alpha_{ij}^k = -\frac{\pi^2}{3} \frac{k_B^2 T}{e} \frac{\partial \sigma_{ij}^k(E)}{\partial E} \quad (4.12)$$

At a temperature of about 10 K, the SNC from both the Mott relation and SNBC formalism converge to about zero. From Fig. 4.6(c), one can easily see that the ANC from the two different formalisms of formula (2) and (3) agree very well with each other at low temperatures from 10 to 100 K. As the slopes of the energy-dependent SHC for σ_{zx}^y and σ_{yz}^x are significantly sharper than that in α_{xy}^z , α_{zx}^y and α_{yz}^x are much larger than α_{xy}^z at temperatures far away from 0 K.

We known that the intrinsic SHC and SNC can be understood as the integral of the SBC and SNBC in the whole BZ. As the maximum elements are different for the SHC and SNC, we choose the SBC and SNBC from two different components of $\sigma(\alpha)_{xy}^z$ and $\sigma(\alpha)_{zx}^y$ to observe their distribution and temperature effect for the evolution from the SBC to SNBC. From the above band structure analysis, we know that the special band structures mainly focus on the high-symmetry planes of $k_{x,y}=0$, $k_z=0$, and $k_x \pm k_y=0$, and high-symmetry line of $\Gamma - Z$. Therefore, we have analysed the SBC and SNBC distribution in

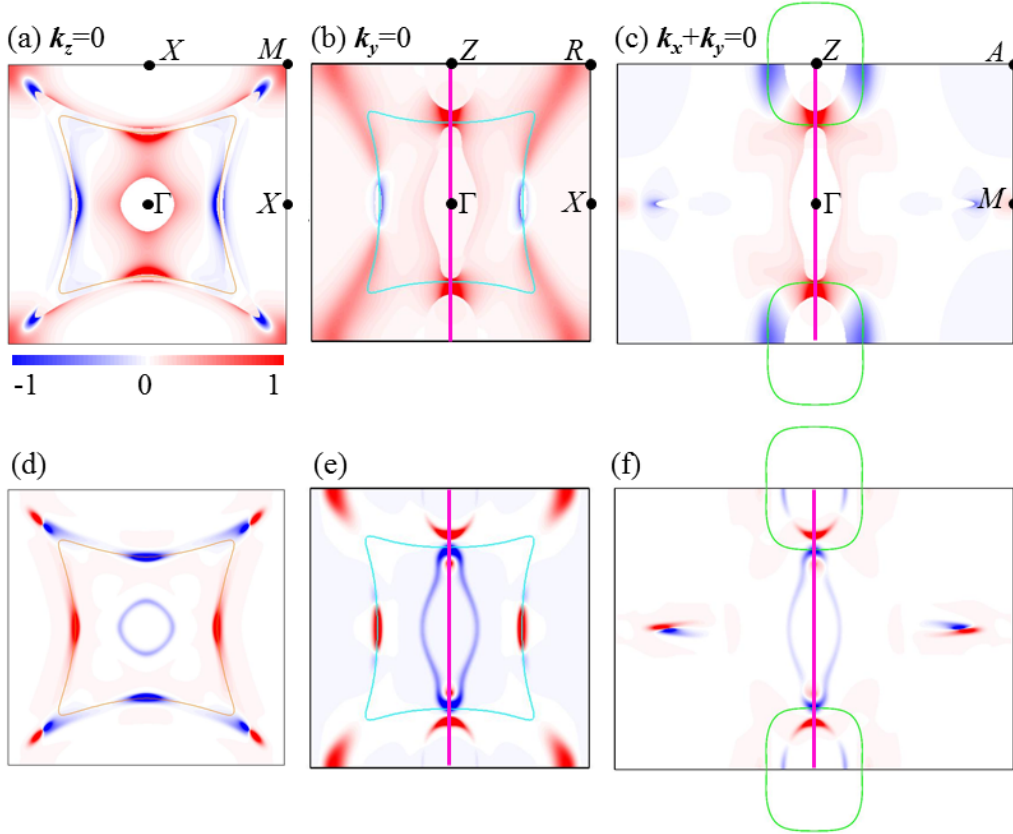


Figure 4.7: Local Berry curvature $\Omega_{xy}^{S,z}(\vec{k})$ and $\Omega_{xy}^{SN,z}(\vec{k})$ distribution on high symmetry planes (a-c) and (d-f) are SBC and SNBC distribution on the three planes of $k_z=0$, $k_y=0$, and $k_x + k_y=0$ planes, respectively. The nodal lines are also shown by orange, cyan, green circles, and magenta curves, respectively. The color bars are in arbitrary units.

all the three planes of $k_{x,y}=0$, $k_z=0$, and $k_x + k_y=0$.

First, we analyzed the component of $\Omega_{xy}^{S,z}$, which contributes to the large tensor element for the SHC. Fixing the energy at the charge neutral point, as shown in Fig. 4.7(a), the large SBC in the $k_z=0$ plane is mainly dominated by the Γ -centered nodal ring. In addition, there exist other hotspots on the Γ - M line near the M point, which is not exactly located on the nodal ring. This is because the SBC is indeed determined by the band structure with the SOC. The gapless linear band crossing transforms to a band anti-crossing by the SOC. Comparing the linear crossing point $K1$ (highlighted by orange circle) in Fig. 4.5(b) and the corresponding band anti-crossing point $K1'$ in Fig. 4.5(c), we can find that the $K1'$ is much closer to the M point than $K1$. Therefore, the hotspots along Γ - M do not exactly lie on the corner of the gapless nodal ring. In addition, the Fermi level does not lie in the band gap of the band anti-crossing but slightly cuts the conduction band, which also implies the strong entanglement between the conduction and valence band around the band anti-crossing points.

Meanwhile, in the $k_y=0$ plane, there are two types of hotspots, one from the nodal ring in the $k_y=0$ plane and the other on the line Z - Γ - Z . The $\Omega_{xy}^{S,z}$ from the nodal line on Z - Γ - Z is much larger, which is related to the magenta bands in Figs. 4.5(c-d). There are also two types of hotspots in the $k_x + k_y=0$ plane, one from Z - Γ - Z as that in the $k_y=0$ plane and the other from the Z -point-centred nodal ring. From Figs. 4.7(b-c), one can find some empty parts with a zero SBC and shape edge transition, such as the Γ - and Z -centred areas. This is due to the shape evolution of the band occupation, such as the band around the Γ point, as shown in Fig. 4.5(d). For the k point from R to Γ , the valence band changes from an occupied band to a non-occupied band after a transition k point (highlighted by the black dot). Similar behavior is also exhibited for the other areas with an empty SBC.

After taking the temperature effect into consideration, the SNBC ($\Omega_{xy}^{SN,z}$) also mainly originates from the four classes of nodal lines as that for the SBC. The main difference is that the shape edge transitions in the empty SBC areas are replaced by the hotspot of the SNBC (see Figs. 4.7(d-f)). This is because the temperature effect smoothens considerably the transition of the band occupation, and the shape transition of the SBC around the edge of the empty area yields a large SNBC.

Similar to $\Omega_{xy}^{S,z}$, the component of $\Omega_{zx}^{S,y}$ is dominated by the four classes of nodal lines, but the volume of the negative part is larger than that of $\Omega_{xy}^{S,z}$ (see Figs. 4.8(a-c)), leading to a relatively smaller absolute value for the SHC tensor element σ_{zx}^y . As the negative SNBC ($\Omega_{zx}^{NS,y}$) primarily originates from the sharp transition of the SBC around the edge

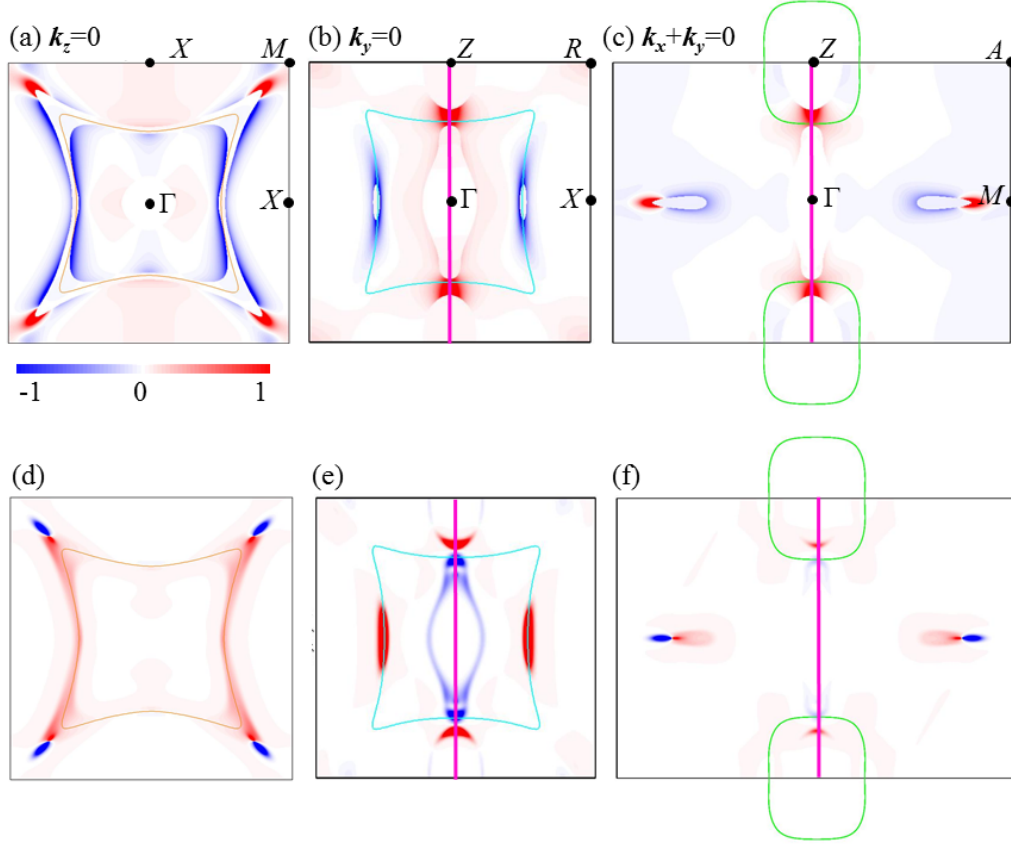


Figure 4.8: Local Berry curvature distribution on high symmetry planes for the component of $\Omega_{zx}^{S,y}(\vec{k})$ and $\Omega_{zx}^{SN,y}(\vec{k})$ (a-c) and (d-f) are SBC and SNBC distribution on the three planes of $k_z=0$, $k_y=0$, and $k_x+k_y=0$ planes, respectively. The nodal lines are also shown by orange, cyan, green circles, and magenta curves, respectively. The color bars are in arbitrary units.

of the zone with an empty SBC, the small magnitude of $\Omega_{zx}^{S,y}$ generates a relatively small SNBC for the same tensor component. Comparing Figs. 4.7 and 4.8, the Γ -centered negative hot rings for $\Omega_{xy}^{SN,z}$ in Figs. 4.7(d) and (f) are almost invisible in Figs. 4.8(d) and (f) for $\Omega_{zx}^{SN,y}$. Moreover, the Γ -centered negative hot ring for $\Omega_{zx}^{SN,y}$ in Fig. 4.8(e) is also considerably weaker than $\Omega_{xy}^{SN,z}$ in Fig. 4.8(d). Because both components of α_{xy}^z and α_{zx}^y are positive values, the smaller negative $\Omega_{zx}^{NS,y}$ directly leads to a larger α_{zx}^y in comparison to α_{xy}^z .

In summary, from our calculations, we predict a large SHC and SNC in the p -band semimetal InBi. Due to the contribution of the nodal lines in the band structure of InBi, the σ_{xy}^z component of the SHC can reach up to about 1100 $((\hbar/e)(\Omega \cdot \text{cm})^{-1})$, the only SHC above 1000 $((\hbar/e)(\Omega \cdot \text{cm})^{-1})$ in the reported p -band systems. In contrast to the intuition that a large SHC is always accompanied by a large SNC, we find that the largest value for the SHC and SNC appear in a different third-order tensor element. The size of the SNC is mainly dependent on the breaking of the balance of the SHC distribution in energy space and gives the largest SNC of about 1.2 $((\hbar/e)(A/m \cdot K))$ at the tensor element α_{zx}^y , which is close to that in the 5d transition metal platinum. These results on InBi provide more general guiding principles to obtain a strong SHE and SNE in commercially more attractive p -band compounds and establishes a more comprehensive understanding of the relationship between the SHE and SNE in these materials.

5 Spin current in non-collinear antiferromagnets: spin Hall and spin polarized current

In this chapter, we study both the intrinsic spin Hall effect (even) and extrinsic spin-polarized charge current (odd) in non-collinear antiferromagnets. Moreover, the shape of the spin current response tensor under various magnetic order is investigated both with and without SOC. We find the spin Hall effect could arise from the non-collinear magnetic order without SOC.

In the previous chapter, we have shown Eq. (1.11), (1.10) could describe time reversal even and odd spin-conductivity respectively. Since the later one (known as the spin-polarized charge current) requires the breaking of time-reversal symmetry, it is normally believed to exist only in ferromagnets. Our study reveals that the spin-polarized charge current could also exist in non-collinear antiferromagnets with zero net magnetic moment, which paves the way to realize the antiferromagnetic metallic or tunneling junction.

5.1 Spin Hall effect emerging from a noncollinear magnetic lattice without spin-orbit coupling

The spin Hall effect, which converts a charge current into a transverse spin current, has long been believed to be a phenomenon induced by the spin-orbit coupling. Here, we identify an alternative mechanism to realize the intrinsic SHE through a noncollinear magnetic structure that breaks the spin rotation symmetry. No spin-orbit coupling is needed even when the scalar spin chirality vanishes, different from the case of the topological Hall effect and topological SHE reported previously. In known noncollinear antiferromagnetic compounds Mn_3X ($X = \text{Ga}, \text{Ge}, \text{and Sn}$), for example, we indeed obtain large spin Hall conductivities based on *ab initio* calculations.

5.1.1 introduction

The SHE in materials is generally believed to rely on spin-orbit coupling (SOC) [67, 74, 129, 186]. In typical SHE devices, the generated spin current is injected into a ferromagnet (FM) and consequently switches its magnetization via the spin-transfer torque [119, 134] or drives an efficient motion of magnetic domain walls. [158, 247] The SHE is conceptually similar to the well established anomalous Hall effect (AHE). In recent decades, the understanding of the intrinsic AHE [142] and intrinsic SHE [141, 185] was significantly advanced based on the concept of the Berry phase, [234] which originates directly from the electronic band structure. Although the AHE requires the existence of SOC in an FM, it also appears in a non-coplanar magnetic lattice without SOC, where an electron acquires a Berry phase by hopping through sites with a noncoplanar magnetic structure (nonzero scalar spin chirality) [153, 203], later referred as the topological Hall effect (THE) [14]. Thus, in experiment the THE-induced Hall signal is considered as a signature of the skyrmion phase with chiral spin texture [90, 146]. Provoked by THE, recent numerical simulations of the spin scattering by a single skyrmion indicated the presence of a finite SHE even without SOC [15, 145, 250], which is termed as a topological SHE. Thus, the topological SHE has been presumed to stem from the Berry phase due to the nonzero spin chirality of the skyrmion. However, the origin of the spin current is elusive in the topological SHE, for it is hard to separate it from the spin-polarized charge current of THE. Here, we pose new questions one step further. Is the skyrmion-like spin texture (nonzero scalar spin chirality) always necessary to generate a SHE without SOC? What is the generic condition for a SHE without SOC?

We propose a mechanism to realize the SHE with the noncollinear magnetic structure but without SOC. The crucial role of SOC is to break the spin rotational symmetry (SRS) in SHE. Alternatively, it is known that common noncollinear magnetic textures can also violate the SRS, thus resulting in the SHE. Different from THE and topological SHE in symmetry, such an SHE appears universally for the noncollinear magnetic lattice, regardless of the scalar spin chirality. For example, it can even emerge in a coplanar magnetic structure where the scalar spin chirality is zero. Here, we first prove the principle from the symmetry analysis in a simple lattice model. Then, we demonstrate the existence of a strong SHE in several known materials Mn_3X ($X = \text{Ga, Ge, and Sn}$) [143, 144] by *ab initio* calculations without including SOC.

		Collinear FM	Collinear AFM	Coplanar	Noncoplanar
Without SOC	AHE	×	×	×	✓
	SHE	×	×	✓	✓
With SOC	AHE	✓	×	✓	✓
	SHE	✓	✓	✓	✓

Figure 5.1: Symmetry conditions for the existence (✓) or absence (×) of AHE and SHE in collinear FM, collinear AFM, coplanar, and noncoplanar magnetic lattices with and without SOC. Note that the SHE is symmetry allowed when the magnetic ordering is coplanar (but noncollinear) even without SOC (see text).

5.1.2 Double-exchange model and symmetry analysis

The existence of the SHE and AHE in metals is determined by symmetry (in insulators apart from symmetry also the topology of the electronic structure is important). The symmetry of magnetic systems is normally described in terms of magnetic space groups, which contain, apart from the spatial symmetry operations, also the time-reversal symmetry operation. In absence of SOC (or other terms in the Hamiltonian that couple the magnetic moments to the lattice such as the shape anisotropy), however, the symmetry of the magnetic systems is higher than that contained in the magnetic space groups since the spins can be rotated independently of the lattice. This can be illustrated by considering the following minimal Hamiltonian

$$H = t \sum_{\langle ij \rangle \alpha} c_{i\alpha}^\dagger c_{j\alpha} - J \sum_{i\alpha\beta} (\boldsymbol{\sigma} \cdot \mathbf{n}_i)_{\alpha\beta} c_{i\alpha}^\dagger c_{i\beta}, \quad (5.1)$$

known as the double-exchange model (*s-d* model) [2, 37, 259] which describes itinerant *s* electrons interacting with local *d* magnetic moments. We assume that magnetic moments are only contributed by the spin degrees of freedom. Here, α and β stand for spin up and spin down, respectively. The first term is the nearest neighbor hopping term with $\langle ij \rangle$

5.1 Spin Hall effect emerging from a noncollinear magnetic lattice without spin-orbit coupling

denoting the nearest neighbor lattice sites. In the second term, J is the Hund's coupling strength between the conduction electron and the on-site spin moment, $\boldsymbol{\sigma}$ is the vector of Pauli matrices, and \mathbf{n}_i is the spin magnetic moment on site i . The magnetic texture is defined by the pattern of \mathbf{n}_i . In such a Hamiltonian, spin rotation only rotates the magnetic moments \mathbf{n}_i . The corresponding symmetry groups are thus formed by combining the magnetic space groups with spin rotations. [12, 116] Such symmetry groups are referred to as spin-space groups. They apply generally for non-interacting Hamiltonians in absence of spin-orbit coupling.

We focus here only on the intrinsic contribution to the AHE and SHE, however, the other (extrinsic) contributions have the same symmetry and thus the symmetry discussion in the following is general. The intrinsic AHE and intrinsic SHE are well characterized via the Berry curvature formalism [67, 142, 186, 234] as we have presented in previous chapter. Here we write out the Berry curvature of spin Berry curvature expression for the convenience of symmetry discussion. The anomalous Hall conductivity $\sigma_{\alpha\beta}$ can be evaluated by the integral of the Berry curvature $\Omega_{\alpha\beta}^n(\mathbf{k})$ over the Brillouin zone for all the occupied bands, where n is the band index. It should be noted that this method can also be applied to THE, although it is commonly interpreted using the real space spin texture. Here, $\sigma_{\alpha\beta}$ corresponds to a 3×3 matrix and indicates a transverse Hall current j_α generated by a longitudinal electric field \mathbf{E} , which satisfies $J_\alpha = \sigma_{\alpha\beta} E_\beta$. Within a linear response, Berry curvature can be expressed as

$$\Omega_{n,\alpha\beta}(\vec{k}) = 2i\hbar^2 \sum_{m \neq n} \frac{\langle \psi_{n\mathbf{k}} | \hat{v}_\alpha | \psi_{m\mathbf{k}} \rangle \langle \psi_{m\mathbf{k}} | \hat{v}_\beta | \psi_{n\mathbf{k}} \rangle}{(E_n(\vec{k}) - E_m(\vec{k}))^2}, \quad (5.2)$$

where n and m are band indices, and $\psi_{n\mathbf{k}}$ and $E_{n\mathbf{k}}$ denote the Bloch wave functions and eigenvalues, respectively, and $\hat{\mathbf{v}}$ is the velocity operator. Replacing the velocity operator with the spin current operator $\hat{J}_\alpha^\gamma = \frac{1}{2}\{\hat{v}_\alpha, \hat{s}_\gamma\}$, where \hat{s}_γ is the spin operator, we obtain the spin Berry curvature,

$$\Omega_{n,\alpha\beta}^\gamma(\mathbf{k}) = 2i\hbar^2 \sum_{m \neq n} \frac{\langle \psi_{n\mathbf{k}} | \hat{J}_\alpha^\gamma | \psi_{m\mathbf{k}} \rangle \langle \psi_{m\mathbf{k}} | \hat{v}_\beta | \psi_{n\mathbf{k}} \rangle}{(E_{n\mathbf{k}} - E_{m\mathbf{k}})^2}. \quad (5.3)$$

The SHC ($\sigma_{\alpha\beta}^\gamma$; $\alpha, \beta, \gamma = x, y, z$) is a third-order tensor ($3 \times 3 \times 3$) and represents the spin current $J_{s,\alpha}^\gamma$ generated by an electric field \mathbf{E} via $J_{s,\alpha}^\gamma = \sigma_{\alpha\beta}^\gamma E_\beta$, where $J_{s,\alpha}^\gamma$ is a spin current flowing along the α -direction with the spin-polarization along the γ -direction, and $f_n(\mathbf{k})$ is the temperature dependent Fermi-Diract distribution.

We know that AHE vanishes while SHE remains if the time-reversal symmetry (operator T) exists in the system. In Eq. 5.2, T reverses the velocities $\hat{v}_{\alpha,\beta}$ and brings an additional “-” sign by the complex conjugate. Thus, $\sigma_{\alpha\beta} = 0$ owing to $\Omega_{n,\alpha\beta}(\vec{k}) = -\Omega_{n,\alpha\beta}(-\vec{k})$. In contrast, In Eq. 5.3, T generates one more “-” sign by reversing the spin in J_α^γ . Then, $\sigma_{\alpha\beta}^\gamma$ can be nonzero since $\Omega_{n,\alpha\beta}^\gamma(\vec{k})$ is even in k -space. In a magnetic system without SOC, T is broken, but a combination of T and a spin rotation (operator S) can still be a symmetry. For example, a coplanar magnetic system shows a TS symmetry, in which S rotates all spins by 180° around the axis perpendicular to the plane. Since S does not act on $\hat{v}_{\alpha,\beta}$, TS causes vanishing $\sigma_{\alpha\beta}$ just as T alone. In a general noncoplanar magnetic lattice, the TS symmetry is naturally broken, because one cannot find a common axis about which all spins can be rotated 180° at the same time, and thus the AHE can exist without SOC.

The situation is different for the SHE since J_α^γ in Eq. 5.3 contains an additional spin operator. As a consequence, (assuming that S is a rotation around the z axis) TS forces $\Omega_{n,\alpha\beta}^{x/y}(\vec{k})$ to be odd where spin \hat{s}_x or \hat{s}_y is reversed by TS , but $\Omega_{n,\alpha\beta}^z(\vec{k})$ to be even where \hat{s}_z is unchanged by TS . Then, one can obtain zero $\sigma_{\alpha\beta}^{x/y}$ but nonzero $\sigma_{\alpha\beta}^z$. In a collinear magnetic lattice there exists more than one spin rotation S such that TS is a symmetry of the system and thus all of the $\sigma_{\alpha\beta}^\gamma$ components have to vanish. Therefore, we can argue that SHE can exist without SOC in general noncollinear magnetic lattices, regardless of FM, AFM, or the scalar spin chirality (coplanar or noncoplanar). In contrast, the AHC is zero for a coplanar magnetic lattice (zero scalar spin chirality), since TS acts as T alone in Eq. 5.2.

When SOC is included, SHE is allowed by symmetry in any crystal, [182] while the AHE, on the other hand, can be present in magnetic systems that are not symmetric under time reversal combined with a translation or inversion (for example, a conventional collinear AFM). We summarize the necessary conditions for the existence of AHE and SHE in systems with and without SOC in Fig. 5.1.

To demonstrate that the SHE can indeed be nonzero without SOC, we consider the s - d Hamiltonian (5.1) projected on a kagome lattice with the so-called $q = 0$ magnetic order, shown in Fig. 5.2(a). Such a coplanar AFM order is well studied in theory [27, 153] and appears in many realistic materials even at room temperature, for example Mn_3X ($X = \text{Ir, Ga, Ge, and Sn}$) [108, 143, 144, 263, 264, 267] as we discuss in the following. For comparison, the SOC effect is also considered by adding to H in Eq. 5.1,

$$H_{\text{so}} = it_2 \sum_{\langle ij \rangle \alpha\beta} v_{ij} (\boldsymbol{\sigma} \cdot \mathbf{n}_{ij})_{\alpha\beta} c_{i\alpha}^\dagger c_{j\beta}, \quad (5.4)$$

where v_{ij} is the antisymmetric Levi-Civita symbol and n_{ij} are a set of coplanar vectors anticlockwise perpendicular to the lattice vector R_{ij} , as defined in Ref. [27] and t_2 is the SOC strength.

We first analyze the symmetry of the SHC tensor for the $q = 0$ magnetic order. Note that we use the Cartesian coordinate systems defined in Fig. 5.2. As discussed above, the existence of the TS symmetry leaves only $\sigma_{\alpha\beta}^z$ terms in the absence of SOC. Further, the combined symmetry TM_x , in which M_x is the mirror reflection along x and flips \hat{s}_z and \hat{v}_x in Eq. 5.3, leads to $\sigma_{xx}^z = \sigma_{yy}^z = 0$. We further obtain only two nonzero SHC tensor element $\sigma_{xy}^z = -\sigma_{yx}^z$ by considering the three-fold rotation around z . The magnetic order shown in Fig. 5.2(b) will also be relevant for the discussion in the following. This magnetic configuration differs from the $q = 0$ case only by a two-fold spin rotation around the y -axis and thus, without SOC its symmetry is exactly the same as that of the $q = 0$ case.

Setting the Hund coupling constant $J = 1.7t$ and SOC strength $t_2 = 0$, we calculate the spin Berry curvature via Eq. 5.3. As expected, we find nonzero SHC σ_{xy}^z fully in agreement with the symmetry considerations. Figures 5.3a and 5.3b show the band structures with $t_2 = 0$ and $t_2 = 0.2t$, respectively. One can see that SOC modifies slightly the band structure by gapping some band crossing points such as the BZ corners (K). Without SOC, we already observe nonzero σ_{xy}^z , while adding SOC reduces σ_{xy}^z slightly at the Fermi energy that is set between the first and second bands at about -2.7 eV. We plot corresponding spin Berry curvature Ω_{xy}^z in the hexagonal BZ in Figs. 5.3d and 5.3e. Large Ω_{xy}^z appears in the BZ without SOC, leading to net σ_{xy}^z . The SOC simply brings an extra contribution to σ_{xy}^z at the band anti-crossing region around the K point.

5.1.3 Realistic materials

After proving the principle, we now identify materials that show strong SHE with negligible contribution from SOC. We naturally consider Mn_3X ($\text{X}=\text{Ga}, \text{Ge}, \text{Sn}, \text{and Ir}$) compounds, since they exhibit non-collinear AFM order at room temperature (the AFM Néel temperature is over 365 K). Our recent *ab initio* calculations showed a sizable intrinsic SHE by including SOC [267]. Here, we further point out that SHE still presents without SOC and SOC actually plays a negligible effect for SHE in these materials.

The primitive unit cell of Mn_3Ga , Mn_3Ge and Mn_3Sn (space group $P6_3/mmc$, No. 194) includes two Mn_3X planes that are stacked along the c -axis according to a “-AB-AB-” sequence. Inside each plane, Mn atoms form a kagome-type lattice with Ga, Ge, or Sn

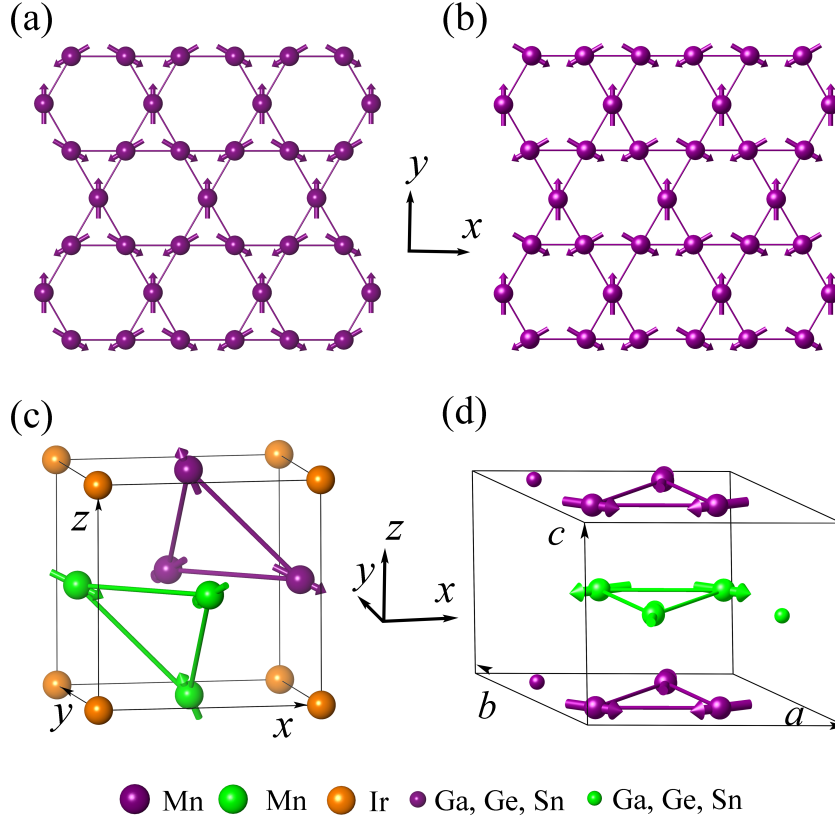


Figure 5.2: Noncollinear order in kagome lattice and the magnetic structure of Mn_3Ir and Mn_3X ($\text{X} = \text{Ga}, \text{Ge}, \text{and Sn}$). (a) The $q = 0$ order in the kagome lattice, with magnetic moments located as 2D Mn plane in Mn_3Ir , (b) Two-fold spin rotation around y -axis of configuration (a), corresponding to Mn planes in Mn_3X ($\text{X} = \text{Ga}, \text{Ge}, \text{Sn}$), (c) The face-centered cubic crystal structure of Mn_3Ir , (d) The hexagonal crystal structure of Mn_3X ($\text{X} = \text{Ga}, \text{Ge}, \text{and Sn}$).

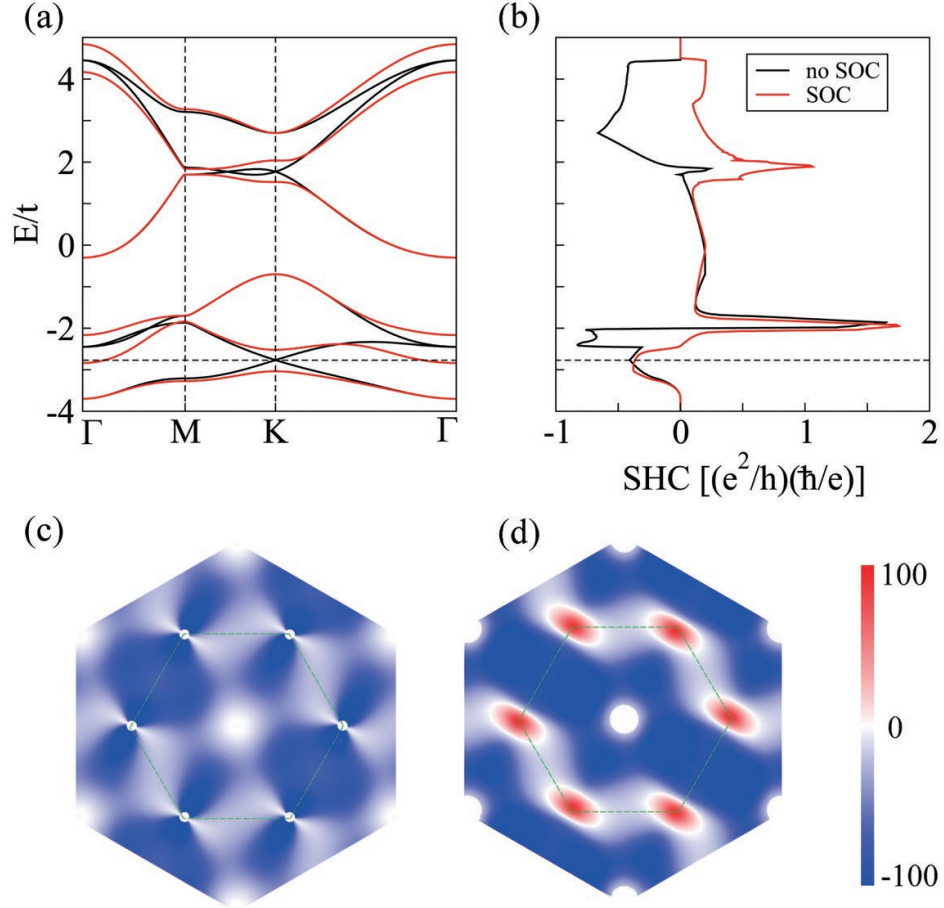


Figure 5.3: Electronic band structures $q = 0$ order in kagome lattice, (a) without and with SOC. (b) Energy-dependent SHC σ_{xy}^z . (c) Spin Berry curvature Ω_{xy}^z distribution of first BZ at Fermi energy -2.7 eV (horizontal line) without SOC and (d) with SOC.

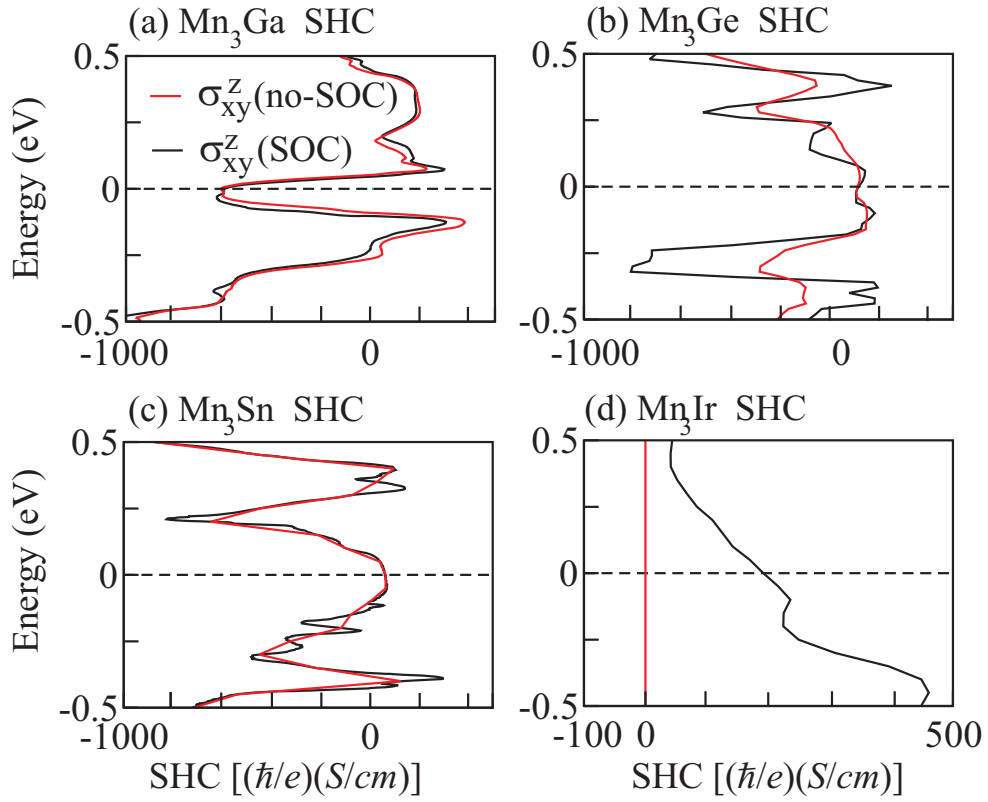


Figure 5.4: Energy-dependent SHC tensor elements of σ_{xy}^z with and without SOC for (a) Mn_3Ga , (b) Mn_3Ge , (c) Mn_3Sn , and (d) Mn_3Ir . The Fermi energy is indicated by the dashed horizontal line.

lying at the center of the hexagon formed by Mn. Both the *ab initio* calculation [263] and neutron diffraction measurements [88, 104, 154] show that the Mn magnetic moments exhibit noncollinear AFM order, where the neighboring moments are aligned at an angle of 120° , as in Fig. 5.2(b). Large AHE in room temperature has recently been reported in Mn_3Ge and Mn_3Sn . [143, 144] These materials also exhibit other exotic phenomena including the Weyl semimetal phase, [243] magneto-optical Kerr effect, [53] anomalous Nernst effect, [113] and topological defects. [118] Distinct from hexagonal Mn_3X compounds, the Mn_3Ir (space group $Pm\bar{3}m$, No. 221) crystallizes in a face-centered cubic structure with Mn atoms in the [111] planes forming a kagome lattice with the $q = 0$ magnetic order.

The symmetry of the SHE without SOC in these materials can be understood using a similar approach as we used for the 2D kagome lattice. The hexagonal Ga, Ge, and Sn materials can be viewed as stacking versions of the kagome lattice and thus we find that the symmetry of SHE is the same as the 2D kagome lattice, i.e. only $\sigma_{xy}^z = -\sigma_{yx}^z$ is nonzero. However, we find that SHE must vanish in Mn_3Ir without SOC, which is imposed by the higher symmetry of the cubic magnetic lattice. For completeness, we list the tensor matrices without and with SOC for all these compounds in the appendix.

Since the SHC tensor shape imposed by the symmetry has been systematically investigated for these materials in Ref. [267], we only discuss one of the largest SHC tensor elements σ_{xy}^z based on the *ab initio* calculations [105] of the SHC. For comparison, we show the SHC without and together with SOC in Fig. 5.4. In the absence of SOC, Ga, Ge, and Sn compounds indeed exhibit nonzero SHC $\sigma_{xy}^z = -613, 115$, and $90 (\hbar/e)(\Omega \cdot \text{cm})^{-1}$, respectively, at the Fermi energy. One can see that SOC induces very few changes in the band structure and thereafter modifies the SHC weakly, especially at the Fermi energy for Ga, Ge, and Sn compounds. It is intuitive to observe comparable σ_{xy}^z values for Ge and Sn compounds, despite the fact that Sn exhibits much larger SOC than Ge. These facts further verifies that the noncollinear magnetic structure, rather than SOC, is dominant for the SHE. The Ga compound shows an opposite sign in SHC compared to the Ge/Sn compound, since Ga has one valence electron fewer than Ge/Sn and the Fermi energy is lower in Mn_3Ga than in $\text{Mn}_3\text{Ge}/\text{Mn}_3\text{Sn}$.

5.1.4 discussion

Understanding the role SOC plays in the SHE is important for the fundamental understanding of the SHE, but also for practical reasons. It can help with the search for materials with large SHE since in non-magnetic or collinear magnetic materials, SOC is necessary

for SHE and thus the presence of heavy elements is generally required for large SHE. The SHE without SOC proposed in this work suggests a new strategy to design SHE materials without necessarily involving heavy elements. In noncollinear systems, the Rashba effect can also appear without SOC [120]. The spin texture in the band structure may depend sensitively on the real space spin texture. For example, we found that band structure spin texture is different between the Kagome lattice and the triangular lattice.

We propose the general, necessary symmetry-breaking requirements (Fig. 5.1) for SHE without SOC. It is worth noting that SHE can become zero without SOC in some non-collinear magnetic lattice where additional symmetries forces the SHE to vanish. For example, we have shown that in Mn_3Ir the SHE vanishes in absence of SOC even though it has a noncollinear magnetic structure. This is a consequence of its high-symmetrical cubic structure. Similar situation could happen for AHE without SOC in a noncoplanar magnetic lattice, such as the AFM skyrmion system [145].

In conclusion, we have shown that the SHE can be realized by a non-chiral coplanar magnetic structure without involving the SOC. The noncollinearity of the magnetic lattice can break the spin rotation symmetry and consequently allow the existence of SHE. By *ab initio* calculations, we further predicted that such an SHE without SOC can be observed in noncollinear AFM compounds Mn_3X ($X = \text{Ga}, \text{Ge}, \text{and Sn}$). From our symmetry considerations, an extrinsic SHE can appear when breaking the spin rotational symmetry. Thus, we expect the extrinsic effect to also exist in our systems. Its amplitude will depend on the details of the scattering, and cannot be estimated without microscopic calculations, though in general for SHE the intrinsic contribution tends to be the dominant contribution. By providing a general theoretical, symmetry based understanding of the SHE, our work motivates a comprehensive search for SHE materials among noncollinear magnetic systems, that not necessarily involve heavy elements. In addition, the close relation between the SHE and the magnetic order suggests that the SHE may be used vice versa, as a probe to establish and symmetry restrict the ground state magnetic structures of long-range ordered antiferromagnets.

Regarding the strong correlated system, we would discuss the spin liquid material as an example. RuCl_3 has a rich magnetic phase diagram, with a complex zig-zag type AFM long-range order at low temperatures, and even a quantum spin liquid phase in applied magnetic field. According to our work, non-magnetic and collinearly ordered phases have vanishing SHE without SOC. For the quantum spin liquid phase, it remains unclear whether SHE appears without SOC. If yes, SHE would be a promising probe to the spin liquid phase. We will study this very interesting question in the future.

5.2 Spin-polarized current in non-collinear antiferromagnets

Noncollinear antiferromagnets, such as Mn_3Sn and Mn_3Ir , were recently shown to be analogous to ferromagnets in that they have a large anomalous Hall effect. Here we show that these materials are similar to ferromagnets in another aspect: the charge current in these materials is spin-polarized. In addition, we show that the same mechanism that leads to the spin-polarized current also leads to a transverse spin current, which has a distinct symmetry and origin from the conventional spin Hall effect. We illustrate the existence of the spin-polarized current and the transverse spin current by performing *ab initio* microscopic calculations and by analyzing the symmetry. We discuss possible applications of these novel spin currents, such as an antiferromagnetic metallic or tunneling junction.

5.2.1 Introduction.

Spintronics is a field that studies phenomena in which both spin and charge degree of electron play an important role. Many of the key spintronics effects are based upon the existence of spin currents. Two main types of spin currents are utilized: the spin-polarized currents in ferromagnets (FMs) and the spin currents due to the spin Hall effect (SHE) which are transversal to the charge current and appear even in non-magnetic materials. The most important effects that originate from the spin-polarized currents in FMs are the giant and the tunneling magnetoresistance effects (GMR and TMR) [86,135,137] and the spin-transfer torque (STT) [169,190]. These effects are utilized for magnetic sensing and in the magnetic random access memories (MRAMs) [92]. This memory is non-volatile and has speed and density comparable to the widely used dynamic random access memory. The SHE is pivotal for spintronics since it allows transforming charge current into a spin current. It is responsible (though other effects can contribute) for the spin-orbit torque (SOT) [119,134] in multilayer heterostructures, which can be used for efficient and fast switching of FM layers. The SOT is now also being explored for use in MRAMs [151,163].

While spintronics has traditionally utilized FM and non-magnetic materials, in the past few years also antiferromagnetic (AFM) materials have attracted a considerable interest. AFMs offer some unique advantages compared to FMs, but are much less explored (see reviews [5,87,127]). AFMs have a very fast dynamics, which allows for switching on ps timescale [64,98,172]. Furthermore, there exists a wide range of AFM materials, including

many insulators and semiconductors, multiferroics [43] and superconductors [122]. Utilizing (and also studying) AFMs is difficult, largely because the magnetic order in AFMs is hard to detect and to manipulate.

AFM spintronics has so far focused mostly on collinear AFMs in which the electrical current is not spin-polarized. This limits the spintronics effects that can be observed in such AFMs. Here we show that this limitation only relates to the simple collinear AFMs. We demonstrate by means of symmetry arguments and ab-initio calculations that in non-collinear AFMs novel type of spin currents occur. These spin currents have a longitudinal component (i.e., flowing along the same direction as the electrical current) or in other words the electrical current is spin-polarized. Unlike in FMs, these spin currents also have a large transverse component. Such a spin current resembles the SHE in that it is a spin current transverse to the charge current, however, it is fundamentally distinct from the SHE. A key distinction is that the spin currents we discuss here are odd under time-reversal, whereas the SHE is even. This is analogous to the distinction between normal current and the anomalous Hall effect (AHE).

Successful experimental demonstrations of electrical detection and manipulation of AFMs has utilized relativistic effects which do not rely on the spin-polarized current [54, 106, 157, 214, 214, 216, 258]. These methods could be used to develop AFM spintronic devices, but they have some disadvantages compared to the methods used in FMs. Our work shows that in non-collinear AFMs spintronics could instead be developed along a similar route as FM spintronics. As an example, we propose that a magnetoresistance and STT will be present in an AFM junction.

The transverse spin currents are also important for spintronics as they allow for similar functionality as the SHE, but have a different origin and symmetry. This could, for example, be useful for the SOT since the high symmetry of SHE in commonly used metals is limiting [128]. Additionally, the odd spin currents are directly relevant for experiments which demonstrated a large SOT in non-collinear AFM/FM heterostructures [152, 170, 211, 233, 264].

We illustrate the existence of the novel spin currents on non-collinear AFMs Mn_3Sn and Mn_3Ir , which have triangular magnetic configurations shown in Figs 5.5(a),(b). These AFMs have recently attracted attention because they were shown to have a large anomalous Hall effect (AHE) [27, 108, 143, 144] as well as a magneto-optical Kerr effect [53], even though they have only a very small net magnetization (which is not the origin of these effects). The conventional SHE in the non-collinear AFMs was already theoretically studied in depth in Ref. [267], thus we focus here only on the odd spin currents.

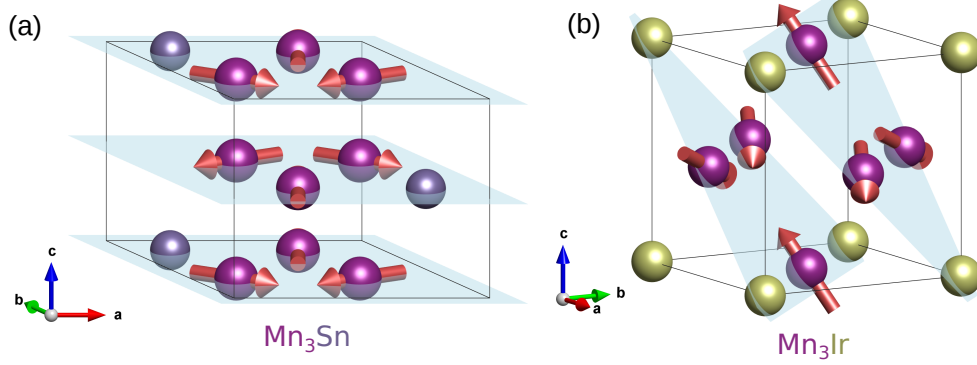


Figure 5.5: (a) Crystal and magnetic structure of Mn_3Sn (as well as Mn_3Ga and Mn_3Ge) and (b) Mn_3Ir (as well as Mn_3Rh , Mn_3Pt).

5.2.2 Symmetry analysis and calculations.

The response of metals to electric fields can be described well by linear response theory. Here we use the so-called constant Γ approximation, and calculate the spin-polarized current from response formula shown in chapter 3.2.

Eqs. (1.10) and (1.11) transform differently under time-reversal because time-reversal is an anti-unitary operator, which transforms the matrix elements as: $\langle n\mathbf{k} | \hat{A} | n\mathbf{k} \rangle \rightarrow \langle n\mathbf{k} | T \hat{A} T | n\mathbf{k} \rangle^*$ [81]. Because of the complex conjugation, the term (1.11) will contain additional minus under a time-reversal transformation compared to the term (1.10). Thus for conductivity the term (1.10) is even under time-reversal, while the term (1.11) is odd. Note that equivalently these terms are also even resp. odd under the reversal of all magnetic moments. The even part describes the ordinary conductivity, while the odd part describes the AHE. Since AHE is odd under time-reversal it can be nonzero only in a magnetic system (assuming non-interacting electrons). Traditionally, it has been considered for FMs only, but recently it was shown that Eq. (1.11) is also nonzero and relatively large in non-collinear AFMs [27, 108]. Collinear AFMs are typically symmetrical under simultaneous time-reversal and lattice translation or under simultaneous time-reversal and inversion and these symmetries prohibit the existence of AHE. In non-collinear AFMs, both of these symmetries are usually broken and thus the non-collinear AFMs can, in general, have an AHE.

For spin-conductivity, the transformation under time-reversal is precisely opposite because the spin current operator contains an additional spin operator which is odd under time-reversal. Thus for spin-conductivity, Eq. (1.10) is odd under time-reversal, while Eq. (1.11) is even. The spin-currents that are even under time-reversal are known as the SHE.

The odd spin-currents were previously considered only in FMs, however, as we will show in this manuscript they also exist in non-collinear AFMs (while in collinear AFMs they will typically be prohibited by the same symmetries as AHE), in complete analogy to the AHE. Since the intrinsic contribution to the spin currents in the triangular AFMs was recently explored in detail in [267], we focus here only on the spin-currents that are odd under time-reversal described by Eq. (1.10). To evaluate this equation, the ground state eigenvalues and eigenfunctions are needed, which we obtain from a non-collinear density functional theory calculation. We use the VASP code with the PBE-GGA exchange-correlation potential. To make the calculation faster we utilize the Wannier interpolation [55, 267].

Within linear response we can describe the spin current using a spin-conductivity tensor σ_{jk}^i , such that $\sum_k \sigma_{jk}^i E_k$ is the spin current with spin-polarization along i and flowing in the direction j . By considering all the symmetry operations and how they transform the spin-conductivity tensor [81, 182, 212] we find that the odd spin currents are indeed allowed by symmetry in the Mn_3X compounds. Note that this symmetry analysis is not related to the constant Γ approximation, but applies generally for any linear response. In Table 5.1 we give the general form of the odd spin-conductivity tensors for Mn_3Sn and Mn_3Ir . These symmetry tensors presume the existence of SOC. We find that the spin currents in the triangular AFMs appear even without the SOC (note that this is also true for the SHE in Mn_3Sn [268]). In absence of the SOC, the symmetry is higher because spin is then not coupled to the lattice directly. The symmetry restricted shape of the odd spin-conductivity tensors in absence of SOC is also given in Table 5.1. These tensors can be derived by considering the combination of symmetries of the nonmagnetic lattice with pure spin rotations [12, 116] and are in good agreement with our calculations.

In Fig. 5.6(a),(b) we plot the dependence of the magnitude of the odd spin currents in Mn_3Sn and Mn_3Ir on Γ . As expected, for small Γ the odd spin currents are diverging as $1/\Gamma$. The magnitude of the SHE is often given in terms of the spin Hall angle, which is defined as $\frac{e}{\hbar} \frac{\sigma_{jk}^i}{\sigma_{kk}}$, where σ_{kk} is the conductivity [74]. Such quantity can be defined for any spin current. To distinguish it from the conventional spin Hall angle we call it the spin current angle (SCA). The SCA defined in this way is dimensionless. In Figs. 5.6(c),(d) we plot the SCA as a function of Γ for Mn_3Sn and Mn_3Ir . To evaluate the SCA we calculated the conductivity using Eq. (1.10). Since both the conductivity and the spin conductivity scale as $1/\Gamma$ for small Γ , the SCA is independent of Γ for small Γ . As can be seen in Fig. 5.6 we find that large spin currents are present even in absence of the SOC.

We can estimate the value of Γ by comparing the calculated conductivity with the experimental conductivity. For Mn_3Ir the experimental conductivity at 300 K is $2.5 \times$

		no SOC	SOC
Mn ₃ Sn	σ^x	$\begin{pmatrix} 0 & \sigma_{xy}^x & 0 \\ \sigma_{xy}^x & 0 & 0 \\ 0 & 0 & 0 \end{pmatrix}$	$\begin{pmatrix} 0 & \sigma_{xy}^x & 0 \\ \sigma_{yx}^x & 0 & 0 \\ 0 & 0 & 0 \end{pmatrix}$
	σ^y	$\begin{pmatrix} -\sigma_{xy}^x & 0 & 0 \\ 0 & \sigma_{xy}^x & 0 \\ 0 & 0 & 0 \end{pmatrix}$	$\begin{pmatrix} \sigma_{xx}^y & 0 & 0 \\ 0 & \sigma_{yy}^y & 0 \\ 0 & 0 & \sigma_{zz}^y \end{pmatrix}$
	σ^z	$\begin{pmatrix} 0 & 0 & 0 \\ 0 & 0 & 0 \\ 0 & 0 & 0 \end{pmatrix}$	$\begin{pmatrix} 0 & 0 & 0 \\ 0 & 0 & \sigma_{yz}^z \\ 0 & \sigma_{zy}^z & 0 \end{pmatrix}$
Mn ₃ Ir	σ^x	$\begin{pmatrix} \sigma_{xx}^x & 0 & 0 \\ 0 & -\frac{\sigma_{xx}^x}{2} & 0 \\ 0 & 0 & -\frac{\sigma_{xx}^x}{2} \end{pmatrix}$	$\begin{pmatrix} \sigma_{xx}^x & \sigma_{xy}^x & \sigma_{xy}^x \\ \sigma_{yx}^x & \sigma_{yy}^x & \sigma_{yz}^x \\ \sigma_{yx}^x & \sigma_{yz}^x & \sigma_{yy}^x \end{pmatrix}$
	σ^y	$\begin{pmatrix} -\frac{\sigma_{xx}^x}{2} & 0 & 0 \\ 0 & \sigma_{xx}^x & 0 \\ 0 & 0 & -\frac{\sigma_{xx}^x}{2} \end{pmatrix}$	$\begin{pmatrix} \sigma_{yy}^x & \sigma_{yx}^x & \sigma_{yz}^x \\ \sigma_{xy}^x & \sigma_{xx}^x & \sigma_{xy}^x \\ \sigma_{yz}^x & \sigma_{yx}^x & \sigma_{yy}^x \end{pmatrix}$
	σ^z	$\begin{pmatrix} -\frac{\sigma_{xx}^x}{2} & 0 & 0 \\ 0 & -\frac{\sigma_{xx}^x}{2} & 0 \\ 0 & 0 & \sigma_{xx}^x \end{pmatrix}$	$\begin{pmatrix} \sigma_{yy}^x & \sigma_{yz}^x & \sigma_{yx}^x \\ \sigma_{yz}^x & \sigma_{yy}^x & \sigma_{yx}^x \\ \sigma_{xy}^x & \sigma_{xy}^x & \sigma_{xx}^x \end{pmatrix}$

Table 5.1: Symmetry restricted form of the odd spin-conductivity tensors in Mn₃Sn and Mn₃Ir with and without SOC. For Mn₃Ir the tensors are given in the coordinate system shown in Fig. 5.5(b). For Mn₃Sn we use a cartesian coordinate system related to the coordinate system in Fig. 5.5(a) in the following way: $\mathbf{x} = \mathbf{a}$, $\mathbf{y} = (\mathbf{a} + 2\mathbf{b})/\sqrt{3}$, $\mathbf{z} = \mathbf{c}$.

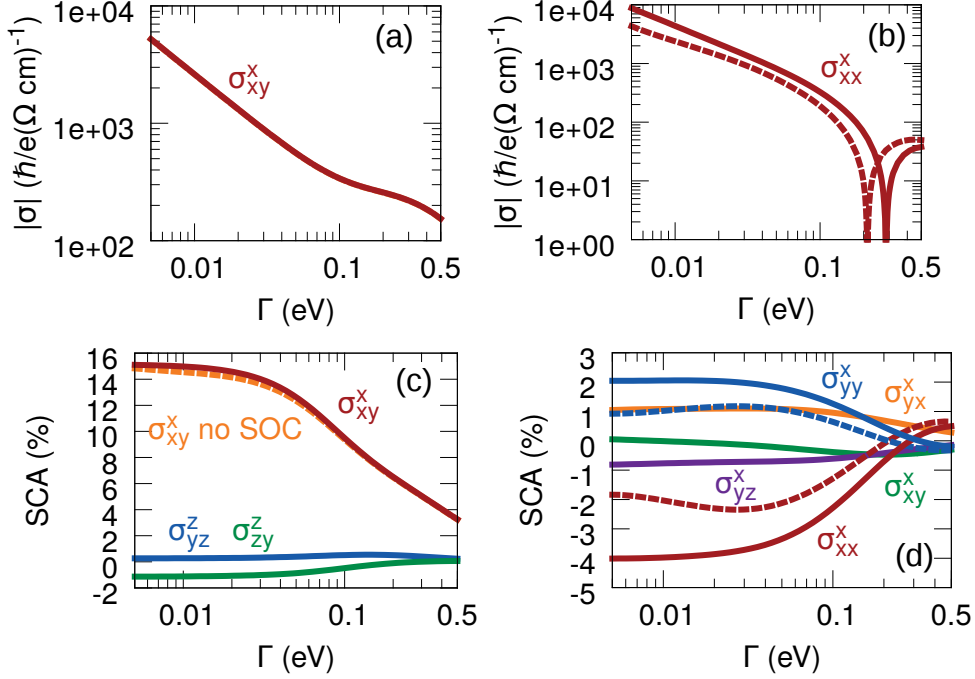


Figure 5.6: Γ dependence of the odd spin currents in Mn_3Sn and Mn_3Ir . (a),(b) The magnitude of the spin current for Mn_3Sn and Mn_3Ir respectively. Only the largest component is shown for clarity. The dashed line denotes a calculation without SOC. The dip in (b) corresponds to a sign change. (c), (d) The SCA for Mn_3Sn and Mn_3Ir respectively.

$10^4 (\Omega \cdot \text{cm})^{-1}$ [241]. This corresponds to $\Gamma \approx 0.05$ eV. For Mn_3Sn we find that even for very large values of Γ (up to 0.5 eV), the calculated conductivity is smaller than the experimental conductivity. This is probably because real crystals contain a significant amount of disorder, which cannot be captured by the constant Γ approximation.

For comparison, we calculated the odd spin currents in bcc Fe using the same method. We find that within the constant Γ approximation the longitudinal SCA in Fe is $\sim 18\%$ and the transverse SCA is $\sim 1\%$. Note that such a calculation is only a rough estimate because the spin-dependent scattering is very important in FMs.

Both Mn_3Sn and Mn_3Ir are not fully compensated, but have a small magnetic moment. Since this magnetic moment is very small, it cannot explain the odd spin currents discussed here. This is confirmed by calculation for Mn_3Ir in which the net magnetic moment is set to zero.

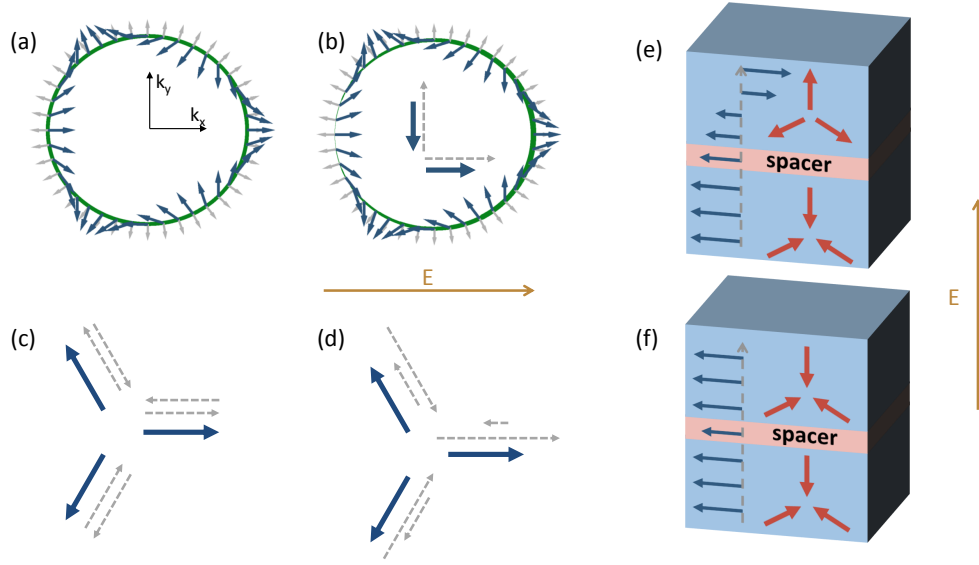


Figure 5.7: (a) Simplified Fermi level of a non-collinear AFM. Green line denotes the Fermi level, blue and gray arrows denote the mean values of spin and velocity respectively. (b) Electric field causes a redistribution of electrons at the Fermi level, signified by thicker or thinner green line. The arrows inside the circle show the corresponding spin currents. (c),(d) The main features of the Fermi level can be captured by considering only three types of electrons with velocities oriented parallel or antiparallel with their spin. (e),(f) Parallel and antiparallel states of the AFM junction. Gray dashed arrow denotes direction of the spin current flow, blue arrows denote the spin polarization of the spin current and red arrows denote the magnetic moments.

5.2.3 Discussion

The spin currents discussed here are similar to the spin-polarized currents in FMs, but they differ in some aspects. In FMs, in absence of SOC, spin is a good quantum number and the current can be decomposed into a spin-up and spin-down currents. This is the so-called two current model. Since the spin-up and spin-down electrons that carry the current have different properties (such as density, velocity or scattering rate), the spin-up and spin-down currents are different and the current is thus spin-polarized.

For non-collinear AFMs such description is not possible because in the presence of the non-collinear magnetic order, spin is not a good quantum number even without SOC. Therefore the electrons at the Fermi level can have spins oriented along various directions, as illustrated in Fig. 5.7(a). Since there is no net magnetic moment, the integral of the spin of all electrons is zero. The integral of spin times velocity also vanishes and thus there is no spin current in equilibrium. Upon applying an electric field, electrons at the

Fermi level are redistributed (see Fig. 5.7(b)). This results in a net current as well as a net spin current. The main features of the Fermi level depicted in Figs 5.7(a),(b) can be captured by considering only three types of electrons, as illustrated in Figs. 5.7(c),(d). It is then easy to verify that the redistribution of electrons results in both longitudinal and transverse spin current (the resulting spin currents are shown in Fig. 5.7(b)). In contrast, in FMs, in absence of SOC, the odd spin currents are only longitudinal.

We first focus on the longitudinal spin currents. These spin currents are analogous to the spin-polarized currents in FMs and will thus have similar implications. When a spin-polarized current is injected into an AFM it generates a STT which can efficiently manipulate the AFM order [29, 57, 62, 63]. Thus the STT will be present in a junction composed of two AFM layers separated by a thin metallic or insulating layer (see Figs. 5.7(e),(f)). Such heterostructure is analogous to the FM spin valve or MTJ. With large enough current, the STT could be used to switch the junction between a parallel and an antiparallel configuration. Analogously to the case of SHE and inverse SHE, there must also exist an inverse effect to the spin-polarized current: a charge current generated by injection of a spin-polarized current. This current will flow in the opposite direction when the spin-polarization of the spin-polarized current is reversed. The parallel and antiparallel configurations will thus have a different conductivity or equivalently different resistance, similarly to the GMR or TMR effect. The AFM junction is thus in principle analogous in functionality to the FM spin valve or MTJ, however, predicting the magnitude of the magnetoresistance and the torque is beyond the scope of this work.

It has been predicted by many authors that magnetoresistance and a STT will occur even in spin valves or tunneling junctions composed of collinear AFMs in which current is not spin-polarized [70, 71, 127, 130, 132, 150, 162, 175, 176, 194, 240]. These effects, however, rely on quantum coherence and perfect interfaces and were shown to be strongly suppressed by disorder [42, 130, 176]. The effects we have described here, on the other hand, do not rely on perfect interfaces and are expected to be similarly robust as the analogous effects in FMs since they rely only on the existence of the spin-polarized current. We also remark that the longitudinal spin currents can occur in nonmagnetic materials as well if the crystalline symmetry is low enough [228]. Such spin currents differ from the spin-polarized currents discussed here since they are even under time reversal and require SOC.

The transverse spin currents are similar to the spin currents due to the SHE, but differ in some key aspects. Because their origin is different they will depend differently on disorder and material properties such as SOC. Perhaps more importantly, the symmetry of the odd spin currents is distinct from the SHE. As a consequence, the odd spin currents can

have different spin-polarization than SHE, which could be important for the SOT [128]. Furthermore, since these spin currents are odd under time-reversal, they will tend to cancel out in samples with many magnetic domains. Recently several experiments have demonstrated a SOT in $\text{Mn}_3\text{Ir}/\text{FM}$ heterostructures [152,211,233,264]. While the origin of such a torque is not clear [152] it is known that in heavy metal/FM heterostructures, the SHE plays an important role [47,55]. Since our calculations show that the odd transverse spin currents are in Mn_3Ir larger than the intrinsic SHE (the intrinsic SHE in Mn_3Ir is $215 \hbar/e(\Omega \cdot \text{cm})^{-1}$ [267]), we expect them to also contribute to the SOT. Taking the odd spin currents into account could help towards a better understanding of the unexplained features of the SOT [152].

In conclusion, we have shown that novel spin currents occur in non-collinear AFMs and that as a consequence electrical current in these materials is spin-polarized. The spin-polarized current is analogous to the spin-polarized current in FMs and could be therefore utilized in the same way. This could have important implications for the field of AFM spintronics since several key spintronics phenomena are based on the existence of spin-polarized current. We show that—just like the AHE—the novel spin currents are a consequence of a symmetry breaking caused by the non-collinear magnetic structure. The conclusions we have made are quite general: the odd spin currents will be present in most magnetic materials except simple collinear AFMs.

6 Nonlinear electrical response: Berry curvature dipole

In this chapter, we study the Berry dipole induced nonlinear electrical response in both 3D WSM and 2D TI. WSM materials such as the TaAs-family pnictides [78, 222] and MoTe₂ [192, 198] have recently been discovered primarily by observation of the unique Fermi arcs of surface states through angle-resolved photoemission spectroscopy [39, 77, 85, 125, 239, 246]. Because Weyl points are monopole sources or drains of the Berry curvature of Bloch wave functions in momentum space, a WSM can exhibit an anomalous Hall effect when breaking the time-reversal symmetry (TRS) [16, 237, 245] or a spin Hall effect [199], as a linear response to an external electric field. Recent theoretical [?, 22, 23, 38, 76, 82, 139, 140, 171, 191, 202] and experimental [31, 126, 196, 230] studies have revealed giant nonlinear optical responses in inversion-symmetry-breaking WSMs, such as the photocurrent from the circular photogalvanic effect (CPGE), second harmonic generation (SHG), and nonlinear Hall effect. These nonlinear effects can be much stronger in WSMs than traditional electro-optic materials owing to the large Berry curvature [40, 138, 191].

Both types of WSMs exhibit a large BCD near the Weyl point that is orders of magnitude larger than that of conventional materials. As a Fermi surface property, the BCD favors tilted Weyl cones. Thus, the type-II WSM is usually superior to the type-I WSM. Further, we found that some small gap regions with highly concentrated Berry curvature can also contribute to a large dipole in the absence of Weyl points, similar to the enhancement of bulk photovoltaic effect in topological insulators [205]. We made an order-of-magnitude estimate of the nonlinear Hall effect for these materials, which is experimentally accessible.

It should be pointed out however that Weyl points require a genuinely 3D band dispersion - Weyl points cannot exist in 2D systems. Then it is also important to find the suitable 2D system that would serve as the platform for nonlinear anomalous Hall effect. In the following work, we show for the first time how a BCD in the band structure of a 2D material can be generated. We found that in 2D the critical point of the transition from

a TI to a normal insulator can induce a large BCD, which is in the spirit similar to the Weyl point in 3D. In the revised manuscript, we now make an explicit connection between the 3D Weyl physics and the 2D critical point, which is related to the observation that a Weyl node can in fact, be regarded as a 3D critical point.

To realize an experimental observation of the NLAHE, establishing the right material system to do so is the most critical issue. WTe₂ and MoTe₂ belong to a class of readily synthesizable layered materials. Originally highlighted for the presence of a semiconducting bandgap in exfoliated monolayers, they have recently been identified as promising topological materials and indeed as we show in our present work they do have a large BCD. Being already studied in transport experiments, 2D WTe₂ and MoTe₂ are thus ideal candidates for the experimental investigation of the nonlinear AHE. We believe this is an important message to the experimental community concerned with 2D materials.

6.1 Semiclassical Berry dipole and nonlinear anomalous Hall current

Very recently, the semiclassical approach has been used to describe the intraband contributions to CPGE and SHG as a Berry phase effect [40, 138] by a geometric quantity: the Berry curvature dipole (BCD) [191]. At the *dc* limit, the photocurrent remains finite as a transverse Hall-like current, i.e., a nonlinear Hall effect [191]. These nonlinear effects originate from the intraband resonant transitions at a low frequency in a noncentrosymmetric metal. Although they have played an important role in predicting topological materials and estimating their linear-response properties, there is still a lack of *ab initio* studies on the nonlinear optical effects of WSMs to quantitatively reveal the role of the Weyl points in realistic materials [230]. The nonlinear response is usually computed with mixed interband and intraband transitions for conventional semiconductors via Berry connection related formalism [187, 253], but an *ab initio* scheme with the Berry curvature dipole would be required to understand contribution from Weyl Fermions.

We first overview previous theoretical work on the nonlinear optical response described by the Berry curvature [40, 138, 140, 191]. For the CPGE, the oscillating electric field $E_c(t) = \text{Re}\{\mathcal{E}_c e^{i\omega t}\}$ of circularly polarized light induces a *dc* photocurrent $\mathbf{j}^{(0)}$ as a second-order nonlinear optical effect: $j_a^{(0)} = \chi_{abc} \mathcal{E}_b \mathcal{E}_c^*$. Similarly, the SHG is described by the second-harmonic current response $\mathbf{j}^{(2\omega)} e^{2i\omega t}$ to a linearly polarized light, where $j_a^{(2\omega)} = \chi_{abc} \mathcal{E}_b \mathcal{E}_c$. At the *dc* limit of a linearly polarized field, the nonlinear Hall effect is

characterized by a transverse current: $j_a = 2j_a^{(0)}|_{\omega \rightarrow 0} = 2\chi_{abb}|\mathcal{E}_b|^2$. For a material with TRS, the nonlinear response tensor σ has been theoretically obtained as a Berry phase effect [40, 138] and very recently further described by the BCD [191] as follows:

$$\chi_{abc} = -\varepsilon_{adc} \frac{e^3 \tau}{2\hbar^2(1 + i\omega\tau)} D_{bd} \quad (6.1)$$

$$D_{bd} = \int_k f_0 \frac{\partial \Omega_d}{\partial k_b}, \quad (6.2)$$

where D_{bd} is the BCD, Ω_d is the Berry curvature, f_0 is the equilibrium Fermi–Dirac distribution, τ refers to the relaxation time approximation in the Boltzmann equation, ε_{adc} stands for the third rank Levi–Civita symbol, and \hbar is the reduced Planck constant. D_{bd} is a Fermi surface effect that is intrinsic to the band structure and becomes dimensionless in three dimensions. We define the BCD density in the k -space as $d_{bd} \equiv f_0 \frac{\partial \Omega_d}{\partial k_b}$. Because d_{bd} is odd to the space inversion, D_{bd} vanishes when inversion symmetry appears. While they were obtained with the semiclassical theory, Eqs. 6.1 and 6.2 can also be derived by a fully quantum theoretical treatment with the Floquet formalism [140].

6.1.1 Simple effective model of Weyl points and corresponding Berry curvature dipole

Before visiting specific WSM materials, we investigated the BCD for a simple Weyl Hamiltonian to reach a qualitative but inspiring understanding:

$$H_{Weyl}(\mathbf{q}) = \hbar v_t q_t \sigma_0 + \hbar v_F \mathbf{q} \cdot \boldsymbol{\sigma}, \quad (6.3)$$

where \mathbf{q} is the momentum with respect to the Weyl point, $\boldsymbol{\sigma}$ is the Pauli matrix vector, v_F is the Fermi velocity of an isotropic Weyl cone without tilt, v_t represents the tilting velocity, and q_t is the tilting momentum along the \hat{t} direction. The tilt of the Weyl cone is characterized by the ratio $|v_t/v_F|$, where $|v_t/v_F| < 1$ stands for a type-I Weyl cone and $|v_t/v_F| > 1$ stands for a type-II one. Because the Berry curvature is $\Omega(\mathbf{q}) = \frac{\mathbf{q}}{2q^3}$ for the lower cone, we can analytically obtain d_{xy} , for example, without loss of generality:

$$d_{xy} = \frac{\partial \Omega_y}{\partial q_x} = \frac{3q_x q_y}{2q^5}. \quad (6.4)$$

We note that Ω and d_{xy} are independent of the tilt and reverse sign for the upper cone. However, the shape of the Fermi surface is sensitive to the tilt.

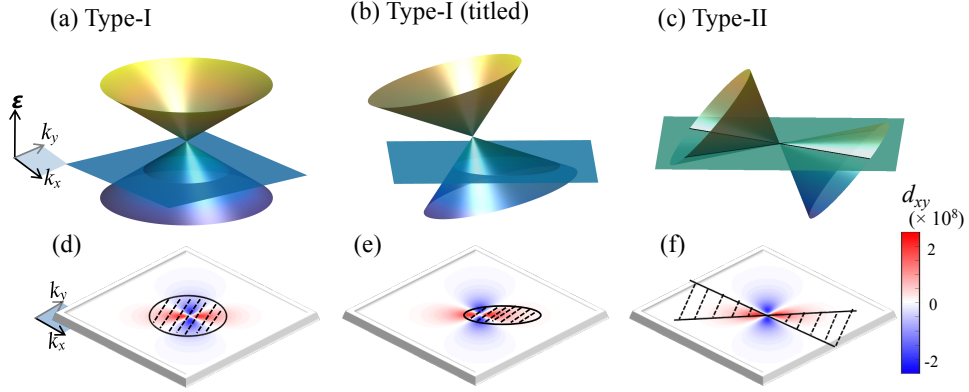


Figure 6.1: The Weyl cones and the dipole moment distribution of the Berry curvature. (a) A standard type-I Weyl cone without tilting. The Fermi energy is indicated by the horizontal plane and the Fermi surface is a circle. The corresponding dipole moment of the Berry curvature is shown in (d) near the Weyl point. (b) A type-I Weyl cone with a slight tilting and corresponding dipole moment in (e). (c) A type-II Weyl cone with a strong tilting and corresponding dipole moment in (f). Near the Weyl point, the dipole moment exhibits a symmetric $k_x k_y$ -type distribution when the Fermi energy crosses a type-I Weyl point and thus, it is summed to be zero as integrating over the k -space. In (d) and (e), the circle with a shadow region indicates the unoccupied bands that do not contribute to the integral of the dipole moment. The blue and red colors show negative and positive values of the dipole moment. In (f), the shadowed regions stand for the unoccupied hole pocket and the occupied electron band, both of which are deducted from the integral of the dipole moment.

The d_{xy} exhibits xy -type symmetry near the Weyl point (Eq. 6.4), which resembles a “ d_{xy} -type” atomic wave function in real space. For a type-I WSM, D_{xy} diminishes when E_F crosses the Weyl point because the integral of d_{xy} leads to zero owing to the xy -type symmetry. This is fully consistent with the fact that D_{xy} vanishes as the Fermi surface shrinks to a point at the Weyl point. When E_F lies either below or above the Weyl point, the Fermi surface region is effectively subtracted from the sum over the lower cone. If the type-I Weyl cone has no tilt (see Fig. 6.1a), the Fermi surface is centered to the Weyl point. Thus, d_{xy} outside the Fermi surface region is still highly symmetric and summed up to be zero. If the type-I Weyl cone has a tilt along some arbitrary direction (see Fig. 6.1b), the Fermi surface center is shifted away from the Weyl point. Consequently, d_{xy} outside the Fermi surface region becomes asymmetric, which leads to a nonzero net D_{xy} . For a type-II Weyl cone (see Fig. 6.1c), the Fermi surface naturally breaks the xy -type symmetries of d_{xy} and thus presents a nonzero D_{xy} . We can simply summarize these optimal conditions for a large D_{xy} near a single Weyl point: (i) For a type-I Weyl point, a tilt is necessary, which is common for WSM materials. Because d_{xy} is highly concentrated near the Weyl point, E_F should stay close enough to the Weyl point. (ii) The type-II Weyl point may exhibit large D_{xy} , even when E_F crosses it. Although the large tilt of Weyl points was also predicted to generate photocurrents by Chan et al. [22], they referred to the resonant transition between occupied and empty bands of the Weyl cone, which is different from the current finding in the low-frequency intraband transition.

Further, we point out that a pair of Weyl points that are the \mathcal{M}_x , \mathcal{M}_y or TRS partners contribute the same D_{xy} because $d_{xy} = d\Omega_y/dq_x$ is even to \mathcal{M}_x , \mathcal{M}_y or TRS. Therefore, multiple Weyl points related to TRS and mirror symmetries multiply their contributions to the BCD instead of compensating for each other.

6.2 Ab initio calculation of Berry dipole in TaAs and NbP

We performed *ab initio* density-functional theory (DFT) calculations for the bulk materials and projected Bloch wave functions to atomic-like local Wannier functions with the full-potential local-orbital (FPLO) program [102] within the generalized gradient approximation (GGA) [160]. For a material, we obtained the tight-binding Hamiltonian \hat{H} . Note that \hat{H} inherits exactly all symmetries of the system, which is crucial for accurate evaluation of the BCD from the Berry curvature Ω in a differential manner. (For the integrals of D_{xy} , the first Brillouzone was sampled by k -grids from $200 \times 200 \times 200$ to $1000 \times 1000 \times 1000$. Satisfactory convergence was achieved for a k -grid of $800 \times 800 \times 800$ for all compounds.

Increasing the grid size to $1000 \times 1000 \times 1000$ only varies the D_{xy} value by no more than 5%.)

The Berry curvature [234] of the n th band can be calculated according to \hat{H} :

$$\Omega_a^n(\mathbf{k}) = \varepsilon_{abc} 2i \sum_{m \neq n} \frac{\langle n | \partial_{k_b} \hat{H} | m \rangle \langle m | \partial_{k_c} \hat{H} | n \rangle}{(\epsilon_n - \epsilon_m)^2}, \quad (6.5)$$

where ϵ_n and $|n\rangle$ are eigenvalues and eigen wave functions, respectively, of \hat{H} at the momentum \mathbf{k} . Ω_a^n runs over occupied bands in Eq. 6.2, where $\Omega_d = \sum_n \Omega_d^n$.

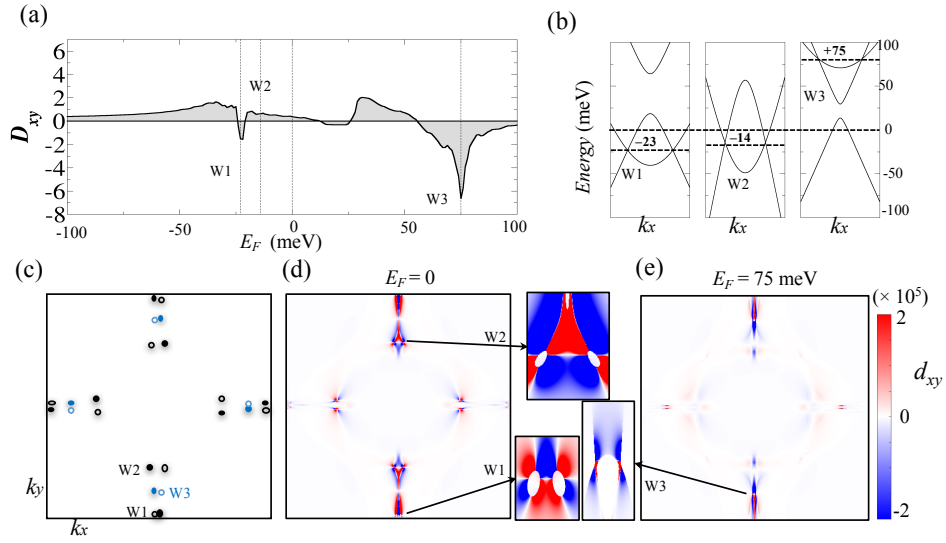


Figure 6.2: Calculated Berry curvature dipole D_{xy} for TaAs. (a) The Fermi energy (E_F) dependence of D_{xy} . $E_F = 0$ corresponds to the charge neutral point. (b) The band dispersions crossing a pair of Weyl points. Three types of Weyl points, W1, W2 and W3, are shown. (c) The projection of three types of Weyl points to the $k_x k_y$ plane by integrating d_{xy} over k_z . The distribution of d_{xy} at (d) $E_F = 0$ and (e) $E_F = 75$ meV crossing W3. Red and blue represent positive and negative values of d_{xy} , respectively, in the arbitrary unit. As insets, d_{xy} distributions near some Weyl points are shown in the $k_x k_y$ plane without integrating the k_z direction. The full Brillouin zone projected to the $k_x k_y$ plane is shown here.

6.2.1 Result of realistic materials

We investigated two representative families of materials with inversion symmetry breaking: (Ta, Nb)(As, P) as type-I WSMs and (Mo, W)Te₂ as type-II WSMs. For a given material,

the BCD tensor D_{ab} shape can be analyzed by considering the corresponding point group symmetry [191]. For instance, TaAs-type compounds belong to the C_{4v} point group, where \mathcal{M}_x and \mathcal{M}_y reflection symmetries exist. Because Ω_x and k_x are even and odd, respectively, to \mathcal{M}_x , d_{xx} is odd to \mathcal{M}_x , so $D_{xx} = 0$. Similarly, $D_{yy} = D_{zz} = 0$. Because Ω_z and k_x are odd and even, respectively, to \mathcal{M}_y , d_{xz} is odd to \mathcal{M}_y , so $D_{xz} = 0$. Likewise, we obtain only two nonzero tensor elements D_{xy} and D_{yx} , which follow $D_{xy} = -D_{yx}$. For (Mo, W)Te₂ in the C_{2v} point group, we obtain two nonzero independent tensor elements: D_{xy} and D_{yx} .

Because it is a Fermi surface property, the BCD relies on the Fermi energy in the band structure. As shown in Figs. 6.2a and b, D_{xy} of TaAs exhibit a sensitive dependence on the Fermi energy. Two groups of type-I Weyl points are known to exist owing to the crossings between the top valence and bottom conduction bands: four pairs of Weyl points, noted as W1 in the $k_z = 0$ plane; and eight pairs of Weyl points, noted as W2 in the $k_z \approx \pi/c$ plane (c is the lattice parameter along the z axis). W1 and W2 lie 23 and 14 meV, respectively, below the charge neutral point ($E_F = 0$) (see Fig. 6.2b). This is consistent with previous calculations and experimental measurements [3]. D_{xy} shows a peak in magnitude when E_F is close to W1, while it reverses the sign without a clear peak when E_F approaches W2. Although D_{xy} is zero as E_F exactly meets the Weyl point, the induced small D_{xy} region can be very narrow compared to the energy sampling interval (0.1 meV in Fig. 6.2a). Thus, D_{xy} does not necessarily show an apparent dip of amplitude at W1 or W2. Because $E_F = 0$ is slightly away from the Weyl points, D_{xy} here is smaller in magnitude than those near W1 or W2. Fig. 6.2d plots d_{xy} projected to the $k_x k_y$ plane. It is clear that d_{xy} is mainly distributed in the W1 and W2 regions near the \mathcal{M}_x plane but not the \mathcal{M}_y mirror plane. The small gap regions near Weyl points also contribute large magnitudes for $|d_{xy}|$. Note that d_{xy} does not necessarily follow the C_4 rotational symmetry. When the vicinity of W1 or W2 is magnified, a roughly xy -like distribution and ellipse-like hollow region can be observed. Such a hollow region corresponds to the Fermi surface that surrounds a Weyl point. This is similar to the effective deduction of the Fermi surface of a tilted Weyl cone, as demonstrated in Fig. 6.1b. Another striking feature is the large peak of D_{xy} at $E_F = 75$ meV. At this energy, we actually observed eight pairs of new Weyl points (noted as W3) by the crossings between the lowest and second-lowest conduction bands (see Fig. 6.2b). The W3 Weyl points are located between W1 and W2 in the momentum space and belong to type-II, as revealed by their energy dispersions. The corresponding d_{xy} indeed presents hot spots near W3, similar to that shown in Fig. 6.1c. This further confirms that type-II Weyl points contribute a larger BCD than type-I Weyl points under similar material conditions.

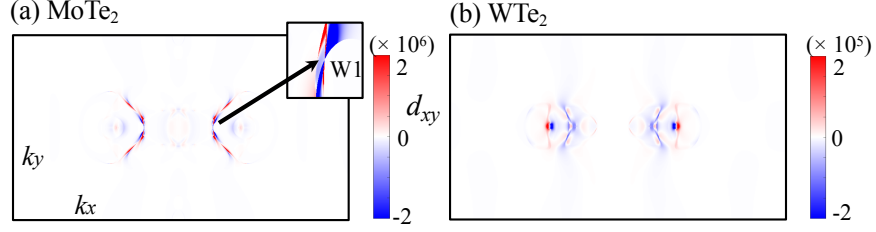


Figure 6.3: Berry curvature dipole for (a) MoTe₂ and (b) WTe₂ projected to the $k_x k_y$ plane for $E_F = 0$. The first Brillouin zone is shown in the $k_x k_y$ plane. A Weyl point region is magnified to demonstrate the type-II Weyl point feature. We point out that the scale of the color bar in (a) is one order of magnitude larger than that in (b).

We now turn to the type-II WSMs: MoTe₂ and WTe₂. In band structures, we obtained two pairs of type-II Weyl points for MoTe₂ and no Weyl point for WTe₂ between their conduction and valence bands, which is slightly different from the literature [192, 198]. This discrepancy is caused by the subtle difference between different DFT methods, as revealed in recent calculations [13, 217]. Here, WTe₂ serves an example of a non-WSM for the purpose of comparison to a WSM. For MoTe₂, we labeled the Weyl points as W1. For W1 points located nearly at $E_F = 0$, D_{xy} indeed shows a peak here. Near W1, the profile of d_{xy} looks like two crossing lines, which is a typical feature of the type-II Weyl point (see Fig. 6.3a). In contrast, WTe₂ exhibits a much smaller D_{xy} than MoTe₂. Although some hot spots of d_{xy} appear in Fig. 6.3b, they are less focused and one order of magnitude smaller than those of MoTe₂.

Table 6.1: The Berry curvature dipole calculated for Weyl semimetal materials. The Fermi energy is set to the charge neutral point. Only the nonzero tensor elements are listed for a given material, which are dimensionless.

Material	D_{xy}	Material	D_{xy}	D_{yx}
TaAs	0.39	MoTe ₂	0.849	-0.703
TaP	0.029	WTe ₂	0.048	-0.066
NbAs	-9.88			
NbP	20.06			

6.2.2 Discussion

Based on the results for TaAs, MoTe₂ and WTe₂, we verified these features of BCD as observed in simple models. Weyl points induce a large BCD, and type-II Weyl points usually contribute much more than type-I Weyl points. A WSM possibly exhibits a much stronger nonlinear response than an ordinary metal.

Furthermore, we reveal some new features of a BCD when all six compounds in Table I are compared. It is known that TaAs, TaP, NbAs, and NbP exhibit a decreasing order of spin-orbit coupling (SOC), which leads to a similarly decreasing order of the spin Hall effect [199]. However, D_{xy} does not follow the same order of SOC. NbAs and NbP show a much larger D_{xy} than other materials, including MoTe₂.

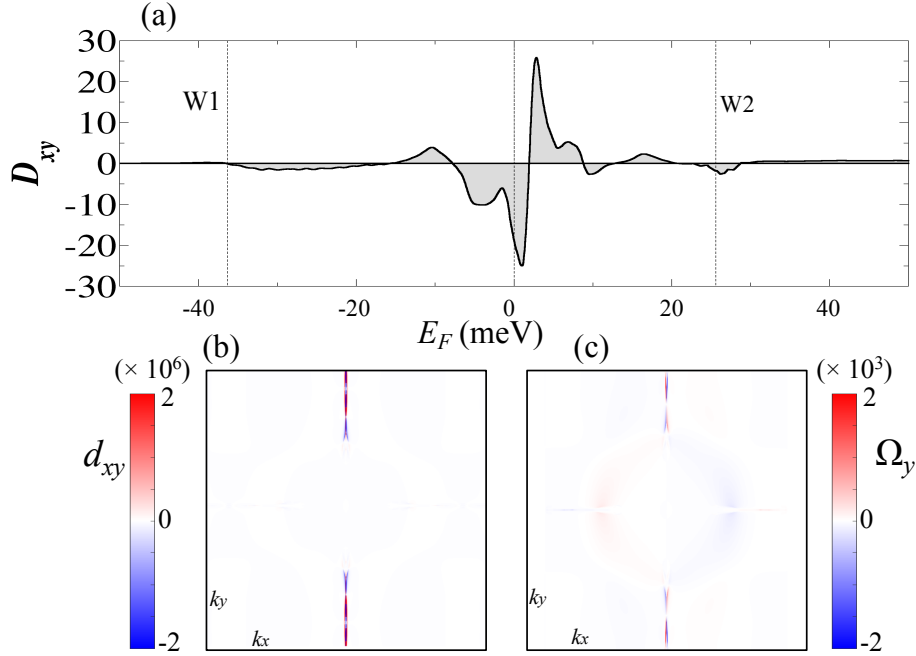


Figure 6.4: Berry curvature dipole for NbP for $E_F = 0$. (a) The energy dependent D_{xy} . W1 and W2 Weyl points lie below and above the charge neutral point, respectively, as indicated. (b) The d_{xy} and (c) Ω_y distributions at $E_F = 0$. Both are shown in arbitrary units.

Take NbP as an example. Its W1 Weyl points (36 meV below $E_F = 0$) present rather small D_{xy} because they are type-I with a weak tilt. In contrast, its W2 points (26 meV above $E_F = 0$) contribute a peak of D_{xy} , as shown in Fig. 6.4a, because they are type-II as revealed recently [232]. Although W1 and W2 still fit the above understanding about Weyl points, there are two large peaks of D_{xy} near $E_F = 0$ where only trivial Femi

pockets exist [101], which implies unusual D_{xy} contributions beyond Weyl points. We found that d_{xy} is dominantly distributed along the \mathcal{M}_x mirror plane (Fig. 6.4b). This can be rationalized by the distribution of the Berry curvature Ω_y . Ω_y is odd to \mathcal{M}_x and even to \mathcal{M}_y . Therefore, the Ω_y gradient along k_x , i.e., $d_{xy} = \partial\Omega_y/\partial k_x$, is large when crossing the \mathcal{M}_x plane. Further, Ω_y is more concentrated in a small region very close to the \mathcal{M}_x plane in NbP than in TaAs, which further enhances d_{xy} in NbP. Such a difference between NbP and TaAs originates from their band structures of SOC. At the limit of zero SOC, the valence and conduction bands each cross inside a mirror plane, which gives rise to a mirror symmetry protected nodal ring for the two systems. As the SOC increases, the nodal ring is gapped out. Consequently, the Berry curvature that caused by the entanglement between the valence and conduction bands has a more extended distribution in momentum space, as indicated by Eq. 6.5. Therefore, TaAs, with a stronger SOC, exhibits a much smaller BCD than NbP.

The sensitive Fermi surface dependence of the BCD serves as a way to effectively tune the nonlinear response in WSM materials. For example, both the carrier doping and external pressure are known to engineer the Fermi surface of these compounds (e.g., Refs. [7, 41, 44, 198, 217]). To enhance the BCD, it is favored that the material exhibits Weyl points and/or small energy gaps at the Fermi energy. The material with nodal lines in the absence of SOC may lead to Weyl points and small gap regions near these nodal lines when weak SOC is turned on without the inversion symmetry, presenting a large volume of BCD distribution near nodal lines (e.g. NbP). Such nodal lines usually required the protection of mirror planes in the material structure.

Finally, we developed a semi-quantitative estimation of the nonlinear response for these materials. According to Eq. 6.5, D_{xy} corresponds to χ_{zxx} and χ_{xxz} , and D_{yx} corresponds to χ_{zyy} and χ_{yyz} . We considered the nonlinear Hall effect, where the transverse Hall-like current $j_z = 2\chi_{zxx}\mathcal{E}_x^2$. The longitudinal current is $j_x = \sigma_{xx}\mathcal{E}_x$, and σ_{xx} is the ordinary conductivity. To characterize the strength of the nonlinear Hall effect, we can define the Hall angle as $\gamma = j_z/j_x = 2(\chi_{zxx}/\sigma_{xx})\mathcal{E}_x$. It is known that $\gamma \sim 10^{-3}$ for materials with the usual anomalous Hall effect (see Ref. [142] for a review). We assumed the relaxation time $\tau \sim 10$ ps and $\sigma_{xx} \sim 10^6 \Omega^{-1}\text{m}^{-1}$ based on recent low-temperature experiments (e.g., Refs. [4, 79, 165, 183, 262]) and an electric field $\mathcal{E}_x \sim 10^2$ V/m that is applicable for a physical property measurement system in a laboratory. Then, we obtained $\chi_{zxx} \sim 10^{-1}D_{xy}$ and $\gamma \sim 10^{-5} - 10^{-4}$ for D_{xy} in the range of TaAs, MoTe₂, NbAs and NbP. Because γ of the nonlinear Hall effect approaches 10% of that of anomalous Hall systems, the nonlinear Hall effect can be measurable for these WSM compounds.

6.3 Berry dipole in two dimensional two-dimensional transition-metal dichalcogenides WTe_2 and MoTe_2

In this section, We discuss the nonlinear electric response in WTe_2 and MoTe_2 monolayers. We reveal a strong NLAHE with a Hall-voltage that is quadratic with respect to the longitudinal current. The optimal current direction is normal to the mirror plane in these two-dimensional (2D) materials. The NLAHE can be sensitively tuned by an out-of-plane electric field, which induces a transition from a topological insulator to a normal insulator. Crossing the critical transition point, the magnitude of the NLAHE increases, and its sign is reversed. Our work paves the way to discover exotic nonlinear phenomena in inversion-symmetry-breaking 2D materials.

6.3.1 Introduction

The transition-metal dichalcogenides WTe_2 and MoTe_2 are WSMs in the 3D bulk [192, 198] and become two-dimensional (2D) TIs in the monolayer (ML) form [159, 166, 207, 231]. Nonlinear optical phenomena, for example, a nonlinear photocurrent, were recently reported in their bulk systems [84, 114]. In this work, we investigate the NLAHE in MLs of WTe_2 and MoTe_2 , because the use of MLs makes it easier to tune the band structure by an external electric field, for instance, by applying a back gate [231]. The out-of-plane electric field is found to sensitively tune the band structure and consequently control the BCD, which is an intrinsic property determined by the band structure and wave functions. Near the electric-field-induced topological transition from a TI to a normal insulator, the BCD and NLAHE are found to be strongly enhanced.

6.3.2 Response tensor in different structure

The WSM state of WTe_2 or MoTe_2 refers to the T_d phase of the crystal structure (space group $Pmn2_1$, No. 31), in which inversion symmetry is broken. However, the corresponding ML recovers the inversion symmetry by a slight distortion, commonly called the $1T'$ phase (space group $P2_1/m$, No. 11). This inversion symmetry can be broken by applying an out-of-plane electric field (E) or even by the existence of a substrate. We focus on the $1T'$ -MLs of the two compounds under different electric fields for two compounds. In addition, we also investigate the T_d -MLs for comparison, considering the fact that the phase transition may occur under special conditions (e.g. Refs [165, 244]). Both T_d - and

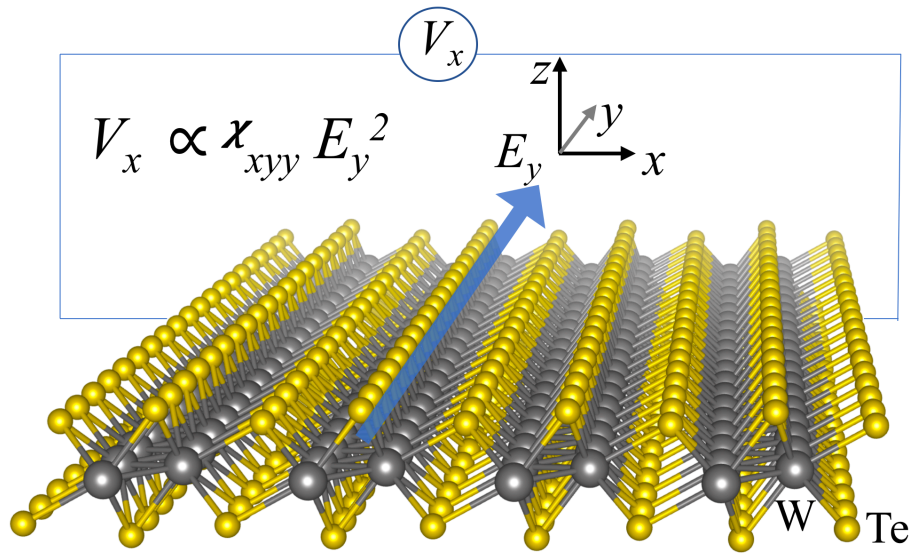


Figure 6.5: Crystal structure and the nonlinear anomalous Hall effect in the WTe_2 monolayer. W and Te atoms are represented by gray and yellow spheres. When applying an electric field along the y axis, i.e. the W chain direction that crosses the mirror plane, a Hall-like voltage V_x appears and is quadratic to the electric field E_y . Such a nonlinear anomalous Hall effect exists without breaking the time-reversal symmetry.

$1T'$ -MLs share a mirror plane $\mathcal{M}_y : y \rightarrow -y$. A zigzag-shape Mo or W atomic chain forms and crosses the mirror plane. The \mathcal{M}_y symmetry is crucial to determining the symmetry of the NLAHE as we will discuss. The BCD is dimensionless in three dimensions, whereas it is in the unit of length in 2D.

Because Ω_z^n is odd with respect to the \mathcal{M}_y reflection, $\frac{\partial \Omega_z^n}{\partial k_x}$ is odd to \mathcal{M}_y while only $\frac{\partial \Omega_z^n}{\partial k_y}$ is even. Therefore, only D_{yz} and χ_{xyy} are nonzero. Thus, the nonlinear Hall voltage V_x appears inside the mirror plane when an electric field E_y passes along the W or Mo chains, and $V_x \propto \chi_{xyy} E_y^2$, as illustrated in Fig. 6.5. If the voltage contacts and electric field directions are switched, there will be no NLAHE signal. This strong anisotropy can serve as a useful tool to distinguish the NLAHE from other effects in WTe_2 and MoTe_2 MLs.

$1T'$ Monolayers of WTe_2

We start with the $1T'$ -ML of WTe_2 . It is known to be a 2D TI. An applied electric field breaks the inversion symmetry and induces a transition from a TI to a trivial insulator. During the transition, the band gap first shrinks to zero and then opens again. A previous study on the TaAs-family of WSMs [266] revealed that the small gap or zero gap region contributes a large gradient of the Berry curvature, i.e, a large BCD. This can be intuitively understood from Eq. 6.5. The smallness of the energy gap (i.e, the denominator of Eq. 6.5) usually indicates that a large Berry curvature is concentrated on the small gap region, which is usually a narrow momentum area, leading to a large gradient of the Berry curvature. In addition to a large magnitude of the BCD, a sign change of the BCD may be induced by the phase transition, because the band inversion switches the sign of the Berry curvature. Therefore, we are particularly interested in the evolution of the BCD with respect to the topological phase transition.

Fig. 6.6 shows the band structures of the $1T'$ -ML under various electric fields. At $E = 0$, all the bands are doubly degenerate because of the coexistence of TRS and the inversion symmetry. The band structure exhibits direct band gaps with an inversion between the conduction and valence bands, giving rise to the 2D TI phase. The zero indirect bandgap is due to the known DFT underestimation, whereas the quasiparticle energy correction can lift the indirect gap, as discussed in previous work [166]. Because this indirect gap underestimation does not sensitively affect the Berry curvature effect investigated here, for simplicity, we use the DFT band structures in this work. As E increases, we indeed observe that the direct energy gap shrinks to zero at $E = 0.0075 \text{ V}/a_0$ (a_0 is the Bohr

radius, 0.53 Å) and opens again, inducing the topological transition. We note that the band touching point at the critical electric field is not equivalent to a Weyl point, since it is not stable against a weak perturbation (e.g. the variation of E) and the Weyl point is well-defined only for 1D and 3D systems. The Z_2 topological invariant before and after the transition is verified by tracing the Wannier centres by the Wilson loop method [193,254].

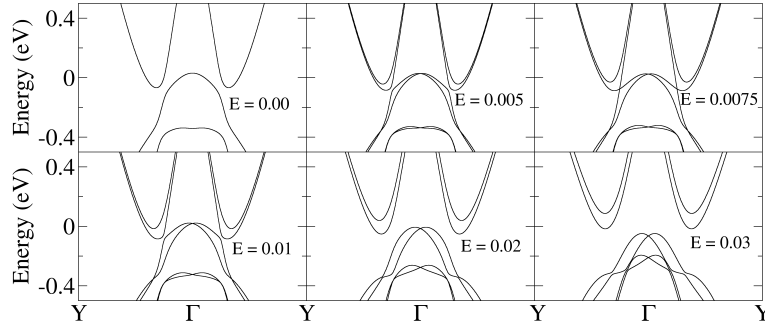


Figure 6.6: Band structures of WTe_2 $1T'$ -monolayers with applied electric field. The electric field E is out-of-plane and in unit of eV/a_0 , where a_0 is the Bohr radius. The band dispersion is shown along the Γ -Y direction, i.e. along the zigzag W chain.

We show the corresponding BCD in Fig. 6.7. At $E = 0$, the BCD vanishes regardless of position of the Fermi energy (E_F), because the coexistence of TRS and inversion symmetry forces $\Omega(\mathbf{k}) = 0$ at every momentum \mathbf{k} . At $E = 0.005$ V/ a_0 (the TI phase), a large BCD appears (Fig. 6.7a). Because it is a Fermi surface property, the BCD depends sensitively on the position of E_F . We focus on the BCD for $E_F = 0$, i.e. the charge neutral point. As E increases from zero, the BCD varies nonmonotonically and is characterized by four regimes. It (i) first increases in a positive amplitude (e.g. $E = 0.005$) V/ a_0 , (ii) then reduces to zero (near $E = 0.0075$ V/ a_0), (iii) further grows with a negative amplitude (e.g. $E = 0.01$ V/ a_0), and (iv) finally decreases to zero at large E ($E > 0.03$ V/ a_0). The regime-(i) is caused by the emergence of nonzero BCD by breaking the inversion symmetry with E . Because the phase transition switches the order of the conduction and valence bands, the sign of the Berry curvature is reversed by the transition, and thus the sign of the BCD is also reversed for regimes-(ii) and (iii). This behavior is quite similar to the sign change of the photocurrent calculated at the topological phase transition of TIs [205]. At large E , the system becomes a gapped insulator; thus, the Fermi surface vanishes at $E_F = 0$ and the BCS then becomes zero. This behavior explains the regime-(iv). For

$E = 0.005 \text{ V}/a_0$ and $0.01 \text{ V}/a_0$, one can find a peak of BCD slightly below $E_F = 0$ in Fig. 6.7. This is because of the smallest energy-gap (the largest Berry curvature) appears slightly below $E_F = 0$.

When the BCD is projected to 2D k -space, it is easier to understand the BCD from the corresponding band structure. For example, at $E = 0.005 \text{ V}/a_0$ the BCD is predominantly contributed by the small-gap region, for example, the nearly band touching positions along the Γ -Y line. After the band inversion at $E = 0.01 \text{ V}/a_0$, the BCD indeed changes sign. As E increases further to $E = 0.02 \text{ V}/a_0$ and $E = 0.03 \text{ V}/a_0$, the BCD decreases exponentially in amplitude, corresponding to regime-(iv) discussed above.

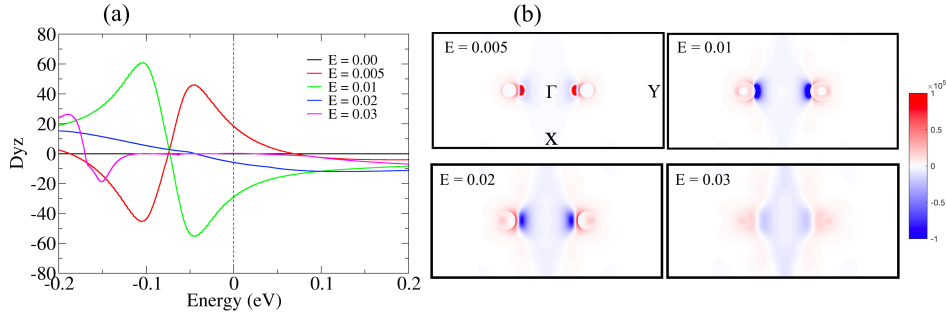


Figure 6.7: The Berry curvature dipole at different Fermi energy and its distribution in the 2D Brillouin zone for WTe_2 $1T'$ -monolayers with varying applied electric field. The Berry curvature dipole is in the unit of a_0 , where a_0 is the Bohr radius 0.529 \AA . In the 2D Brillouin zone, red and blue colors present positive and negative amplitudes (in arbitrary units) of the Berry curvature dipole.

T_d Monolayers of WTe_2

The T_d -ML breaks inversion symmetry. We can divide the effect of inversion symmetry breaking into two parts, the in-plane distortion Δ_{\parallel} and the out-of-plane distortion Δ_{\perp} . The induced band splitting can be observed at the bottom of the conduction band (Fig. 6.8a). It is also a 2D TI in topology. When an electric field is applied along the Δ_{\perp} , the symmetry breaking can be further enhanced to be $\Delta_{\parallel} + E$. For example, both the conduction and valence bands split further as E increases from 0 to 0.05. As in the $1T'$ structure, E drives the system to the topological phase transition in the band structure. However, the critical field for the T_d phase (~ 0.10) is much larger than that for the $1T'$ phase. Therefore, the BCD increases monotonically from $E = 0$ to $E = 0.05 \text{ V}/a_0$, as shown in Fig. 6.8b. When

E is opposite to Δ_\perp , the effective out-of-plane inversion-symmetry-breaking is $\Delta_\perp - E$. As E increases in amplitude, the symmetry-breaking effect first decreases and then increase again. For example, the band splitting is partially suppressed for $E = -0.01 \text{ V}/a_0$ and is further enhanced for $E = -0.05 \text{ V}/a_0$. The BCD shows the same trend (see Fig. 6.8b).

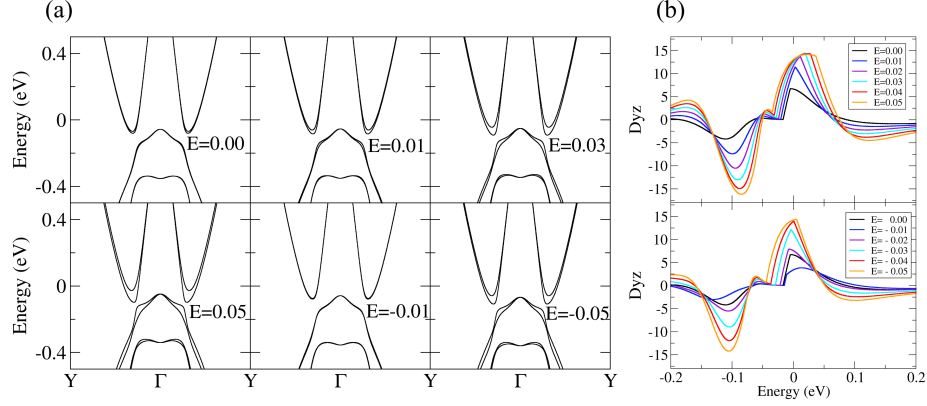


Figure 6.8: Band structures and the Berry curvature dipole (in unit of a_0) at different electric field (E in unit of V/a_0) for WTe_2 T_d -monolayers.

Monolayers of MoTe_2

The MoTe_2 MLs ($1T'$ and T_d) exhibit trends quite similar to those of WTe_2 MLs. For the $1T'$ structure, the topological phase transition occurs between $E = 0.01 \text{ V}/a_0$ and $E = 0.015 \text{ V}/a_0$. Therefore, the BCD exhibits large magnitudes with opposite signs under these two electric fields. When E increases further, the BCD decreases in amplitude, as shown in Fig. 6.9.

6.3.3 Discussion on magnitude

We estimate the magnitude of the NALHE. In a longitudinal dc field E_y , the nonlinear Hall $j_x = 2j_x^{(0)}|_{\omega \rightarrow 0} = 2\chi_{xyy}|\mathcal{E}_y|^2 = \sigma_{xy}E_y$, where we define a Hall conductance $\sigma_{xy} \equiv 2\chi_{xyy}E_y = \frac{e^3\tau}{h^2}D_{yz} = G_0(\tau D_{yz}eE_y\pi/\hbar)$ and $G_0 \equiv \frac{2e^2}{h}$ the conductance quantum. Considering $E_y \sim 10^3 \text{ V}/\text{m}$, $\tau \sim 1 \text{ ps}$ and $D_yz \sim 20a_0$ for $1T'$ WTe_2 , we obtain $\sigma_{xy} \sim 1\%G_0$. The magnitude of the NLAHE in MoTe_2 -MLs is comparable to that of WTe_2 , as indicated in Fig. 6.9. This Hall conductance can be measured under current experimental conditions.

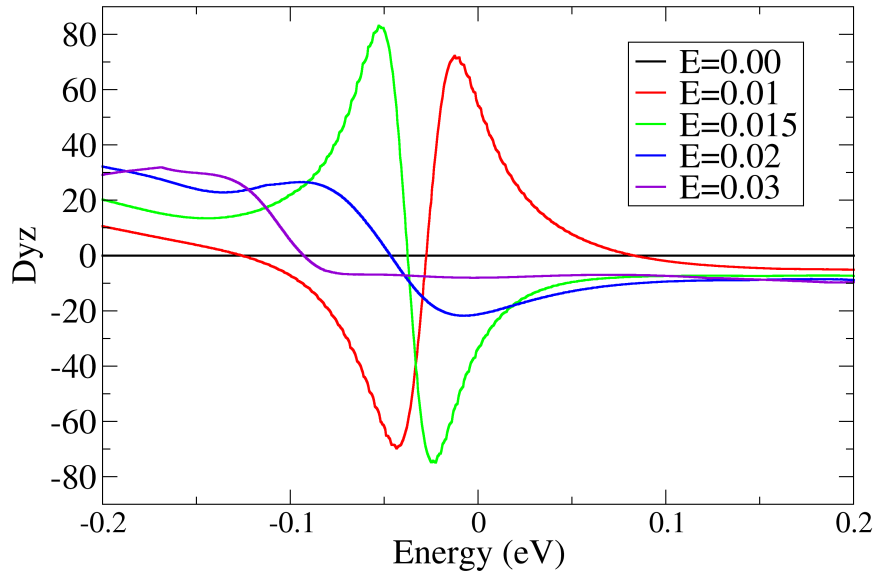


Figure 6.9: The Berry curvature dipole at different Fermi energy for MoTe₂ 1T'-monolayers with varying applied electric field.

6.3.4 Conclusions

In conclusion, we reveal a strong NLAHE in WTe₂ and MoTe₂ MLs. An out-of-plane external electric field can break the inversion symmetry (for the $1T'$ structure) and generate a nonzero BCD, leading to the NLAHE. Near the topological phase transition region induced by the electric field, the NLAHE is strongly enhanced. In addition to a dc electric field, a longitudinal (in-plane) electric field can also be the electric field of a low-frequency stimulation (e.g. a microwave), which may induce an even stronger NLAHE owing to the strong electric field. In addition to an out-of-plane electric field, the inversion symmetry of MLs can also be broken by other ways, such as the strain (e.g. recently realized in the MoS₂ ML [110]) and the substrate proximity. Note that our conclusions can be generalized from MLs to few layers and also to other phases (e.g. $2H$ and $1T$) of transition-metal dichalcogenides, when the inversion symmetry as well as the three-fold rotational symmetry is broken in these systems.

7 Nonlinear optical response

In the previous chapter, we study the nonlinear electrical effect which works at low-frequency and dc region. Now we would investigate the photogalvanic effect in the optical region both for the interband and intraband in the Weyl semimetal material TaAs. We find colossal photocurrents caused by the Weyl points in the band structure in a wide range of laser frequency. Our calculations reveal that the photocurrent is predominantly contributed by the three-band transition from the occupied Weyl band to the empty Weyl band via an intermediate band away from the Weyl cone, for excitations both by linearly and circularly polarized lights. Therefore, it is essential to sum over all three-band transitions by considering a full set of Bloch bands (both Weyl bands and trivial bands) in the first-principles band structure while it does not suffice to only consider the two-band direct transition within a Weyl cone. The calculated photoconductivity is well consistent with recent experimental measurements. Our work provides the first first-principles calculation on nonlinear optical phenomena of Weyl semimetals and serves as a deep understanding of the photogalvanic effects in complexed materials.

7.1 Introduction

Recent experiments [84, 114, 126, 155, 197, 230] have reported giant photocurrents effects and the second-harmonic generation (SHG) in the TaAs-family WSMs exhibiting in orders of magnitude larger responses than conventional nonlinear materials. However, the first-principles investigation on the photogalvanic effects of WSMs, which accounts for the realistic material band structures, is still missing. Moreover, some experiments are seemingly controversial to each other. Reference [126] reported a photocurrent caused by the circularly polarized light but claimed that a negligible photocurrent was caused by the linearly polarized light through the shift current mechanism. In contrast, Ref. [155] reported a colossal shift current with linearly polarized light in the same compound. Therefore, accurate estimations of photocurrents are necessary and timely to identify quantitative contributions from CPGE and shift current for a specific material. In addition, nonlinear

optical phenomena are highly sensitive to the bulk Fermi surface topology but are insensitive to surface states. Hence, they can serve a direct pathway to probe the topology inside the bulk.

In this work, we perform first-principles studies on the CPGE and shift current effect in WSMs. With the second-order Kubo formalism, we calculate the photocurrent conductivity in the inversion-asymmetric WSM TaAs via a multiband approach. Our results agree quantitatively with recent experiments. The shift current displays a close relation with the existence of WPs. Especially in the long-wavelength region, the shift current is predominantly contributed by virtual transitions from the occupied Weyl to the empty Weyl band through a third trivial band, referred to as the three-band transition, as illustrated in Fig. 7.1b. For CPGE, the three-band virtual transitions make the dominant contributions and distribute relatively uniform in the momentum space. In contrast, the two-band real transitions contribute much less photocurrent, which is mainly caused by the Weyl cone regions. Given the significance of the three-band transitions, it is necessary to sum over all intermediate states by considering a full set of Bloch states. Then the first-principles method is naturally the best way to compute the nonlinear response. For the same photon energy used in the experiment, we find that the CPGE photocurrent is nearly two orders of magnitude greater than the shift current and clarify the possible reason why the shift current was not detected in a previous experiment that reported the CPGE [126].

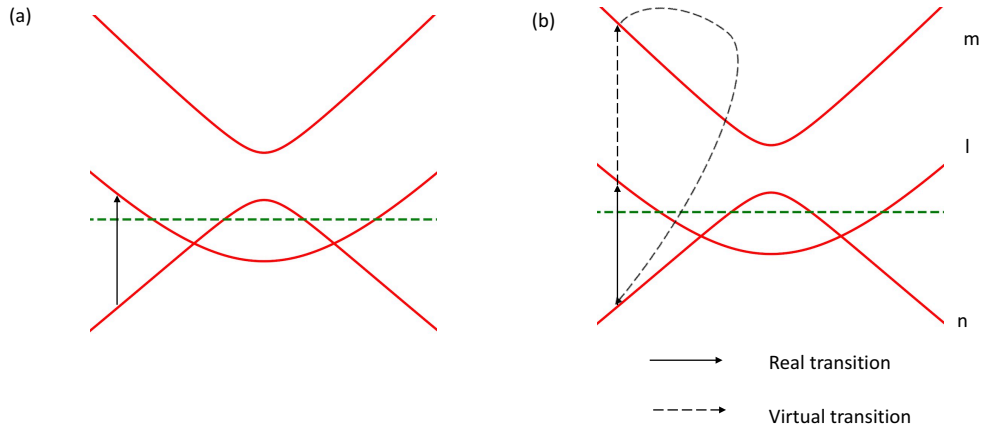


Figure 7.1: Optical process for bands with a pair of Weyl nodes of (a) absorption, (b) dc photocurrent.

7.2 Resonance theory

The calculation of CPGE and shift current is based on a quadratic response theory proposed by von Baltz and Kraut [103, 107, 213], which accounts for the steady-state short-circuit photocurrent under the linearly polarized light. To calculate the photocurrent also for the circularly polarized light, we have generalized this quadratic response theory to a more general relation for the photoconductivity:

$$\sigma_{ab}^c = \frac{|e|^3}{8\pi^3\omega^2} \text{Re} \left\{ \phi_{ab} \sum_{\Omega=\pm\omega} \sum_{l,m,n} \int_{BZ} d^3k (f_l - f_n) \right. \\ \left. \frac{\langle n\vec{k}|\hat{v}_a|l\vec{k} \rangle \langle l\vec{k}|\hat{v}_b|m\vec{k} \rangle \langle m\vec{k}|\hat{v}_c|n\vec{k} \rangle}{(E_n - E_m - i\delta)(E_n - E_l + \hbar\Omega - i\delta)} \right\}. \quad (7.1)$$

The conductivity (σ_{ab}^c ; $a, b, c = x, y, z$) is a third rank tensor and represents the photocurrent J^c generated by an electrical field \vec{E} via $J^c = \sigma_{ab}^c E_a^* E_b$. Here $\hat{v}_a = \frac{\hat{p}_a}{m_0}$, $E_n = E_n(\vec{k})$, and m_0 , $\delta = \hbar/\tau$, τ stand for, respectively, free electron mass, broadening parameter, and the quasiparticle lifetime. ϕ_{ab} is the phase difference between driving field \vec{E}_a and \vec{E}_b , i.e. $\phi_{yz} = i$ for left-circular polarized light propagating in x direction with light-polarization vector $(0, 1, i)$. It is clear that the real part of the integral in Eq. 7.3 describes the shift current response under linearly polarized light and the imaginary part of the integral gives the helicity dependent CPGE.

Next, we analyze the response tensor under time reversal symmetry (\hat{T}) and the point group symmetry. For simple, we define $N \equiv \langle n\vec{k}|\hat{v}_a|l\vec{k} \rangle \langle l\vec{k}|\hat{v}_b|m\vec{k} \rangle \langle m\vec{k}|\hat{v}_c|n\vec{k} \rangle$. \hat{T} reverses the velocity and brings an additional minus sign to the imaginary part of N by the complex conjugation. Thus, in materials with time reversal symmetry, the real part of the numerator is odd to \vec{k} and therefore vanishes in the integral, and hence, only the imaginary part of the numerator has to be taken into account for calculations on non-magnetic WSMs. Since there is no current from $l = n$ or $m = n$, we can separate the contribution into two parts with respect to band number l and m . The three-band processes ($n \rightarrow m \rightarrow l$) are given by $l \neq m$, and the two-band processes are given by $l = m$ (two-band transition). By applying the point group symmetry operations to the numerator N , the third rank conductivity tensor shape can be determined, as can be the tensor form of the anomalous Hall conductivity and spin Hall conductivity [257].

To see the relations between photocurrent response and the detailed band structure, we

analyze the energy denominator by decomposing it into real and imaginary parts:

$$\begin{aligned} D_1 &= \frac{1}{E_n - E_m - i\delta} = \frac{P}{E_n - E_m} + i\pi\delta(E_n - E_m), \\ D_2 &= \frac{1}{E_n - E_l + \hbar\Omega - i\delta} = \frac{P}{E_n - E_l + \hbar\Omega} + i\pi\delta(E_n - E_l + \hbar\Omega), \end{aligned} \quad (7.2)$$

Since the product of the three velocity matrices is purely imaginary, $Im(D_1 D_2)$ ($\sim \pi \frac{P}{(E_n - E_m)} \delta(E_n - E_l + \hbar\Omega)$) gives the shift current response when ϕ_{ab} is real. Only the momentum vector with band gap equal to photon energy ($|E_n - E_l| = \hbar\omega$) contributes to the response under the linearly polarized light. It indicates that the shift current distributes mainly in some selective small areas in the momentum space. When the incident photon energy is sufficiently small, the response current only comes from the gap between two Weyl bands due to the energy selection rule. In the $\delta = \hbar/\tau \rightarrow 0$ limit (long relaxation time limit, which is valid for semiconductors and insulators), the summation over band m can be performed analytically via the first-order perturbation correction of Bloch-wave function [213]. In the end, we obtain the shift vector formula for the shift current density [213, 252]. The shift vector directly connects the response photocurrent with a charge center shift between valance and conduction bands, but is quite numerically unstable for metallic system with a low-frequency driving field, due to the energy delta function and gauge fix of Berry connection of valance and conduction bands, and is not suited to deal with scattering processes with finite relaxation time. In a two-band approximation, the shift current response σ_{aa}^a ($a = x, y, z$) is zero as the velocity numerator N is real (here $l = m$, $N = \langle \vec{l}\vec{k} | \hat{v}_a | \vec{l}\vec{k} \rangle + \langle \vec{n}\vec{k} | \hat{v}_a | \vec{l}\vec{k} \rangle^2$), in which the velocity $v_a \equiv \langle \vec{l}\vec{k} | \hat{v}_a | \vec{l}\vec{k} \rangle$ is odd to \vec{k} due to the time reversal symmetry. Therefore, to calculate the shift current in real materials properly, one needs to use a multiband approach beyond the two-band approximation.

For circularly polarized light with helicity dependent term $\phi_{ab} = i$, the dispersive part $Re(D_1 D_2)$ ($\sim \frac{1}{(E_n - E_m)(E_n - E_l + \hbar\Omega)}$) (note relaxation time plays a minor role in CPGE) contributes to the response photocurrent. The absence of δ -function in $Re(D_1 D_2)$ indicates that there is no specific energy selection rule in the transition. Thus, in contrast to the concentrated distribution of the shift current, the CPGE distribution can be rather smeared out in momentum space. It also indicates that different transition pathways (real and virtual) contribute relatively equally to the photocurrent, assuming comparable numerators N . Given a large number of three-band virtual transitions, the virtual process might overwhelm the two-band direct process to induce the photocurrent.

To calculate the second-order photoconductivity in realistic compounds, we obtain

the density-functional theory (DFT) Bloch wave functions from the Full-Potential Local-Orbital program (FPLO) [102] within the generalized gradient approximation (GGA) [160]. By projecting the Bloch wave functions onto Wannier functions, we obtain a tight-binding Hamiltonian with 32 bands, which we use for efficient evaluation of the photocurrent. For the integrals of Eq. 7.3, the BZ was sampled by k -grids from $200 \times 200 \times 200$ to $960 \times 960 \times 960$. Satisfactory convergence was achieved for a k -grid of size $240 \times 240 \times 240$ for all three compounds. Increasing the grid size to $960 \times 960 \times 960$ varied the conductivity by less than 5%.

7.3 Result of TaAs

The material TaAs belongs to point group $4mm$ and has mirror reflections in x and y directions. Due to the mirror symmetries, the nonzero conductivity elements are limited to the ones with an even number of x and y , i.e. $\sigma_{xx}^z, \sigma_{yy}^z, \sigma_{zz}^z, \sigma_{zy}^y(\sigma_{yz}^y), \sigma_{zx}^x(\sigma_{xz}^x)$. In addition, the 4_2 screw rotation symmetry about z axis gives the relation $\sigma_{xx}^z = \sigma_{yy}^z, \sigma_{zy}^y = \sigma_{zx}^x$. Therefore, only three independent elements exist, i.e. $\sigma_{xx}^z, \sigma_{zy}^y$ and σ_{zz}^z . For the shift current, all three elements matter. For CPGE, only σ_{zy}^y is relevant.

Since the photocurrent response arises from both real and virtual band transitions, it generally has a strong dependence on the incident photon energy. As we are starting from a relaxation time approximation, the incident photon energy in our calculation should be above 5 meV (the typical relaxation time $\delta = \frac{\hbar}{\tau}$ for metallic system, we use $\delta = 10$ meV in our calculations). Thus, we focus on the mid-infrared region from 20 meV to 200 meV, which contains the transitions between Weyl bands. In TaAs, two groups of type-I Weyl nodes exist : (1) four pairs of WPs, noted as W_1 , on the $k_z = 0$ plane with energy -23 meV; (2) eight pairs of WPs, noted as W_2 , out of $k_z = 0$ plane with energy 14 meV. The shift current shown in Fig 7.2 has a strong peak at photon energy $\hbar\omega = 40$ meV, around twice of the energy of in-plane Weyl nodes, and is almost zero below the Weyl node energy scale in our calculation. This is explained by real transitions from band n to band l in Fig.7.1, photocurrent is nonzero only when $E_l(\vec{k}) > 0, E_n(\vec{k}) < 0, E_l(\vec{k}) - E_n(\vec{k}) = \hbar\omega$, and increase when $\hbar\omega$ is decreasing because of the $\frac{1}{\omega^2}$ in the prefactor of Eq.7.3.

For the photon energy dependence of CPGE, the $1/(\hbar\omega)^2$ behavior is observed in the region where our approach is valid. Since the energy denominator $Re(D_1 D_2)$ is the dispersive part of the second-order optical response, the complex integral is nearly unchanged in low-frequency regime, leading to a $1/(\hbar\omega)^2$ dependence due to the prefactor of Eq. 7.3

7.4 Effect of disorders and fluctuations.

Next, we discuss the effect of temperature and impurity scattering on the photocurrent generation. In our calculation, the effect of disorder and fluctuations are taken into account by the constant relaxation time τ , which is not considered in the shift vector formalism [187, 252]. Since the distribution of shift current in momentum space is quite concentrated around Weyl nodes, the constant relaxation time would lead to almost the same results compared with more realistic momentum dependent relaxation time. Another possible effect on the conductivities comes from the change in the electron distribution. However, since most of the experiments are carried out at low temperature ($k_B T = 4.3$ meV ($T = 50$ K)), which is comparable to δ and much smaller than the frequency of light, we expect the temperature change in the Fermi-Dirac distribution function does not modify the conductivity significantly.

Figure 7.3 show the chemical potential dependence of shift current and CPGE, calculated with different relaxation time. As shown in Fig. 7.3, both terms show only small dependence on the relaxation time. For shift current σ_{zz}^z , the response current is maximized when Fermi level is adjusted around the Weyl nodes energy, and change only by 20% even if the relaxation time is changed by a factor of 100. For the CPGE σ_{yz}^z curve, the response current is almost unchanged at the charge neutrality point, and does not show strong dependence on the Weyl nodes energy level.

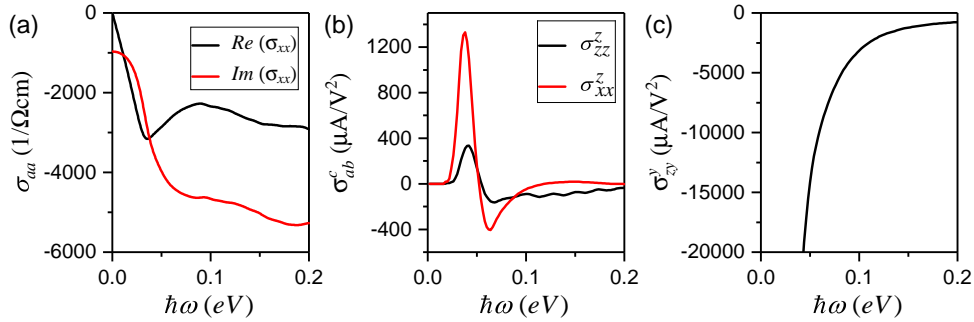


Figure 7.2: Photon energy dependence of (a) optical conductivity, (b) shift current conductivity under linearly polarized light, (c) circular photogalvanic conductivity.

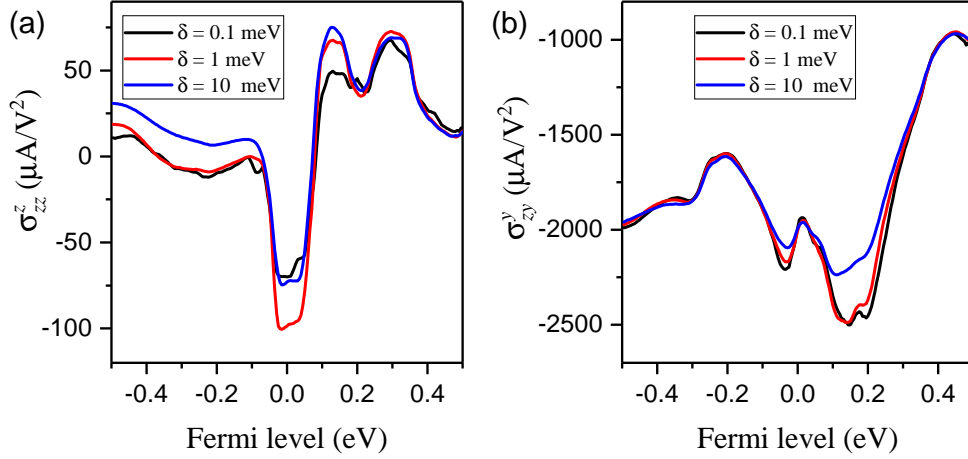


Figure 7.3: Fermi level dependence of (a) shift current and (b) circular photogalvanic conductivity at $\hbar\omega = 120$ meV. Each lines shows the results for different relaxation time.

7.5 Two- and three-band processes

For given valence band n and conduction band l , the CPGE and shift current should sum over the real transition ($n \rightarrow l$, $l = m$ in Eq. 7.3) and also the virtual transitions ($n \rightarrow m \rightarrow l$, $l \neq m$ in Eq. 7.3) for all third bands m . To understand the importance of virtual transitions, here we separate the two- and three-band process contributions for the response at incident photon energy $\hbar\omega = 120$ meV, to investigate which one is more essential in the photocurrent generation.

As shown in Fig. 7.4(a), the three-band part of CPGE σ_{zy}^y is $1825 \mu A/V^2$, while the two-band part is only $75 \mu A/V^2$ at the charge neutrality point. We obtain the $J_y = 1.2 \times 10^{-4}$ A with only two-band transitions in our method, which matches well with the theoretical calculated result 1.015×10^{-4} A in Ref. [126] via an effective two-band model.

Similarly, for the entire range of Fermi level we calculated, a large contribution to the photocurrent comes from the three-band processes. The distribution of three-band contribution for σ_{zy}^y is quite dispersed in momentum space, in contrast to the of the two-band part concentrating around WPs. In total magnitude, the two-band process is ten times smaller than the three-band process. Taking a closer look into the small area around W_1 WPs, the two-band part solely comes from $E_v(\vec{k}) - E_c(\vec{k}) = 120$ meV, which is the direct transition between two Weyl bands; while the three-band contribution stay almost uniformly in the momentum space, implying that virtual transitions have a larger contribution than the real transitions.

It should be stressed that the shift current σ_{zz}^z is purely a three-band process, as we have analyzed according to Eq. 1 and have also confirmed in numerical calculations. Therefore, it is necessary to include a third band for the evaluation of the photocurrent \vec{J} parallel to electric field \vec{E} . In the momentum space distribution of shift current σ_{zz}^z , the nonzero part is concentrated around the WPs, which shows the absorptive nature of shift current. Thus, we can conclude that shift current in Weyl system comes from the interplay of Weyl nodes and third trivial bands when the incident photon energy is at the same scale of the energy of Weyl nodes.

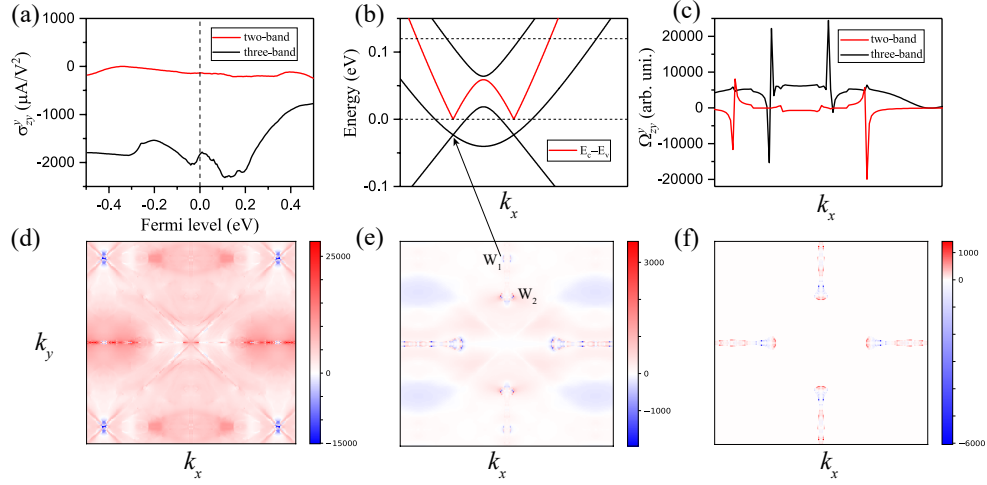


Figure 7.4: (a) Three-band and two-band part of the Fermi level dependent CPGE σ_{zy}^y at $\hbar\omega = 120$ meV, (b) Band structure in k_x direction across the w_1 Weyl node; (c) Three-band and two-band contribution of Ω_{zy}^y (CPGE σ_{zy}^y in momentum space) through the same k path as (b), blue curve is the band gap between valence and conduction band; (d) Three-band part of σ_{zy}^y (CPGE) in first Brillouin zone; (e) Two-band part of σ_{zy}^y (CPGE) in first Brillouin zone; (f) σ_{zz}^z (shift) in first Brillouin zone.

7.6 Discussion and comparison with experiments

We have systematically studied the photocurrent response both for linearly and circularly polarized lights in type-I WSM TaAs, and show that shift current spectrum has a strong dependence with Weyl points energy, while CPGE shows a $1/(\hbar\omega)^2$ behavior in mid-infrared regime, when the incident photon energy is larger than the smearing energy. Comparing our calculated results with recent photocurrent experiments, we observe that the CPGE experiment of TaAs [126] measured σ_{zy}^y (CPGE) with the incident photon

energy $\hbar\omega = 120$ meV. Our calculated σ_{zy}^y is $1900 \mu A/V^2$, gives a photocurrent $J_y = 2.1 \times 10^{-3} A$ under the experimental laser power. Taking into account a scaling factor 10^{-4} determined in experiment [126] and other unspecified decay channels, our results agree well with the experimental value of $40 \times 10^{-9} A$. The calculated shift current J_y is $8 \times 10^{-5} A$ in this setup (4% of the photocurrent from circularly polarized light), which may possibly explain why shift current was neglected in Ref. [126] that focused on the CPGE.

Recently the shift current was experimentally studied in TaAs [155] and σ_{xx}^z , σ_{zz}^z , and σ_{zx}^x were measured at photon energy $\hbar\omega = 117$ meV, which is at least an order of magnitude larger than previously measured materials (e.g. $\sigma_{zz}^z(shift) = 0.013 \mu A/V^2$ in BaTiO₃ with visible light [252, 261]). Our calculated $\sigma_{zx}^x(shift)$ is $79 \mu A/V^2$, in good agreement with the experimental result $\sigma_{zx}^x = 26 \mu A/V^2$.

Apart from the above fixed photon energy experiments, it would be interesting to investigate the frequency dependent photocurrent both for circularly and linearly polarized light, to verify the $1/(\hbar\omega)^2$ dependence of CPGE and the peak of shift current for $\hbar\omega$ being around twice of the WP (W_1) energy.

In addition, the calculated SH susceptibility χ_{zz}^z and the ratio of χ_{zx}^x/χ_{zz}^z are 6200 pm/V and 0.3 respectively, which are quite close to the measured value 7200 pm/V and 0.031 at low temperature [230]. Here we present the generalized formula for second harmonic generation (SHG):

$$\sigma_{ab}^c = \frac{|e|^3}{8\pi^3\omega^2} Re \left\{ \phi_{ab} \sum_{\Omega=\pm\omega} \sum_{l,m,n} \int_{BZ} d^3k (f_l - f_n) \right. \\ \left. \frac{\langle n\vec{k}|\hat{v}_a|l\vec{k} \rangle \langle l\vec{k}|\hat{v}_b|m\vec{k} \rangle \langle m\vec{k}|\hat{v}_c|n\vec{k} \rangle}{(E_n - E_m - 2\hbar\Omega - i\delta)(E_n - E_l + \hbar\Omega - i\delta)} \right\}. \quad (7.3)$$

The conductivity (σ_{ab}^c ; $a, b, c = x, y, z$) is a third rank tensor and represents the photocurrent J^c generated by an electrical field \vec{E} via $J^c = \sigma_{ab}^c E_a^* E_b$. And the second harmonic susceptibility is given by $\chi_{ab}^c = \sigma_{ab}^c / 2i\omega\epsilon_0$. Here $\hat{v}_a = \frac{\hat{p}}{m_0}$, $E_n = E_n(\vec{k})$, and m_0 , $\delta = \hbar/\tau$, τ , ϵ_0 stand for, respectively, free electron mass, broadening parameter, quasiparticle lifetime and vacuum permittivity. ϕ_{ab} is the phase difference between driving field \vec{E}_a and \vec{E}_b , i.e. $\phi_{yz} = i$ for left-circular polarized light propagating in x direction with light-polarization vector $(0, 1, i)$. The SHG has a similar behavior as the shift current, and we would analysis the photon energy dependent spectrum in future work.

7.7 Summary

In summary, we have developed a first-principles multiband approach to determine the photocurrent response from linearly and circularly polarized lights. We have established that the virtual transitions from Weyl bands to trivial bands play an essential role in the photocurrent generation process. In general, our method is also useful to study the nonlinear optical responses in ordinary metallic and insulating materials.

8 Summary

In this thesis, we have studied the linear response and nonlinear response in periodic solid systems with Kubo-based formalism and first-principle Wannier Hamiltonian. We derive and implement an effective formalism to describe charge current, spin current, and photocurrent response to an external electrical field, temperature gradient, and laser radiation. We focus on two aspects— linear response: anomalous Hall effect, spin Hall effect, spin Nernst effect, and spin-polarised charge current; nonlinear response: nonlinear Hall effect, Berry dipole, and photogalvanic effect under linearly and circularly polarised light. The target system is mainly topological materials with unconventional low-energy quasi-particles such as Dirac or Weyl points, and noncollinear coplanar antiferromagnets.

After introducing the numerical method, first, we overview WSMs. Besides the inversion-symmetry-breaking nonmagnetic WSM, Weyl fermion would also be realised in a magnetic system with broken TRS. We predict the fully compensated ferrimagnet Ti_2MnAl as a magnetic WSM, and noncollinear antiferromagnetic Mn_3X ($\text{X}=\text{Ga}, \text{Ge}, \text{Sn}, \text{Rh}, \text{Pt}, \text{Ir}$) as Weyl metals.

Second, we derive the linear response Kubo formula and obtain the Berry curvature representation for anomalous and spin Hall effects. Further, we extend the expression to describe the response to an external temperature gradient, i.e. the ANE and spin Nernst effect. We evaluate several types of materials for the charge and spin current generation. We determine that the SOC gapped nodal-line is a key contributor to spin current generation. Illustrating the example of TaAs and IrO_2 , we propose a p-band semimetal InBi as the ideal material for spin current generation, which has larger spin Hall angle and spin Nernst angle compared with Pt.

Finally, we extend the response formula to describe the second-order response, typically the nonlinear Hall effect from the Berry dipole. We observe that the Berry dipole is strongly concentrated around the Weyl points in the 3D WSM TaAs family and enhanced around the topological transition point in two-dimensional MoTe_2 and WTe_2 . To study the second-order response in the optical region, we develop the resonant Kubo-like nonlinear response formula-based approach for metallic systems. We analyse various types of electron

transitions (direct and indirect) in a TRS system and argue that, depending on the type of photoexcitation (linear or circularly polarised), the transition process that includes an intermediate band may have a dominant contribution to the nonlinear optical response for TaAs, which is in contrast with a previous two-band effective Weyl model-based study.

From these results, we observe that, although the quantum and classical response theory is well established, rich physics remains to be explored on its relation with band topology. The topological quasi-particles generally yield special and enhanced transport properties, especially in the nonlinear region, which would lead to broad applications of topological materials and pave the way for the detection of topological band structures via various transport measurements. This work has dealt with nonmagnetic materials with TRS for the nonlinear response region. It would be interesting to study the nonlinear response in a time-reversal-breaking system and detect the magnetic orientation using nonlinear signals in the future. Another promising direction is to study the transport properties of correlated topological systems and determine the direct response signatures.

Bibliography

- [1] ALI, M. N., GIBSON, Q. D., KLIMCZUK, T., AND CAVA, R. J. Noncentrosymmetric superconductor with a bulk three-dimensional Dirac cone gapped by strong spin-orbit coupling. *Phys. Rev. B* 89, 2 (Jan. 2014), 020505.
- [2] ANDERSON, P. W., AND HASEGAWA, H. Considerations on double exchange. *Phys. Rev.* 100 (Oct 1955), 675–681.
- [3] ARNOLD, F., NAUMANN, M., WU, S. C., SUN, Y., SCHMIDT, M., BORRMANN, H., FELSER, C., YAN, B., AND HASSINGER, E. Chiral Weyl Pockets and Fermi Surface Topology of the Weyl Semimetal TaAs. *Phys. Rev. Lett.* 117, 14 (2016), 146401.
- [4] ARNOLD, F., SHEKHAR, C., WU, S.-C., SUN, Y., DOS REIS, R. D., KUMAR, N., NAUMANN, M., AJEESH, M. O., SCHMIDT, M., GRUSHIN, A. G., BARDARSON, J. H., BAENITZ, M., SOKOLOV, D., BORRMANN, H., NICKLAS, M., FELSER, C., HASSINGER, E., AND YAN, B. Negative magnetoresistance without well-defined chirality in the Weyl semimetal TaP. *Nat. Commun.* 7 (May 2016), 11615.
- [5] BALTZ, V., MANCHON, A., TSOI, M., MORIYAMA, T., ONO, T., AND TSERKOVNYAK, Y. Antiferromagnetism: the next flagship magnetic order for spintronics? *arXiv preprint arXiv:1606.04284* (2016).
- [6] BAUER, G. E. W., SAITOH, E., AND WEES, B. J. v. Spin caloritronics. *Nature Materials* 11 (2012), 391.
- [7] BELOPOLSKI, I., SANCHEZ, D. S., ISHIDA, Y., PAN, X., YU, P., XU, S.-Y., CHANG, G., CHANG, T.-R., ZHENG, H., ALIDoust, N., BIAN, G., NEUPANE, M., HUANG, S.-M., LEE, C.-C., SONG, Y., BU, H., WANG, G., LI, S., EDA, G., JENG, H.-T., KONDO, T., LIN, H., LIU, Z., SONG, F., SHIN, S., AND HASAN, M. Z. Discovery of a new type of topological Weyl fermion semimetal state in $\text{Mo}_x\text{W}_{1-x}\text{Te}_2$. *Nat. Commun.* 7 (Dec. 2016), ncomms13643.

- [8] BERNEVIG, B. A., HUGHES, T. L., AND ZHANG, S.-C. Quantum spin hall effect and topological phase transition in HgTe quantum wells. *Science* *314*, 5806 (2006), 1757–1761.
- [9] BERNEVIG, B. A., AND ZHANG, S.-C. Intrinsic spin hall effect in the two-dimensional hole gas. *Physical Review Letters* *95* (2005), 016801.
- [10] BIAN, G., CHANG, T.-R., SANKAR, R., XU, S.-Y., ZHENG, H., NEUPERT, T., CHIU, C.-K., HUANG, S.-M., CHANG, G., BELOPOLSKI, I., SANCHEZ, D. S., NEUPANE, M., ALIDoust, N., LIU, C., WANG, B., LEE, C.-C., JENG, H.-T., ZHANG, C., YUAN, Z., JIA, S., BANSIL, A., CHOU, F., LIN, H., AND HASAN, M. Z. Topological nodal-line fermions in spin-orbit metal PbTaSe₂. *Nat. Commun.* *7* (2016), 10556.
- [11] BRADLYN, B., CANO, J., WANG, Z., VERGNIORY, M. G., FELSER, C., CAVA, R. J., AND BERNEVIG, B. A. Beyond Dirac and Weyl fermions: Unconventional quasiparticles in conventional crystals. *Science* *353*, 6299 (Aug. 2016), DOI: 10.1126/science.aaf5037.
- [12] BRINKMAN, W. F., AND ELLIOTT, R. J. Theory of Spin-Space Groups. *Proc. R. Soc. London, Ser. A* *294* (Oct 1966), 343–358.
- [13] BRUNO, F. Y., TAMAI, A., WU, Q. S., CUCCHI, I., BARRETEAU, C., DE LA TORRE, A., WALKER, S. M., RICCÒ, S., WANG, Z., KIM, T. K., HOESCH, M., SHI, M., PLUMB, N. C., GIANNINI, E., SOLUYANOV, A. A., AND BAUMBERGER, F. Observation of large topologically trivial Fermi arcs in the candidate type-II Weyl semimetal WTe₂. *Phys. Rev. B* *94*, 12 (Sept. 2016), 121112.
- [14] BRUNO, P., DUGAEV, V. K., AND TAILLEFUMIER, M. Topological Hall Effect and Berry Phase in Magnetic Nanostructures. *Phys. Rev. Lett.* *93*, 9 (Aug. 2004), 096806.
- [15] BUHL, P. M., FREIMUTH, F., BLÜGEL, S., AND MOKROUSOV, Y. Topological spin Hall effect in antiferromagnetic skyrmions. *arXiv:1701.03030* (2017).
- [16] BURKOV, A. A. Anomalous Hall Effect in Weyl Metals. *Phys. Rev. Lett.* *113*, 18 (2014).
- [17] BURKOV, A. A., AND BALENTS, L. Weyl Semimetal in a Topological Insulator Multilayer. *Phys. Rev. Lett.* *107*, 12 (Sept. 2011), 127205.

- [18] BURKOV, A. A., HOOK, M. D., AND BALENTS, L. Topological nodal semimetals. *Phys. Rev. B* *84*, 23 (Dec. 2011), 235126.
- [19] BZDUŠEK, T., WU, Q., RÜEGG, A., SIGRIST, M., AND SOLUYANOV, A. A. Nodal-chain metals. *Nature* *538*, 7623 (Aug. 2016), 75–78.
- [20] CHADOV, S., QI, X., KBLER, J., FECHER, G. H., FELSER, C., AND ZHANG, S. C. Tunable multifunctional topological insulators in ternary heusler compounds. *Nature Materials* *9* (2010), 541.
- [21] CHAN, C.-K., LEE, P. A., BURCH, K. S., HAN, J. H., AND RAN, Y. When chiral photons meet chiral fermions: photoinduced anomalous hall effects in weyl semimetals. *Physical review letters* *116*, 2 (2016), 026805.
- [22] CHAN, C.-K., LINDNER, N. H., REFAEL, G., AND LEE, P. A. Photocurrents in Weyl semimetals. *Phys. Rev. B* *95*, 4 (Jan. 2017), 041104.
- [23] CHAN, Y. H., CHIU, C.-K., CHOU, M. Y., AND SCHNYDER, A. P. Ca_3P_2 and other topological semimetals with line nodes and drumhead surface states. *Phys. Rev. B* *93*, 20 (May 2016), 205132.
- [24] CHANG, C., ZHANG, J., FENG, X., SHEN, J., ZHANG, Z., GUO, M., LI, K., OU, Y., WEI, P., WANG, L., JI, Z. Q., FENG, Y., JI, S., CHEN, X., JIA, J., DAI, X., FANG, Z., ZHANG, S. C., HE, K., WANG, Y., LU, L., MA, X. C., AND XUE, Q.-K. Experimental Observation of the Quantum Anomalous Hall Effect in a Magnetic Topological Insulator. *Science* *340*, 6129 (Apr. 2013), 167–170.
- [25] CHANG, T.-R., CHANG, G., LEE, C.-C., HUANG, S.-M., WANG, B., BIAN, G., ZHENG, H., SANCHEZ, D. S., BELOPOLSKI, I., ALIDOUST, N., NEUPANE, M., BANSIL, A., JENG, H.-T., XU, S.-Y., LIN, H., AND HASAN, M. Z. Prediction of an arc-tunable Weyl Fermion metallic state in Mo. *Nat. Commun.* *7* (Feb. 2016), 1–9.
- [26] CHEN, C., XU, X., JIANG, J., WU, S. C., QI, Y. P., YANG, L. X., WANG, M. X., SUN, Y., SCHRÖTER, N. B. M., YANG, H. F., SCHOOP, L. M., LV, Y. Y., ZHOU, J., CHEN, Y. B., YAO, S. H., LU, M. H., CHEN, Y. F., FELSER, C., YAN, B., LIU, Z. K., AND CHEN, Y. L. Dirac Line-nodes and Effect of Spin-orbit Coupling in Non-symmorphic Critical Semimetal MSiS ($\text{M}=\text{Hf}, \text{Zr}$). *arXiv:1701.06888* (Jan. 2017).

- [27] CHEN, H., NIU, Q., AND MACDONALD, A. H. Anomalous hall effect arising from noncollinear antiferromagnetism. *Phys. Rev. Lett.* *112* (Jan 2014), 017205.
- [28] CHEN, Y., XIE, Y., YANG, S. A., PAN, H., ZHANG, F., COHEN, M. L., AND ZHANG, S. Nanostructured Carbon Allotropes with Weyl-like Loops and Points. *Nano Lett.* *15*, 10 (Oct. 2015), 6974–6978.
- [29] CHENG, R., XIAO, J., NIU, Q., AND BRATAAS, A. Spin pumping and spin-transfer torques in antiferromagnets. *Phys. Rev. Lett.* *113* (2014), 057601.
- [30] CHENG, S.-G., XING, Y., SUN, Q.-F., AND XIE, X. Spin nernst effect and nernst effect in two-dimensional electron systems. *Physical Review B* *78*, 4 (2008), 045302.
- [31] CHI, S., LI, Z., XIE, Y., ZHAO, Y., WANG, Z., LI, L., YU, H., WANG, G., WENG, H., ZHANG, H., AND WANG, J. Ultra-broadband photodetection of Weyl semimetal TaAs up to infrared 10 μm range at room temperature. *arxiv* (May 2017).
- [32] CHIU, C.-K., AND SCHNYDER, A. P. Classification of reflection-symmetry-protected topological semimetals and nodal superconductors. *Phys. Rev. B* *90*, 20 (Nov. 2014), 205136.
- [33] CHIU, C.-K., TEO, J. C. Y., SCHNYDER, A. P., AND RYU, S. Classification of topological quantum matter with symmetries. *Rev. Mod. Phys.* *88*, 3 (Aug. 2016), 035005.
- [34] CHOI, T., LEE, S., CHOI, Y. J., KIRYUKHIN, V., AND CHEONG, S.-W. Switchable Ferroelectric Diode and Photovoltaic Effect in BiFeO₃. *Science* *324*, 5923 (Apr. 2009), 63–66.
- [35] COOPER, G., SAUNDERS, G., AND LAWSON, A. The electrical resistivity and thermoelectric power of InBi and In₂Bi. *Journal of Physics and Chemistry of Solids* *25*, 11 (1964), 1277–1278.
- [36] CRÉPIEUX, A., AND BRUNO, P. Theory of the anomalous hall effect from the kubo formula and the dirac equation. *Physical Review B* *64*, 1 (2001), 014416.
- [37] DE GENNES, P. G. Effects of double exchange in magnetic crystals. *Phys. Rev.* *118* (Apr 1960), 141–154.

- [38] DE JUAN, F., GRUSHIN, A. G., MORIMOTO, T., AND MOORE, J. E. Quantized circular photogalvanic effect in Weyl semimetals. *Nat. Commun.* 8 (July 2017), ncomms15995.
- [39] DENG, K., WAN, G., DENG, P., ZHANG, K., DING, S., WANG, E., YAN, M., HUANG, H., ZHANG, H., XU, Z., DENLINGER, J., FEDOROV, A., YANG, H., DUAN, W., YAO, H., WU, Y., FAN, S., ZHANG, H., CHEN, X., AND ZHOU, S. Experimental observation of topological Fermi arcs in type-II Weyl semimetal MoTe₂. *Nat. Phys.* 12 (Sept. 2016), 1105–1110.
- [40] DEYO, E., GOLUB, L. E., IVCHENKO, E. L., AND SPIVAK, B. Semiclassical theory of the photogalvanic effect in non-centrosymmetric systems. *arxiv* (Apr. 2009).
- [41] DOS REIS, R. D., WU, S. C., SUN, Y., AJEESH, M. O., SHEKHAR, C., SCHMIDT, M., FELSER, C., YAN, B., AND NICKLAS, M. Pressure tuning the Fermi surface topology of the Weyl semimetal NbP. *Phys. Rev. B* 93, 20 (May 2016), 205102.
- [42] DUINE, R. A., HANEY, P. M., NÚÑEZ, A., AND MACDONALD, A. Inelastic scattering in ferromagnetic and antiferromagnetic spin valves. *Phys. Rev. B* 75 (2007), 014433.
- [43] EERENSTEIN, W., MATHUR, N. D., AND SCOTT, J. F. Multiferroic and magnetoelectric materials. *Nature* 442 (Aug 2006), 759–765.
- [44] EINAGA, M., SHIMIZU, K., HU, J., MAO, Z. Q., AND POLITANO, A. Resistivity of Weyl semimetals NbP and TaP under pressure. *Phys. Status Solidi RRL* 11, 8 (Aug. 2017), 1700182.
- [45] EKAHANA, S. A., WU, S.-C., JIANG, J., OKAWA, K., PRABHAKARAN, D., HUANG, C.-C., MO, S.-K., SASAGAWA, T., FELSER, C., YAN, B., LIU, Z., AND CHEN, Y. Observation of nodal line in non-symmorphic topological semimetal inbi. *New J. Phys.* 19 (2017), 065007.
- [46] FAN, J., AND EOM, J. Direct electrical observation of spin hall effect in bi film. *Applied Physics Letters* 92 (2008), 142101.
- [47] FAN, Y., UPADHYAYA, P., KOU, X., LANG, M., TAKEI, S., WANG, Z., TANG, J., HE, L., CHANG, L.-T., MONTAZERI, M., YU, G., JIANG, W., NIE, T.,

- SCHWARTZ, R. N., TSERKOVNYAK, Y., AND WANG, K. L. Magnetization switching through giant spin-orbit torque in a magnetically doped topological insulator heterostructure. *Nature Materials* 13, 7 (Apr. 2014), 699–704.
- [48] FANG, C., CHEN, Y., KEE, H.-Y., AND FU, L. Topological nodal line semimetals with and without spin-orbital coupling. *Phys. Rev. B* 92 (2015), 081201(R).
- [49] FANG, C., GILBERT, M. J., AND BERNEVIG, B. A. Bulk topological invariants in noninteracting point group symmetric insulators. *Phys. Rev. B* 86, 11 (Sept. 2012), 115112.
- [50] FANG, C., WENG, H., DAI, X., AND FANG, Z. Topological nodal line semimetals*. *Chinese Phys. B* 25, 11 (Nov. 2016), 117106.
- [51] FANG, Q.-L., ZHANG, J.-M., AND XU, K.-W. Magnetic properties and origin of the half-metallicity of Ti_2MnZ ($\text{Z}=\text{Al, Ga, In, Si, Ge, Sn}$) Heusler alloys with the Hg₂CuTi-type structure. *Journal of Magnetism and Magnetic Materials* 349 (2014), 104.
- [52] FELSER, C., FECHER, G. H., AND BALKED, B. Spintronics: A challenge for materials science and solid-state chemistry. *Angewandte Chemie International Edition* 46 (2007), 668.
- [53] FENG, W., GUO, G.-Y., ZHOU, J., YAO, Y., AND NIU, Q. Large magneto-optical Kerr effect in noncollinear antiferromagnets Mn_3X ($\text{X}=\text{Rh, Ir, Pt}$). *Phys. Rev. B* 92, 14 (Oct. 2015), 144426.
- [54] FINA, I., MARTI, X., YI, D., LIU, J., CHU, J. H., RAYAN-SERRAO, C., SURESHA, S., SHICK, A. B., ŽELEZNÝ, J., JUNGWIRTH, T., FONTCUBERTA, J., AND RAMESH, R. Anisotropic magnetoresistance in an antiferromagnetic semiconductor. *Nature Commun.* 5 (Sep 2014), 4671.
- [55] FREIMUTH, F., BLÜGEL, S., AND MOKROUSOV, Y. Spin-orbit torques in Co/Pt (111) and Mn/W (001) magnetic bilayers from first principles. *Phys. Rev. B* 90, 17 (2014), 174423.
- [56] FU, L., AND KANE, C. L. Topological insulators with inversion symmetry. *Phys. Rev. B* 76 (Jul 2007), 045302.

- [57] FUJITA, H. Field-free, spin-current control of magnetization in non-collinear chiral antiferromagnets. *ArXiv e-prints* (Oct 2016).
- [58] FUJIWARA, K., FUKUMA, Y., MATSUNO, J., IDZUCHI, H., NIIMI, Y., OTANI, Y., AND TAKAGI, H. 5d iridium oxide as a material for spin-current detection. *Nat. Comm.* *4* (2013), 2893.
- [59] GHIMIRE, N. J., LUO, Y., NEUPANE, M., WILLIAMS, D. J., BAUER, E. D., AND RONNING, F. Magnetotransport of single crystalline NbAs. *J. Phys. Condens. Matter* *27* (2015), 152201.
- [60] GILBERT, T. Hohenberg-kohn theorem for nonlocal external potentials. *Physical Review B* *12*, 6 (1975), 2111.
- [61] GOLUB, L. E., IVCHENKO, E. L., AND SPIVAK, B. Z. Photocurrent in gyrotropic Weyl semimetals. *Jetp Lett.* *105*, 12 (2017), 782–785.
- [62] GOMONAY, H. V., KUNITSYN, R. V., AND LOKTEV, V. M. Symmetry and the macroscopic dynamics of antiferromagnetic materials in the presence of spin-polarized current. *Phys. Rev. B* *85*, 13 (apr 2012), 134446.
- [63] GOMONAY, H. V., AND LOKTEV, V. M. Spin transfer and current-induced switching in antiferromagnets. *Phys. Rev. B* *81* (Apr 2010), 144427.
- [64] GOMONAY, O., JUNGWIRTH, T., AND SINOVA, J. High antiferromagnetic domain wall velocity induced by néel spin-orbit torques. *Phys. Rev. Lett.* *117* (Jun 2016), 017202.
- [65] GOOTH, J., NIEMANN, A. C., MENG, T., GRUSHIN, A. G., LANDSTEINER, K., GOTSMANN, B., MENGES, F., SCHMIDT, M., SHEKHAR, C., SUESS, V., HUEHNE, R., RELLINGHAUS, B., FELSER, C., YAN, B., AND NIELSCH, K. Experimental signatures of the mixed axial-gravitational anomaly in the Weyl semimetal NbP. *arXiv* (Mar. 2017).
- [66] GOSWAMI, P., PIXLEY, J. H., AND DAS SARMA, S. Axial anomaly and longitudinal magnetoresistance of a generic three-dimensional metal. *Phys. Rev. B* *92*, 7 (Aug. 2015), 075205.
- [67] GRADHAND, M., FEDOROV, D., PIENKA, F., ZAHN, P., MERTIG, I., AND GYÖRFFY, B. L. First-principle calculations of the berry curvature of bloch states

- for charge and spin transport of electrons. *Journal of Physics: Condensed Matter* **24**, 21 (2012), 213202.
- [68] GRINBERG, I., WEST, D. V., TORRES, M., GOU, G., STEIN, D. M., WU, L., CHEN, G., GALLO, E. M., AKBASHEV, A. R., DAVIES, P. K., SPANIER, J. E., AND RAPPE, A. M. Perovskite oxides for visible-light-absorbing ferroelectric and photovoltaic materials. *Nature* **503**, 7477 (Nov. 2013), 509–512.
 - [69] GUO, G. Y., MURAKAMI, S., CHEN, T.-W., AND NAGAOSA, N. Intrinsic spin Hall effect in platinum: first-principles calculations. *Phys. Rev. Lett.* **100** (Mar. 2008), 096401.
 - [70] HANEY, P. M., AND MACDONALD, A. H. Current-Induced Torques Due to Compensated Antiferromagnets. *Phys. Rev. Lett.* **100**, 19 (may 2008), 196801.
 - [71] HANEY, P. M., WALDRON, D., DUINE, R. A., NÚÑEZ, A., GUO, H., AND MACDONALD, A. H. Ab initio giant magnetoresistance and current-induced torques in Cr/Au/Cr multilayers. *Phys. Rev. B* **75** (2007), 174428(1)–174428(7).
 - [72] HASAN, M. Z., AND KANE, C. L. Colloquium: Topological insulators. *Rev. Mod. Phys.* **82**, 4 (Nov. 2010), 3045–3067.
 - [73] HIRAYAMA, M., OKUGAWA, R., MIYAKE, T., AND MURAKAMI, S. Topological Dirac Nodal Lines in fcc Calcium, Strontium, and Ytterbium. *arXiv:1602.06501* (Feb. 2016).
 - [74] HOFFMANN, A. Advances in magnetics: Spin hall effects in metals. *IEEE Transactions on Magnetism* **49** (2013), 5172.
 - [75] HOSUR, P. Circular photogalvanic effect on topological insulator surfaces: Berry-curvature-dependent response. *Phys. Rev. B* **83**, 3 (Jan. 2011), 035309.
 - [76] HOSUR, P., AND QI, X.-L. Tunable circular dichroism due to the chiral anomaly in weyl semimetals. *Phys. Rev. B* **91** (Feb 2015), 081106.
 - [77] HUANG, L., MCCORMICK, T. M., OCHI, M., ZHAO, Z., SUZUKI, M.-T., ARITA, R., WU, Y., MOU, D., CAO, H., YAN, J., TRIVEDI, N., AND KAMINSKI, A. Spectroscopic evidence for a type II Weyl semimetallic state in MoTe₂. *Nat. Mater.* **15**, 11 (July 2016), 1155–1160.

- [78] HUANG, S.-M., XU, S.-Y., BELOPOLSKI, I., LEE, C.-C., CHANG, G., WANG, B., ALIDOUST, N., BIAN, G., NEUPANE, M., ZHANG, C., JIA, S., BANSIL, A., LIN, H., AND HASAN, M. Z. A Weyl Fermion semimetal with surface Fermi arcs in the transition metal monpnictide TaAs class. *Nat. Commun.* 6 (June 2015), 8373.
- [79] HUANG, X., ZHAO, L., LONG, Y., WANG, P., CHEN, D., YANG, Z., LIANG, H., XUE, M., WENG, H., FANG, Z., DAI, X., AND CHEN, G. Observation of the Chiral-Anomaly-Induced Negative Magnetoresistance in 3D Weyl Semimetal TaAs. *Phys. Rev. X* 5, 3 (Aug. 2015), 031023.
- [80] HUH, Y., MOON, E.-G., AND KIM, Y. B. Long-range coulomb interaction in nodal-ring semimetals. *Phys. Rev. B* 93 (Jan 2016), 035138.
- [81] ŽELEZNÝ, J., GAO, H., MANCHON, A., FREIMUTH, F., MOKROUSOV, Y., ZEMEN, J., MAŠEK, J., SINOVA, J., AND JUNGWIRTH, T. Spin-orbit torques in locally and globally noncentrosymmetric crystals: Antiferromagnets and ferromagnets. *Phys. Rev. B* 95 (Jan 2017), 014403.
- [82] ISHIZUKA, H., HAYATA, T., UEDA, M., AND NAGAOSA, N. Emergent electromagnetic induction and adiabatic charge pumping in noncentrosymmetric weyl semimetals. *Phys. Rev. Lett.* 117 (Nov 2016), 216601.
- [83] ISHIZUKA, H., HAYATA, T., UEDA, M., AND NAGAOSA, N. Momentum-space electromagnetic induction in weyl semimetals. *Physical Review B* 95, 24 (2017), 245211.
- [84] JI, Z., LIU, G., ADDISON, Z., LIU, W., YU, P., GAO, H., LIU, Z., RAPPE, A. M., KANE, C. L., MELE, E. J., ET AL. Spatially dispersive circular photogalvanic effect in a weyl semimetal. *arXiv preprint arXiv:1802.04387* (2018).
- [85] JIANG, J., LIU, Z. K., SUN, Y., YANG, H. F., RAJAMATHI, C. R., QI, Y. P., YANG, L. X., CHEN, C., PENG, H., HWANG, C. C., SUN, S. Z., MO, S.-K., VOBORNIK, I., FUJII, J., PARKIN, S., FELSER, C., YAN, B., AND CHEN, Y. L. Signature of type-II Weyl semimetal phase in MoTe₂. *Nat. Commun.* 8 (Jan. 2017), 13973.
- [86] JULLIERE, M. Tunneling between ferromagnetic films. *Physics Letters A* 54, 3 (1975), 225 – 226.

- [87] JUNGWIRTH, T., MARTI, X., WADLEY, P., AND WUNDERLICH, J. Antiferromagnetic spintronics. *Nature Nanotechnology* 11 (Mar 2016), 231–241.
- [88] KÁDÁR, G., AND KRÉN, E. Neutron diffraction study of mn₃ge. *International Journal of Magnetism* 1 (1971), 43.
- [89] KAHK, J. M., POLL, C. G., OROPEZA, F. E., ABLETT, J. M., CÉOLIN, D., RUEFF, J.-P., AGRESTINI, S., UTSUMI, Y., TSUEI, K. D., LIAO, Y. F., BORGATTI, F., PANACCIONE, G., REGOUTZ, A., EGDELL, R. G., MORGAN, B. J., SCANLON, D. O., AND PAYNE, D. J. Understanding the Electronic Structure of IrO₂ Using Hard-X-ray Photoelectron Spectroscopy and Density-Functional Theory. *Phys. Rev. Lett.* 112, 11 (Mar. 2014), 117601.
- [90] KANAZAWA, N., ONOSE, Y., ARIMA, T., OKUYAMA, D., OHYAMA, K., WAKIMOTO, S., KAKURAI, K., ISHIWATA, S., AND TOKURA, Y. Large Topological Hall Effect in a Short-Period Helimagnet MnGe. *Phys. Rev. Lett.* 106, 15 (Apr. 2011), 156603.
- [91] KARGARIAN, M., RANDEIRA, M., AND TRIVEDI, N. Theory of Kerr and Faraday rotations and linear dichroism in Topological Weyl Semimetals. *Sci. Rep.* 5, 1 (Aug. 2015), 12683.
- [92] KHVALKOVSKIY, A. V., APALKOV, D., WATTS, S., CHEPULSKII, R., BEACH, R. S., ONG, A., TANG, X., DRISKILL-SMITH, A., BUTLER, W. H., VISSCHER, P. B., LOTTIS, D., CHEN, E., NIKITIN, V., AND KROUNBI, M. Basic principles of stt-mram cell operation in memory arrays. *Journal of Physics D: Applied Physics* 46, 7 (2013), 074001.
- [93] KIM, B., JIN, H., MOON, S., KIM, J.-Y., PARK, B.-G., LEEM, C., YU, J., NOH, T., KIM, C., OH, S. J., PARK, J. H., DURAIRAJ, V., CAO, G., AND ROTENBERG, E. Novel $J_{eff} = 1/2$ Mott State Induced by Relativistic Spin-Orbit Coupling in Sr₂ IrO₄. *Phys. Rev. Lett.* 101, 7 (Aug. 2008), 076402.
- [94] KIM, B. J., OHSUMI, H., KOMESU, T., SAKAI, S., MORITA, T., TAKAGI, H., AND ARIMA, T. Phase-Sensitive Observation of a Spin-Orbital Mott State in Sr₂IrO₄. *Science* 323, 5919 (Mar. 2009), 1329–1332.
- [95] KIM, D.-J., JEON, C.-Y., CHOI, J.-G., LEE, J. W., SURABHI, S., JEONG, J.-R., LEE, K.-J., AND PARK, B.-G. Observation of transverse spin nernst mag-

- netoresistance induced by thermal spin current in ferromagnet/non-magnet bilayers. *Nature Communications* 8, 1 (2017), 1400.
- [96] KIM, W. J., KIM, S. Y., KIM, C. H., SOHN, C. H., KORNETA, O. B., CHAE, S. C., AND NOH, T. W. Spin-orbit coupling induced band structure change and orbital character of epitaxial IrO₂ films. *Phys. Rev. B* 93, 4 (2016), 045104.
 - [97] KIM, Y., WIEDER, B. J., KANE, C. L., AND RAPPE, A. M. Dirac Line Nodes in Inversion-Symmetric Crystals. *Phys. Rev. Lett.* 115, 3 (2015), 036806.
 - [98] KIMEL, A., KIRILYUK, A., TSVETKOV, A., PISAREV, R., AND RASING, T. Laser-induced ultrafast spin reorientation in the antiferromagnet tmfeo₃. *Nature* 429, 6994 (2004), 850–853.
 - [99] KIMURA, T., OTANI, Y., SATO, T., TAKAHASHI, S., AND MAEKAWA, S. Room-temperature reversible spin hall effect. *Physical Review Letters* 98 (2007), 156601.
 - [100] KLEINER, W. H. Space-time symmetry of transport coefficients. *Physical Review* 142 (1966), 318.
 - [101] KLOTZ, J., WU, S.-C., SHEKHAR, C., SUN, Y., SCHMIDT, M., NICKLAS, M., BAENITZ, M., UHLARZ, M., WOSNITZA, J., FELSER, C., AND YAN, B. Quantum oscillations and the Fermi surface topology of the Weyl semimetal NbP. *Phys. Rev. B* 93, 12 (Mar. 2016), 121105.
 - [102] KOEPERNIK, K., AND ESCHRIG, H. Full-potential nonorthogonal local-orbital minimum-basis band-structure scheme. *Physical Review B* 59, 3 (1999), 1743.
 - [103] KRAUT, W., AND VON BALTZ, R. Anomalous bulk photovoltaic effect in ferroelectrics: a quadratic response theory. *Physical Review B* 19, 3 (1979), 1548.
 - [104] KRÉN, E., AND KÁDÁR, G. Neutron diffraction study of mn₃ga. *Solid State Communications* 8, 20 (1970), 1653–1655.
 - [105] KRESSE, G., AND FURTHMÜLLER, J. Efficient iterative schemes for ab initio total-energy calculations using a plane-wave basis set. *Phys. Rev. B* 54, 16 (1996), 11169.
 - [106] KRIEGNER, D., VÝBORNÝ, K., OLEJNÍK, K., REICHOVÁ, H., NOVÁK, V., MARTI, X., GAZQUEZ, J., SAIDL, V., NĚMEC, P., VOLOBUEV, V. V., SPRINGHOLZ, G., HOLÝ, V., AND JUNGWIRTH, T. Multiple-stable anisotropic

- magnetoresistance memory in antiferromagnetic MnTe. *Nature Commun.* **7** (Jun 2016), 11623.
- [107] KRISTOFFEL, N., AND GULBIS, A. Some optical properties of a vibronic ferroelectric and the anomalous bulk photovoltaic effect. *Zeitschrift für Physik B Condensed Matter* **39**, 2 (1980), 143–149.
 - [108] KÜBLER, J., AND FELSER, C. Non-collinear antiferromagnets and the anomalous Hall effect. *EPL* **108** (Dec. 2014), 67001.
 - [109] KÜBLER, J., AND FELSER, C. Weyl points in the ferromagnetic heusler compound Co_2MnAl . *EPL* **114** (2016), 47005.
 - [110] LEE, J., WANG, Z., XIE, H., MAK, K. F., AND SHAN, J. Valley magnetoelectricity in single-layer MoS_2 . *Nature Materials* **16**, 9 (2017), 887.
 - [111] LEE, W.-L., WATAUCHI, S., MILLER, V. L., CAVA, R. J., AND ONG, N. P. Anomalous hall effect current and nernst effect in the CuCr_2Se_4 - xBi_2Se_3 ferromagnet. *Physical Review Letters* **93** (2004), 226601.
 - [112] LEJAEGHERE, K., BIHLMAYER, G., BJÖRKMAN, T., BLAHA, P., BLÜGEL, S., BLUM, V., CALISTE, D., CASTELLI, I. E., CLARK, S. J., DAL CORSO, A., ET AL. Reproducibility in density functional theory calculations of solids. *Science* **351**, 6280 (2016), aad3000.
 - [113] LI, R., MA, H., CHENG, X., WANG, S., LI, D., ZHANG, Z., LI, Y., AND CHEN, X.-Q. Dirac Node Lines in Pure Alkali Earth Metals. *Phys. Rev. Lett.* **117**, 9 (Aug. 2016), 096401.
 - [114] LIM, S., RAJAMATHI, C. R., SUSS, V., FELSER, C., AND KAPITULNIK, A. Temperature-induced inversion of the spin-photogalvanic effect in WTe_2 and MoTe_2 . *arXiv* (Feb. 2018).
 - [115] LIN, J. J., HUANG, S. M., LIN, Y. H., LEE, T. C., LIU, H., ZHANG, X. X., CHEN, R. S., AND HUANG, Y. S. Low temperature electrical transport properties of RuO_2 and IrO_2 single crystals. *Journal of Physics: Condensed Matter* **16**, 45 (2004), 8035–8041.
 - [116] LITVIN, D. B., AND OPECHOWSKI, W. Spin groups. *Physica* **76** (Sep 1974), 538–554.

- [117] LIU, C.-X., QI, X.-L., DAI, X., FANG, Z., AND ZHANG, S.-C. Quantum Anomalous Hall Effect in Hg_{1-y}MnyTe Quantum Wells. *Phys. Rev. Lett.* **101**, 14 (Oct. 2008).
- [118] LIU, J., AND BALENTS, L. Anomalous Hall effect and topological defects in anti-ferromagnetic Weyl semimetals: Mn₃Sn/Ge. *arXiv:1703.08910* (2017).
- [119] LIU, L., PAI, C.-F., LI, Y., TSENG, H. W., RALPH, D. C., AND BUHRMAN, R. A. Spin-torque switching with the giant spin hall effect of tantalum. *Science* **336**, 6081 (2012), 555–558.
- [120] LIU, Q., GUO, Y., AND FREEMAN, A. J. Tunable rashba effect in two-dimensional laobis2 films: Ultrathin candidates for spin field effect transistors. *Nano letters* **13**, 11 (2013), 5264–5270.
- [121] LIU, Z. K., ZHOU, B., ZHANG, Y., WANG, Z. J., WENG, H. M., PRABHAKARAN, D., MO, S.-K., SHEN, Z. X., FANG, Z., DAI, X., HUSSAIN, Z., AND CHEN, Y. L. Discovery of a Three-Dimensional Topological Dirac Semimetal, Na₃Bi. *Science* **343**, 6173 (Feb. 2014), 864–867.
- [122] LU, L., WANG, Z., YE, D., RAN, L., FU, L., JOANNOPOULOS, J. D., AND SOLJA I, M. Experimental observation of Weyl points. *Science* **349**, 6248 (Aug. 2015), 622–624.
- [123] LUO, Y., GHIMIRE, N. J., WARTENBE, M., CHOI, H., NEUPANE, M., McDONALD, R. D., BAUER, E. D., ZHU, J., THOMPSON, J. D., AND RONNING, F. Electron-hole compensation effect between topologically trivial electrons and nontrivial holes in NbAs. *Phys. Rev. B* **92**, 20 (Nov. 2015), 205134.
- [124] LV, B. Q., FENG, Z. L., XU, Q. N., MA, J. Z., AND KONG, L. Y. Experimental Observation of Three-Component ‘New Fermions’ in Topological Semimetal MoP. *arXiv* (2016).
- [125] LV, B. Q., WENG, H. M., FU, B. B., WANG, X. P., MIAO, H., MA, J., RICHARD, P., HUANG, X. C., ZHAO, L. X., CHEN, G. F., FANG, Z., DAI, X., QIAN, T., AND DING, H. Experimental Discovery of Weyl Semimetal TaAs. *Phys. Rev. X* **5** (2015), 031013.

- [126] MA, Q., XU, S.-Y., CHAN, C.-K., ZHANG, C.-L., CHANG, G., LIN, Y., XIE, W., PALACIOS, T., LIN, H., JIA, S., ET AL. Direct optical detection of weyl fermion chirality in a topological semimetal. *Nature Physics* (2017).
- [127] MACDONALD, A. H., AND TSOI, M. Antiferromagnetic metal spintronics. *Phil. Trans. R. Soc. A* 369, 1948 (2011), 3098–3114.
- [128] MACNEILL, D., STIEHL, G. M., GUIMARAES, M. H. D., BUHRMAN, R. A., PARK, J., AND RALPH, D. C. Control of spin-orbit torques through crystal symmetry in WTe₂/ferromagnet bilayers. *Nature Physics* 13 (Nov 2016), 300–305.
- [129] MAEKAWA, S., VALENZUELA, S. O., SAITOH, E., AND KIMURA, T. *Spin Current*, vol. 17. Oxford University Press, 2012.
- [130] MANCHON, A. Spin diffusion and torques in disordered antiferromagnets. *arXiv:1608.00140* (jul 2016).
- [131] MARZARI, N., MOSTOFI, A. A., YATES, J. R., SOUZA, I., AND VANDERBILT, D. Maximally localized wannier functions: Theory and applications. *Reviews of Modern Physics* 84, 4 (2012), 1419.
- [132] MERODIO, P., KALITSOV, A., BA, H., BALTZ, V., AND CHSHIEV, M. Spin-dependent transport in antiferromagnetic tunnel junctions. *Appl. Phys. Lett.* 105, 12 (2014), 122403.
- [133] MEYER, S., CHEN, Y.-T., WIMMER, S., ALTHAMMER, M., WIMMER, T., SCHLITZ, R., GEPRAGS, S., HUEBL, H., KDDERITZSCH, D., EBERT, H., BAUER, G. E. W., GROSS, R., AND GOENNENWEIN, S. T. B. Observation of the spin nernst effect. *Nature Materials* 16 (2017), 977.
- [134] MIRON, I. M., GARELLO, K., GAUDIN, G., ZERMATTEN, P.-J., COSTACHE, M. V., AUFFRET, S., BANDIERA, S., RODMACQ, B., SCHUHL, A., AND GAMBARDELLA, P. Perpendicular switching of a single ferromagnetic layer induced by in-plane current injection. *Nature* 476, 7359 (2011), 189–193.
- [135] MIYAZAKI, T., AND TEZUKA, N. Giant magnetic tunneling effect in fe/al₂o₃/fe junction. *Journal of Magnetism and Magnetic Materials* 139, 3 (1995), L231 – L234.
- [136] MOLL, P. J. W., POTTER, A. C., NAIR, N. L., RAMSHAW, B. J., MODIC, K. A., RIGGS, S., ZENG, B., GHIMIRE, N. J., BAUER, E. D., KEALHOFER, R.,

- RONNING, F., AND ANALYTIS, J. G. Magnetic torque anomaly in the quantum limit of Weyl semimetals. *Nat. Commun.* 7 (2016), 12492.
- [137] MOODERA, J. S., KINDER, L. R., WONG, T. M., AND MESERVEY, R. Large magnetoresistance at room temperature in ferromagnetic thin film tunnel junctions. *Phys. Rev. Lett.* 74 (Apr 1995), 3273–3276.
- [138] MOORE, J. E., AND ORENSTEIN, J. Confinement-Induced Berry Phase and Helicity-Dependent Photocurrents. *Phys. Rev. Lett.* 105, 2 (July 2010), 026805.
- [139] MORIMOTO, T., AND NAGAOSA, N. Topological nature of nonlinear optical effects in solids. *Science advances* 2, 5 (2016), e1501524.
- [140] MORIMOTO, T., ZHONG, S., ORENSTEIN, J., AND MOORE, J. E. Semiclassical theory of nonlinear magneto-optical responses with applications to topological Dirac/Weyl semimetals. *Phys. Rev. B* 94, 24 (Dec. 2016), 245121.
- [141] MURAKAMI, S., NAGAOSA, N., AND ZHANG, S.-C. Dissipationless quantum spin current at room temperature. *Science* 301 (2003), 1348.
- [142] NAGAOSA, N., SINOVA, J., ONODA, S., MACDONALD, A. H., AND ONG, N. P. Anomalous Hall effect. *Reviews of Modern Physics* 82 (2010), 1539.
- [143] NAKATSUJI, S., KIYOHARA, N., AND HIGO, T. Large anomalous Hall effect in a non-collinear antiferromagnet at room temperature. *Nature* 527, 7577 (Oct. 2015), 212–215.
- [144] NAYAK, A. K., FISCHER, J. E., SUN, Y., YAN, B., KAREL, J., KOMAREK, A. C., SHEKHAR, C., KUMAR, N., SCHNELLE, W., KUBLER, J., FELSER, C., AND PARKIN, S. S. P. Large anomalous Hall effect driven by a nonvanishing Berry curvature in the noncollinear antiferromagnet Mn₃Ge. *Sci. Adv.* 2, 4 (Apr. 2016), e1501870–e1501870.
- [145] NDIAYE, P. B., AKOSA, C. A., AND MANCHON, A. Topological hall and spin hall effects in disordered skyrmionic textures. *Physical Review B* 95, 6 (2017), 064426.
- [146] NEUBAUER, A., PFLEIDERER, C., BINZ, B., ROSCH, A., RITZ, R., NIKLOWITZ, P. G., AND BÖNI, P. Topological Hall Effect in the A Phase of MnSi. *Phys. Rev. Lett.* 102, 18 (May 2009), 186602.

- [147] NEUMANN, J. V., AND WIGNER, E. P. W. Ueber merkwürdige diskrete eigenwerte. *Phys. Z.* 30 (1929), 465.
- [148] NIELSEN, H. B., AND NINOMIYA, M. Absence of neutrinos on a lattice: (I). Proof by homotopy theory. *Nucl. Phys. B* 185, 1 (July 1981), 20–40.
- [149] NIEMANN, A. C., GOOTH, J., WU, S.-C., BÄSSLER, S., SERGELIUS, P., HÜHNE, R., RELLINGHAUS, B., SHEKHAR, C., SUSS, V., SCHMIDT, M., FELSER, C., YAN, B., AND NIELSCH, K. Chiral magnetoresistance in the Weyl semimetal NbP. *Sci. Rep.* 7 (Mar. 2017), srep43394.
- [150] NÚÑEZ, A. S., DUINE, R. A., HANEY, P., AND MACDONALD, A. H. Theory of spin torques and giant magnetoresistance in antiferromagnetic metals. *Phys. Rev. B* 73 (Jun 2006), 214426.
- [151] OBORIL, F., BISHNOI, R., EBRAHIMI, M., AND TAHOORI, M. B. Evaluation of hybrid memory technologies using sot-mram for on-chip cache hierarchy. *IEEE Transactions on Computer-Aided Design of Integrated Circuits and Systems* 34, 3 (March 2015), 367–380.
- [152] OH, Y.-W., CHRIS BAEK, S.-H., KIM, Y. M., LEE, H. Y., LEE, K.-D., YANG, C.-G., PARK, E.-S., LEE, K.-S., KIM, K.-W., GO, G., JEONG, J.-R., MIN, B.-C., LEE, H.-W., LEE, K.-J., AND PARK, B.-G. Field-free switching of perpendicular magnetization through spin-orbit torque in antiferromagnet/ferromagnet/oxide structures. *Nature Nanotech.* 11 (Oct 2016), 878–884.
- [153] OHGUSHI, K., MURAKAMI, S., AND NAGAOSA, N. Spin anisotropy and quantum Hall effect in the kagome lattice: Chiral spin state based on a ferromagnet. *Physical Review B* 62, 10 (2000), R6065–R6068.
- [154] OHYAMA, T., YASUKCHI, K., AND KANEMATSU, K. *Phys. Soc. Japan* 16 (1961), 325.
- [155] OSTERHOUDT, G. B., DIEBEL, L. K., YANG, X., STANCO, J., HUANG, X., SHEN, B., NI, N., MOLL, P., RAN, Y., AND BURCH, K. S. Colossal photovoltaic effect driven by the singular berry curvature in a weyl semimetal. *arXiv preprint arXiv:1712.04951* (2017).

- [156] PARAMESWARAN, S. A., TURNER, A. M., AROVAS, D. P., AND VISHWANATH, A. Topological order and absence of band insulators at integer filling in non-symmorphic crystals. *Nature Physics* 9, 5 (May 2013), 299–303.
- [157] PARK, B. G., WUNDERLICH, J., MARTÍ, X., HOLÝ, V., KUROSAKI, Y., YAMADA, M., YAMAMOTO, H., NISHIDE, A., HAYAKAWA, J., TAKAHASHI, H., SHICK, A. B., AND JUNGWIRTH, T. A spin-valve-like magnetoresistance of an antiferromagnet-based tunnel junction. *Nature Materials* 10 (May 2011), 347–351.
- [158] PARKIN, S., AND YANG, S.-H. Memory on the racetrack. *Nature Nanotech* 10, 3 (Mar. 2015), 195–198.
- [159] PENG, L., YUAN, Y., LI, G., YANG, X., XIAN, J.-J., YI, C.-J., SHI, Y.-G., AND FU, Y.-S. Observation of topological states residing at step edges of WTe₂. *Nat. Commun.* 8, 1 (Sept. 2017), 659.
- [160] PERDEW, J. P., BURKE, K., AND ERNZERHOF, M. Generalized gradient approximation made simple. *Phys. Rev. Lett.* 77 (1996), 3865.
- [161] PERDEW, J. P., AND WANG, Y. Accurate and simple analytic representation of the electron-gas correlation energy. *Physical Review B* 45, 23 (1992), 13244.
- [162] PRAKHYA, K., POPESCU, A., AND HANEY, P. M. Current-induced torques between ferromagnets and compensated antiferromagnets: Symmetry and phase coherence effects. *Phys. Rev. B* 89, 5 (2014), 054421.
- [163] PRENAT, G., JABEUR, K., VANHAUWAERT, P., PENDINA, G. D., OBORIL, F., BISHNOI, R., EBRAHIMI, M., LAMARD, N., BOULLE, O., GARELLO, K., LANGER, J., OCKER, B., CYRILLE, M. C., GAMBARDELLA, P., TAHOORI, M., AND GAUDIN, G. Ultra-fast and high-reliability sot-mram: From cache replacement to normally-off computing. *IEEE Transactions on Multi-Scale Computing Systems* 2, 1 (Jan 2016), 49–60.
- [164] QI, X.-L., AND ZHANG, S.-C. Topological insulators and superconductors. *Rev. Mod. Phys.* 83 (2011), 1057.
- [165] QI, Y., NAUMOV, P. G., ALI, M. N., RAJAMATHI, C. R., SCHNELLE, W., BARKALOV, O., HANFLAND, M., WU, S.-C., SHEKHAR, C., SUN, Y., SUSS, V., SCHMIDT, M., SCHWARZ, U., PIPPEL, E., WERNER, P., HILLEBRAND, R.,

- FORSTER, T., KAMPERT, E., PARKIN, S., CAVA, R. J., FELSER, C., YAN, B., AND MEDVEDEV, S. A. Superconductivity in Weyl semimetal candidate MoTe₂. *Nat. Commun.* 7 (Mar. 2016), 11038.
- [166] QIAN, X., LIU, J., FU, L., AND LI, J. Quantum spin Hall effect in two-dimensional transition metal dichalcogenides. *Science* 346, 6215 (Dec. 2014), 1344–1347.
- [167] QIU, Z., HOU, D., KIKKAWA, T., UCHIDA, K.-I., AND SAITOH, E. All-oxide spin Seebeck effects. *Appl. Phys. Express* 8, 8 (Aug. 2015), 083001.
- [168] RAJAMATHI, C. R., GUPTA, U., KUMAR, N., YANG, H., SUN, Y., SUSS, V., SHEKHAR, C., SCHMIDT, M., BLUMTRITT, H., WERNER, P., YAN, B., PARKIN, S., FELSER, C., AND RAO, C. N. R. Weyl Semimetals as Hydrogen Evolution Catalysts. *Adv. Mater.* 54 (Mar. 2017), 1606202.
- [169] RALPH, D., AND STILES, M. Spin transfer torques. *J. Magn. Magn. Matter.* 320, 7 (2008), 1190 – 1216.
- [170] REICHLOVÁ, H., KRIEGNER, D., HOLÝ, V., OLEJNÍK, K., NOVÁK, V., YAMADA, M., MIURA, K., OGAWA, S., TAKAHASHI, H., JUNGWIRTH, T., AND WUNDERLICH, J. Current-induced torques in structures with ultrathin irnm anti-ferromagnets. *Phys. Rev. B* 92 (Oct 2015), 165424.
- [171] ROSTAMI, H., AND POLINI, M. Nonlinear anomalous photocurrents in Weyl semimetals. *arxiv* (May 2017).
- [172] ROY, P. E., OTXOA, R. M., AND WUNDERLICH, J. Robust picosecond writing of a layered antiferromagnet by staggered spin-orbit fields. *Phys. Rev. B* 94 (Jul 2016), 014439.
- [173] RYDEN, W. D., REED, W. A., AND GREINER, E. S. High-Field Magnetoresistance of Ir O₂. *Physical Review B* (1972).
- [174] SAHIN, C., AND FLATTE, M. E. Tunable giant spin hall conductivities in a strong spin-orbit semimetal: Bi_{1-x}Sb_x. *Physical Review Letters* 114 (2015), 107201.
- [175] SAIDAOU, H., MANCHON, A., AND WAIN TAL, X. Robust spin transfer torque in antiferromagnetic tunnel junctions. *arXiv:1607.01523* (2016).

- [176] SAIDAOUI, H. B. M., MANCHON, A., AND WAIN TAL, X. Spin transfer torque in antiferromagnetic spin valves: From clean to disordered regimes. *Phys. Rev. B* 89 (May 2014), 174430.
- [177] SAITOH, E., UEDA, M., MIYAJIMA, H., AND TATARA, G. Conversion of spin current into charge current at room temperature: Inverse spin-hall effect. *Applied physics letters* 88, 18 (2006), 182509.
- [178] SANCHO, M. P. L., SANCHO, J. M. L., AND RUBIO, J. Quick iterative scheme for the calculation of transfer matrices: application to mo (100). *Phys. F: Met. Phys* 14, 1205 (1984).
- [179] SANCHO, M. P. L., SANCHO, J. M. L., AND RUBIO, J. Highly convergent schemes for the calculation of bulk and surface green functions. *Phys. F: Met. Phys* 15, 851 (1985).
- [180] SCHOOP, L. M., ALI, M. N., STRASSER, C., TOPP, A., VARYKHALOV, A., MARCHENKO, D., DUPPEL, V., PARKIN, S. S. P., LOTSCH, B. V., AND AST, C. R. Dirac cone protected by non-symmorphic symmetry and three-dimensional Dirac line node in ZrSiS. *Nat. Commun.* 7 (Jan. 2016), 11696.
- [181] SCOTT, J. F. *Ferroelectric memories*. Springer-Verlag Berlin Heidelberg, 2000.
- [182] SEEMANN, M., KOEDDERITZSCH, D., WIMMER, S., AND EBERT, H. Symmetry-imposed shape of linear response tensors. *Phys. Rev. B* 92 (2015), 155138.
- [183] SHEKHAR, C., NAYAK, A. K., SUN, Y., SCHMIDT, M., NICKLAS, M., LEERMAKERS, I., ZEITLER, U., SKOURSKI, Y., WOSNITZA, J., LIU, Z., CHEN, Y., SCHNELLE, W., BORRMANN, H., GRIN, Y., FELSER, C., AND YAN, B. Extremely large magnetoresistance and ultrahigh mobility in the topological Weyl semimetal NbP. *Nat. Phys.* 11 (2015), 645.
- [184] SHENG, P., SAKURABA, Y., LAU, Y.-C., TAKAHASHI, S., MITANI, S., AND HAYASHI, M. The spin nernst effect in tungsten. *Science advances* 3, 11 (2017), e1701503.
- [185] SINOVA, J., CULCER, D., NIU, Q., SINITSYN, N. A., JUNGWIRTH, T., AND MACDONALD, A. H. Universal intrinsic spin hall effect. *Physical Review Letters* 92 (2004), 126603.

- [186] SINOVA, J., VALENZUELA, S. O., WUNDERLICH, J., BACK, C., AND JUNGWIRTH, T. Spin hall effects. *Rev. Mod. Phys.* 87 (2015), 1213.
- [187] SIPE, J. E., AND SHKREBTII, A. I. Second-order optical response in semiconductors. *Phys. Rev. B* 61, 8 (Feb. 2000), 5337–5352.
- [188] SKAFTOUROS, S., OZDOGAN, K., SASIOGLU, E., AND GALANAKIS, I. Search for spin gapless semiconductors: The case of inverse heusler compounds. *Appl. Phys. Lett.* 102 (2013), 022402.
- [189] SLATER, J. C., AND KOSTER, G. F. Simplified lcao method for the periodic potential problem. *Physical Review* 94, 6 (1954), 1498.
- [190] SLONCZEWSKI, J. C. Conductance and exchange coupling of two ferromagnets separated by a tunneling barrier. *Phys. Rev. B* 39 (Apr 1989), 6995–7002.
- [191] SODEMANN, I., AND FU, L. Quantum Nonlinear Hall Effect Induced by Berry Curvature Dipole in Time-Reversal Invariant Materials. *Phys. Rev. Lett.* 115, 21 (Nov. 2015), 216806.
- [192] SOLUYANOV, A. A., GRESCH, D., WANG, Z., WU, Q., TROYER, M., DAI, X., AND BERNEVIG, B. A. Type-II Weyl semimetals. *Nature* 527, 7579 (Nov. 2015), 495–498.
- [193] SOLUYANOV, A. A., AND VANDERBILT, D. Computing topological invariants without inversion symmetry. *Phys. Rev. B* 83, 235401 (2011).
- [194] STAMENOVA, M., MOHEBBI, R., SEYED-YAZDI, J., RUNGGER, I., AND SANVITO, S. First-principles spin-transfer torque in CuMnAs|GaP|CuMnAs junctions. *Phys. Rev. B* 95 (Feb 2017), 060403.
- [195] STINSHOFF, ROLF, N. A. K., FECHER, G. H., BALKE, B., OUARDI, S., SKOORSKI, Y., AND NAKAMURA, TETSUYA ANDFELSER, C. Completely compensated ferrimagnetism and sublattice spin crossing in the half-metallic heusler compound mn1.5fev0.5. *Phys. Rew. B* 95 (2017), 060410(R).
- [196] SUN, K., SUN, S., GUO, C., WEI, L., TIAN, H., YANG, H., CHEN, G., AND LI, J. An Anomalous Circular Photogalvanic Effect in the Weyl Semimetal TaAs. *arxiv* (Dec. 2016).

- [197] SUN, K., SUN, S.-S., WEI, L.-L., GUO, C., TIAN, H.-F., CHEN, G.-F., YANG, H.-X., AND LI, J.-Q. Circular photogalvanic effect in the weyl semimetal taas. *Chinese Physics Letters* 34, 11 (2017), 117203.
- [198] SUN, Y., WU, S. C., ALI, M. N., FELSER, C., AND YAN, B. Prediction of Weyl semimetal in orthorhombic MoTe 2. *Phys. Rev. B* 92 (Oct. 2015), 161107(R).
- [199] SUN, Y., ZHANG, Y., FELSER, C., AND YAN, B. Strong intrinsic spin Hall effect in the TaAs family of Weyl semimetals. *Phys. Rev. Lett.* 117 (Apr. 2016), 146403.
- [200] SUN, Y., ZHANG, Y., LIU, C.-X., FELSER, C., AND YAN, B. Dirac nodal lines and induced spin hall effect in metallic rutile oxides. *Physical Review B* 95, 23 (2017), 235104.
- [201] SUNDARAM, G., AND NIU, Q. Wave-packet dynamics in slowly perturbed crystals: Gradient corrections and berry-phase effects. *Physical Review B* 59, 23 (1999), 14915.
- [202] TAGUCHI, K., IMAEDA, T., SATO, M., AND TANAKA, Y. Photovoltaic chiral magnetic effect in weyl semimetals. *Phys. Rev. B* 93 (May 2016), 201202.
- [203] TAGUCHI, Y., OOHARA, Y., YOSHIKAWA, H., NAGAOSA, N., AND TOKURA, Y. Spin chirality, Berry phase, and anomalous Hall effect in a frustrated ferromagnet. *Science* 291, 5513 (2001), 2573–2576.
- [204] TAMAI, A., WU, Q. S., CUCCHI, I., BRUNO, F. Y., RICCO, S., KIM, T. K., HOESCH, M., BARRETEAU, C., GIANNINI, E., BESNARD, C., SOLUYANOV, A. A., AND BAUMBERGER, F. Fermi Arcs and Their Topological Character in the Candidate Type-II Weyl Semimetal MoTe₂ . *Phys. Rev. X* 6, 3 (Aug. 2016), 031021.
- [205] TAN, L. Z., AND RAPPE, A. M. Enhancement of the bulk photovoltaic effect in topological insulators. *Phys. Rev. Lett.* 116, 23 (2016), 237402.
- [206] TANAKA, T., KONTANI, H., NAITO, M., NAITO, T., HIRASHIMA, D. S., YAMADA, K., AND INOUE, J. Intrinsic spin Hall effect and orbital Hall effect in 4d and 5d transition metals. *Phys. Rev. B* 77, 16 (Apr. 2008), 165117.
- [207] TANG, S., ZHANG, C., WONG, D., PEDRAMRAZI, Z., TSAI, H.-Z., JIA, C., MORITZ, B., CLAASSEN, M., RYU, H., KAHN, S., JIANG, J., YAN, H.,

- HASHIMOTO, M., LU, D., MOORE, R. G., HWANG, C.-C., HWANG, C., HUSSAIN, Z., CHEN, Y., UGEDA, M. M., LIU, Z., XIE, X., DEVEREAUX, T. P., CROMMIE, M. F., MO, S.-K., AND SHEN, Z.-X. Quantum spin Hall state in monolayer 1T'-WTe₂. *Nature Physics* 13, 7 (July 2017), 683–687.
- [208] TAUBER, K., FEDOROV, D. V., GRADHAND, M., AND MERTIG, I. Spin hall and spin nernst effect in dilute ternary alloys. *Physical Review B* 87, 16 (2013), 161114.
- [209] TAUBER, K., GRADHAND, M., FEDOROV, D. V., AND MERTIG, I. Extrinsic spin nernst effect from first principles. *Physical review letters* 109, 2 (2012), 026601.
- [210] TILLEY, S. D., CORNUZ, M., SIVULA, K., AND GRÄTZEL, M. Light-Induced Water Splitting with Hematite: Improved Nanostructure and Iridium Oxide Catalysis. *Angew. Chem.* 122, 36 (Aug. 2010), 6549–6552.
- [211] TSHITOYAN, V., CICCARELLI, C., MIHAI, A. P., ALI, M., IRVINE, A. C., MOORE, T. A., JUNGWIRTH, T., AND FERGUSON, A. J. Electrical manipulation of ferromagnetic nife by antiferromagnetic irmn. *Phys. Rev. B* 92 (Dec 2015), 214406.
- [212] ŽELEZNÝ, J. <https://bitbucket.org/zeleznyj/linear-response-symmetry>.
- [213] VON BALTZ, R., AND KRAUT, W. Theory of the bulk photovoltaic effect in pure crystals. *Physical Review B* 23, 10 (1981), 5590.
- [214] WADLEY, P., HOWELLS, B., ŽELEZNÝ, J., ANDREWS, C., HILLS, V., CAMPION, R. P., NOVÁK, V., OLEJNÍK, K., MACCHEROZZI, F., DHESI, S. S., MARTIN, S. Y., WAGNER, T., WUNDERLICH, J., FREIMUTH, F., MOKROUSOV, Y., KUNEŠ, J., CHAUHAN, J. S., GRZYBOWSKI, M. J., RUSHFORTH, A. W., EDMONDS, K. W., GALLAGHER, B. L., AND JUNGWIRTH, T. Electrical switching of an antiferromagnet. *Science* 351, 6273 (2016), 587–590.
- [215] WAN, X. G., TURNER, A. M., VISHWANATH, A., AND SAVRASOV, S. Y. Topological semimetal and Fermi-arc surface states in the electronic structure of pyrochlore iridates. *Phys. Rev. B* 83, 20 (May 2011), 205101.
- [216] WANG, C., SEINIGE, H., CAO, G., ZHOU, J.-S., GOODENOUGH, J. B., AND TSOI, M. Anisotropic magnetoresistance in antiferromagnetic sr₂iro₄. *Phys. Rev. X* 4 (Nov 2014), 041034.

- [217] WANG, Z., GRESCH, D., SOLUYANOV, A. A., XIE, W., KUSHWAHA, S., DAI, X., TROYER, M., CAVA, R. J., AND BERNEVIG, B. A. MoTe₂: A Type-II Weyl Topological Metal. *Phys. Rev. Lett.* *117*, 5 (July 2016), 056805.
- [218] WANG, Z., SUN, Y., CHEN, X.-Q., FRANCHINI, C., XU, G., HONGMING WENG, DAI, X., AND ZHONG FANG. Dirac semimetal and topological phase transitions in A₃Bi (A= Na, K, Rb). *Phys. Rev. B* *85* (May 2012), 195320.
- [219] WANG, Z., ZHENG, Y., SHEN, Z., ZHOU, Y., YANG, X., LI, Y., FENG, C., AND XU, Z.-A. Helicity protected ultrahigh mobility Weyl fermions in NbP. *arXiv:1506.00924* (June 2015).
- [220] WANG, Z. W., VERGNIORY, M. G., KUSHWAHA, S., HIRSCHBERGER, M., AND CHULKOV, E. V. Time-reversal-breaking weyl fermions in magnetic heusler alloys. *Physical Review Letters* *117* (2016), 236401.
- [221] WANNIER, G. H. The structure of electronic excitation levels in insulating crystals. *Physical Review* *52*, 3 (1937), 191.
- [222] WENG, H., FANG, C., FANG, Z., BERNEVIG, B. A., AND DAI, X. Weyl Semimetal Phase in Noncentrosymmetric Transition-Metal Monophosphides. *Phys. Rev. X* *5*, 1 (Mar. 2015), 011029.
- [223] WENG, H., FANG, C., FANG, Z., AND DAI, X. Coexistence of Weyl fermion and massless triply degenerate nodal points. *Phys. Rev. B* *94*, 16 (Oct. 2016), 165201.
- [224] WENG, H., FANG, C., FANG, Z., AND DAI, X. Topological semimetals with triply degenerate nodal points in θ -phase tantalum nitride. *Phys. Rev. B* *93*, 24 (June 2016), 241202.
- [225] WENG, H., LIANG, Y., XU, Q., YU, R., FANG, Z., DAI, X., AND KAWAZOE, Y. Topological node-line semimetal in three-dimensional graphene networks. *Phys. Rev. B* *92*, 4 (July 2015), 045108.
- [226] WIEDER, B. J., KIM, Y., RAPPE, A. M., AND KANE, C. L. Double Dirac Semimetals in Three Dimensions. *Phys. Rev. Lett.* *116*, 18 (May 2016), 186402.
- [227] WIMMER, S., KÖDDERITZSCH, D., CHADOVA, K., AND EBERT, H. First-principles linear response description of the spin nernst effect. *Physical Review B* *88*, 20 (2013), 201108.

- [228] WIMMER, S., SEEMANN, M., CHADOVA, K., KÖDDERITZSCH, D., AND EBERT, H. Spin-orbit-induced longitudinal spin-polarized currents in nonmagnetic solids. *Phys. Rev. B* *92* (Jul 2015), 041101.
- [229] WINKLER, G. W., WU, Q., TROYER, M., KROGSTROP, P., AND SOLUYANOV, A. A. Topological Phases in $\text{InAs}_{1-x}\text{Sb}_x$: From Novel Topological Semimetal to Majorana Wire . *Phys. Rev. Lett.* *117*, 7 (Aug. 2016), 076403.
- [230] WU, L., PATANKAR, S., MORIMOTO, T., NAIR, N. L., THEWALT, E., LITTLE, A., ANALYTIS, J. G., MOORE, J. E., AND ORENSTEIN, J. Giant anisotropic nonlinear optical response in transition metal monpnictide Weyl semimetals. *Nature Physics* *13*, 4 (Apr. 2017), 350–355.
- [231] WU, S., FATEMI, V., GIBSON, Q. D., WATANABE, K., TANIGUCHI, T., CAVA, R. J., AND JARILLO-HERRERO, P. Observation of the quantum spin Hall effect up to 100 kelvin in a monolayer crystal. *Science* *359*, 6371 (Jan. 2018), 76–79.
- [232] WU, S.-C., SUN, Y., CLAUDIA, F., AND YAN, B. Hidden type-II Weyl points in the Weyl semimetal NbP. *arXiv* (2017).
- [233] WU, Y., MOU, D., JO, N. H., SUN, K., HUANG, L., BUD’KO, S. L., CANFIELD, P. C., AND KAMINSKI, A. Observation of Fermi arcs in the type-II Weyl semimetal candidate WTe₂. *Phys. Rev. B* *94*, 12 (Sept. 2016), 121113.
- [234] XIAO, D., CHANG, M.-C., AND NIU, Q. Berry phase effects on electronic properties. *Rev. Mod. Phys.* *82*, 3 (July 2010), 1959–2007.
- [235] XIAO, D., YAO, Y., FANG, Z., AND NIU, Q. Berry-phase effect in anomalous thermoelectric transport. *Physical Review Letters* *97* (2006), 026603.
- [236] XIE, L. S., SCHOOP, L. M., SEIBEL, E. M., GIBSON, Q. D., XIE, W., AND CAVA, R. J. A new form of Ca_3P_2 with a ring of Dirac nodes. *APL Mater.* *3* (2015), 083602.
- [237] XU, G., WENG, H., WANG, Z., DAI, X., AND FANG, Z. Chern Semimetal and the Quantized Anomalous Hall Effect in HgCr_2Se_4 . *Phys. Rev. Lett.* *107*, 18 (Oct. 2011), 186806.
- [238] XU, S., LIU, C., KUSHWAHA, S. K., SANKAR, R., KRIZAN, J. W., BELOPOLSKI, I., NEUPANE, M., BIAN, G., ALIDOUST, N., CHANG, T. R., JENG, H. T.,

- HUANG, C. Y., TSAI, W. F., LIN, H., SHIBAYEV, P. P., CHOU, F. C., CAVA, R. J., AND HASAN, M. Z. Observation of Fermi arc surface states in a topological metal. *Science* *347*, 6219 (Jan. 2015), 294–298.
- [239] XU, S.-Y., BELOPOLSKI, I., ALIDoust, N., NEUPANE, M., BIAN, G., ZHANG, C., SANKAR, R., CHANG, G., ZHUJUN, Y., LEE, C.-C., SHIN-MING, H., ZHENG, H., MA, J., SANCHEZ, D. S., WANG, B., BANSIL, A., CHOU, F., SHIBAYEV, P. P., LIN, H., JIA, S., AND HASAN, M. Z. Discovery of a Weyl fermion semimetal and topological Fermi arcs. *Science* *349* (2015), 613.
- [240] XU, Y., WANG, S., AND XIA, K. Spin-Transfer Torques in Antiferromagnetic Metals from First Principles. *Phys. Rev. Lett.* *100*, 22 (jun 2008), 226602.
- [241] YAMAOKA, T. Antiferromagnetism in -phase mn-ir alloys. *Journal of the Physical Society of Japan* *36*, 2 (1974), 445–450.
- [242] YAN, B., AND FELSER, C. Topological Materials: Weyl Semimetals. *arXiv:1611.04182* (Nov. 2016).
- [243] YANG, H., SUN, Y., ZHANG, Y., SHI, W.-J., PARKIN, S. S. P., AND YAN, B. Topological Weyl semimetals in the chiral antiferromagnetic materials Mn₃Ge and Mn₃Sn. *N. J. Phys.* *19*, 1 (2017), 015008.
- [244] YANG, J., COLEN, J., LIU, J., NGUYEN, M. C., CHERN, G.-W., AND LOUCA, D. Elastic and electronic tuning of magnetoresistance in mote₂. *Science advances* *3*, 12 (2017), eaao4949.
- [245] YANG, K.-Y., LU, Y.-M., AND RAN, Y. Quantum Hall effects in a Weyl semimetal: Possible application in pyrochlore iridates. *Phys. Rev. B* *84*, 7 (Aug. 2011), 075129.
- [246] YANG, L. X., LIU, Z. K., SUN, Y., PENG, H., YANG, H. F., ZHANG, T., ZHOU, B., ZHANG, Y., GUO, Y. F., RAHN, M., PRABHAKARAN, D., HUSSAIN, Z., MO, S. K., FELSER, C., YAN, B., AND CHEN, Y. L. Weyl Semimetal Phase in non-Centrosymmetric Compound TaAs. *Nat. Phys.* *11* (2015), 728–732.
- [247] YANG, S.-H., RYU, K.-S., AND PARKIN, S. Domain-wall velocities of up to 750?m?s⁻¹ driven by exchange-coupling torque in synthetic antiferromagnets. *Nature Nanotech* *10*, 3 (Feb. 2015), 221–226.

- [248] YANG, S. Y., SEIDEL, J., BYRNES, S. J., SHAFER, P., YANG, C. H., ROSSELL, M. D., YU, P., CHU, Y. H., SCOTT, J. F., AGER III, J. W., MARTIN, L. W., AND RAMESH, R. Above-bandgap voltages from ferroelectric photovoltaic devices. *Nature Nanotech* 5, 2 (Feb. 2010), 143–147.
- [249] YANG, X., BURCH, K., AND RAN, Y. Divergent bulk photovoltaic effect in Weyl semimetals. *arXiv* (Dec. 2017), arXiv:1712.09363.
- [250] YIN, G., LIU, Y., BARLAS, Y., ZANG, J., AND LAKE, R. K. Topological spin Hall effect resulting from magnetic skyrmions. *Phys. Rev. B* 92, 2 (July 2015), 024411.
- [251] YOUNG, S. M., AND KANE, C. L. Dirac semimetals in two dimensions. *Phys. Rev. Lett.* 115 (2015), 126803.
- [252] YOUNG, S. M., AND RAPPE, A. M. First principles calculation of the shift current photovoltaic effect in ferroelectrics. *Physical review letters* 109, 11 (2012), 116601.
- [253] YOUNG, S. M., ZAHEER, S., TEO, J. C. Y., KANE, C. L., MELE, E. J., AND RAPPE, A. M. Dirac Semimetal in Three Dimensions. *Phys. Rev. Lett.* 108, 14 (Apr. 2012), 140405.
- [254] YU, R., QI, X. L., BERNEVIG, A., FANG, Z., AND DAI, X. Equivalent expression of z^2 topological invariant for band insulators using the non-abelian berry connection. *Phys. Rev. B* 84, 075119 (2011).
- [255] YU, R., WENG, H., FANG, Z., DAI, X., AND HU, X. Topological Node-Line Semimetal and Dirac Semimetal State in Antiperovskite Cu_3PdN . *Phys. Rev. Lett.* 115, 3 (July 2015), 036807.
- [256] YU, R., ZHANG, W., ZHANG, H. J., ZHANG, S. C., DAI, X., AND FANG, Z. Quantized Anomalous Hall Effect in Magnetic Topological Insulators. *Science* 329, 5987 (July 2010), 61–64.
- [257] ŽELEZNÝ, J., GAO, H., MANCHON, A., FREIMUTH, F., MOKROUSOV, Y., ZEMEN, J., MAŠEK, J., SINOVA, J., AND JUNGWIRTH, T. Spin-orbit torques in locally and globally noncentrosymmetric crystals: Antiferromagnets and ferromagnets. *Physical Review B* 95, 1 (2017), 014403.
- [258] ŽELEZNÝ, J., GAO, H., VÝBORNÝ, K., ZEMEN, J., MAŠEK, J., MANCHON, A., WUNDERLICH, J., SINOVA, J., AND JUNGWIRTH, T. Relativistic Néel-order fields

- induced by electrical current in antiferromagnets. *Phys. Rev. Lett.* **113**, 15 (2014), 157201.
- [259] ZENER, C. Interaction between the d -shells in the transition metals. ii. ferromagnetic compounds of manganese with perovskite structure. *Phys. Rev.* **82** (May 1951), 403–405.
- [260] ZENG, M., FANG, C., CHANG, G., CHEN, Y.-A., HSIEH, T., BANSIL, A., LIN, H., AND FU, L. Topological semimetals and topological insulators in rare earth monpnictides. *arXiv* (Apr. 2015).
- [261] ZENKEVICH, A., MATVEYEV, Y., MAKSIMOVA, K., GAYNUTDINOV, R., TOLSTIKHINA, A., AND FRIDKIN, V. Giant bulk photovoltaic effect in thin ferroelectric batio 3 films. *Physical Review B* **90**, 16 (2014), 161409.
- [262] ZHANG, C.-L., XU, S.-Y., BELOPOLSKI, I., YUAN, Z., LIN, Z., TONG, B., BIAN, G., ALIDOUST, N., LEE, C.-C., HUANG, S.-M., CHANG, T.-R., CHANG, G., HSU, C.-H., JENG, H.-T., NEUPANE, M., SANCHEZ, D. S., ZHENG, H., WANG, J., LIN, H., ZHANG, C., LU, H.-Z., SHEN, S.-Q., NEUPERT, T., ZAHID HASAN, M., AND JIA, S. Signatures of the Adler–Bell–Jackiw chiral anomaly in a Weyl fermion semimetal. *Nat. Commun.* **7** (Feb. 2016), 10735.
- [263] ZHANG, D., YAN, B., WU, S.-C., KÜBLER, J., KREINER, G., PARKIN, S. S., AND FELSER, C. First-principles study of the structural stability of cubic, tetragonal and hexagonal phases in mn_3z ($\text{z} = \text{ga, sn and ge}$) heusler compounds. *Journal of Physics: Condensed Matter* **25**, 20 (2013), 206006.
- [264] ZHANG, W., HAN, W., YANG, S.-H., SUN, Y., ZHANG, Y., YAN, B., AND PARKIN, S. S. P. Giant facet-dependent spin-orbit torque and spin hall conductivity in the triangular antiferromagnet irmn_3 . *Science Advances* **2**, 9 (2016).
- [265] ZHANG, Y., BRINK, J. V. D., FELSER, C., AND YAN, B. Electrically tuneable nonlinear anomalous hall effect in two-dimensional transition-metal dichalcogenides wte_2 and mote_2 . *arXiv preprint arXiv:1804.11069* (2018).
- [266] ZHANG, Y., SUN, Y., AND YAN, B. Berry curvature dipole in Weyl semimetal materials: An ab initio study. *Phys. Rev. B* **97**, 4 (Jan. 2018), 041101 (R).

- [267] ZHANG, Y., SUN, Y., YANG, H., ŽELEZNÝ, J., PARKIN, S. P. P., FELSER, C., AND YAN, B. Strong anisotropic anomalous Hall effect and spin Hall effect in the chiral antiferromagnetic compounds Mn_3X ($X = \text{Ge}, \text{Sn}, \text{Ga}, \text{Ir}, \text{Rh}, \text{and Pt}$). *Phys. Rev. B* 95 (Feb 2017), 075128.
- [268] ZHANG, Y., ŽELEZNÝ, J., SUN, Y., VAN DEN BRINK, J., AND YAN, B. Spin Hall effect emerging from a chiral magnetic lattice without spin-orbit coupling.
- [269] ZHU, Z., WINKLER, G. W., WU, Q., LI, J., AND SOLUYANOV, A. A. Triple Point Topological Metals. *Phys. Rev. X* 6, 3 (July 2016), 031003.

Acknowledgements

At the end of this thesis, I would like to thank all the people who have accompanied me in these three years

Firstly, I would like to thank my supervisor Prof. Dr. Jeroen van den Brink and Prof. Dr. Claudia Felser for granting the Ph.D. position, giving me the great freedom to work on projects I am really interested in, and supporting me to attend several important conference and internship. I'm also indebted to Dr. Binghai Yan for his guidance on my Ph.D. topics, and Prof. Dr. Carsten Timm for his priceless suggestions as my mentor in SFB project, this work is only possible with their great help.

Special thanks also to Prof. Naoto Nagaosa and Dr. Hiroaki Ishizuka for hosting my internship in Riken, working with them is truly a delightful experience for me. I am also grateful to all my colleagues in MPI CPfS and IFW Dresden, especially Dr. Jakub Zelezny and Klaus Koepf for the continuous and fruitful discussions. In particular, I would like to thank all the office mates and friends in MPI CPfS, Hao Yang, Dr. Yan Sun, Dr. Wujun Shi, Dr. Guowei Li and Dr. Qiunan Xu, for the countless discussions and company in spare time.

At last, I would like to express my deep gratitude to my family, especially my sister, parents, and grandparents who have always believed in me and encourage me, sincere gratitude to my wife, for her continuous support and patience.

Eidesstattliche Erklärung

Hiermit versichere ich, dass ich die vorliegende Arbeit ohne unzulässige Hilfe Dritter und ohne Benutzung anderer als der angegebenen Hilfsmittel angefertigt habe; die aus fremden Quellen direkt oder indirekt übernommenen Gedanken sind als solche kenntlich gemacht. Die Arbeit wurde bisher weder im Inland noch im Ausland in gleicher oder ähnlicher Form einer anderen Prüfungsbehörde vorgelegt.

Die vorliegende Arbeit wurde von 02.09.2015 bis 10.12.2018 am Max-Planck-Institutes für Chemische Physik fester Stoffe (MPI CPfS), Festkörperchemie (SSC), und Leibniz-Institut für Festkörper- und Werkstoffforschung Dresden (IFW Dresden), Institut für theoretische Festkörperphysik (ITF), unter der Betreuung von Prof. Dr. Jeroen van den Brink und Dr. Binghai Yan angefertigt.

Ich versichere, dass ich bisher keine erfolglosen Promotionsverfahren unter- nommen habe. Ich erkenne die Promotionsordnung der Fakultät Mathematik und Naturwissenschaften der Technischen Universität Dresden an.

Yang Zhang

Dresden, den 10. Dec 2018